Probabilistic Aerothermal Design of Compressor Airfoils

by

Victor E. Garzon

B.S., University of Kentucky (1994)
M.S., University of Kentucky (1998)

Submitted to the Department of Aeronautics and Astronautics
in partial fulfillment of the requirements for the degree of

Doctor of Philosophy

at the

MASSACHUSETTS INSTITUTE OF TECHNOLOGY

February 2003

Author_____
Department of Aeronautics and Astronautics
11 December 2002

Certified by_____
David L. Darmofal
Associate Professor of Aeronautics and Astronautics
Thesis Supervisor

Certified by_____
Mark Drela
Professor of Aeronautics and Astronautics

Certified by_____
Edward M. Greitzer
H. N. Professor of Aeronautics and Astronautics

Certified by_____
Ian A. Waitz
Professor of Aeronautics and Astronautics

Accepted by_____
Edward M. Greitzer
H. N. Slater Professor of Aeronautics and Astronautics
Chair, Committee on Graduate Students

Probabilistic Aerothermal Design of Compressor Airfoils

by

Victor E. Garzon

Submitted to the Department of Aeronautics and Astronautics
on 11 December 2002, in partial fulfillment of the
requirements for the degree of
Doctor of Philosophy

Abstract

Despite the generally accepted notion that geometric variability is undesirable in turbomachinery airfoils, little is known in detail about its impact on aerothermal compressor performance. In this work, statistical and probabilistic techniques were used to assess the impact of geometric and operating condition uncertainty on axial compressor performance. High-fidelity models of geometric variability were constructed from surface measurements of existing hardware using principal component analysis (PCA). A quasi-two-dimensional cascade analysis code, at the core of a parallel probabilistic analysis framework, was used to assess the impact of uncertainty on aerodynamic performance of compressor rotor airfoils. Three rotor blades with inlet relative Mach numbers of 0.82, 0.90 and 1.25 were considered. Discrepancies between nominal and mean loss (mean-shift) of up to 20% were observed. Loss and turning variability were found to grow linearly with geometric noise amplitude.

A probabilistic, gradient-based approach to compressor blade optimization was presented. Probabilistic objectives, constraints and gradients are approximated using low-resolution Monte Carlo sampling. Test airfoils were optimized both deterministically and probabilistically and then analyzed probabilistically to account for geometric variability. Probabilistically redesigned airfoils exhibited reductions in mean loss of up to 25% and in loss variability of as much as 65% from corresponding values for deterministically redesigned airfoils. A probabilistic mean-line multi-stage axial compressor model was used to estimate the impact of geometric variability on overall compressor performance. Probabilistic loss and turning models were exercised on a six-stage compressor model. At realistic levels of geometric variability, the mean polytropic efficiency was found to be upwards of 1% lower than nominal. Compressor simulations using airfoils redesigned probabilistically for minimum loss variability exhibited reductions of 30 to 40% in polytropic efficiency variability and mean shift.

Thesis Supervisor: David L. Darmofal
Title: Associate Professor of Aeronautics and Astronautics

Acknowledgments

I am indebted to Prof. David Darmofal for suggesting the topic of this thesis, for his excellent academic and technical advise and for his constant encouragement. Thanks to Prof. Edward Greitzer and Prof. Ian Waitz for their research guidance and many contributions to this thesis. Thanks to Prof. Mark Drela for developing MISES and ancillary codes, and for answering countless questions about their usage. Prof. Daniel Frey suggested principal component analysis to characterize geometric variability of compressor airfoils. Thanks also to Dr. Ali Merchant for allowing me use of his codes and for answering various questions about compressor design. Special thanks to Mr. Jeff Lancaster for helping ground this thesis in reality. Mr. Robert Haimes' guidance with system administration matters is also thankfully acknowledged.

The work reported in this thesis was made possible by the financial support of NASA Glenn Research Center through grant No. NAG3-2320.

Contents

1 Introduction **9**
- 1.1 Motivation . . . 9
- 1.2 Background . . . 10
- 1.3 Thesis Objectives . . . 12
- 1.4 Contributions . . . 13
- 1.5 Outline . . . 14

2 Characterization of Geometric Variability **15**
- 2.1 Principal Component Analysis of Airfoil Measurements . . . 15
  - 2.1.1 Background . . . 16
  - 2.1.2 Application . . . 17
- 2.2 Statistical Models of Geometric Variability . . . 22
- 2.3 PCA Results Vs. Number of Samples . . . 23
- 2.4 Other Methods of Describing Geometric Noise . . . 25
- 2.5 Summary . . . 28

3 Impact of Geometric Variability On Compressor Blade Aerodynamics **29**
- 3.1 Aerodynamic Performance Assessment . . . 29
  - 3.1.1 Background . . . 29
  - 3.1.2 Blade row aerodynamic analysis: MISES . . . 30
- 3.2 Probabilistic Analysis . . . 31
  - 3.2.1 Monte Carlo Simulation . . . 32
- 3.3 Applications . . . 33
  - 3.3.1 Integrally-bladed rotor, mid-span section . . . 33
  - 3.3.2 DFVLR transonic cascade . . . 44
  - 3.3.3 NASA rotor 37, mid-span section . . . 49
- 3.4 Summary . . . 53

4 Probabilistic Optimization of Compressor Blade Sections **56**
- 4.1 Gradient-Based Probabilistic Optimization . . . 56
- 4.2 Applications . . . 60
  - 4.2.1 Objectives and Constraints . . . 60
  - 4.2.2 Geometric Design Modes . . . 60
  - 4.2.3 IBR Rotor Mid-Span . . . 61
  - 4.2.4 DFVLR Cascade Airfoil . . . 69
  - 4.2.5 Rotor 37 Mid-Span . . . 76
- 4.3 Summary . . . 83

5 Effect of Geometric Variability on Compressor Performance **85**
5.1 Mean-Line Compressor Model . . . 85
5.2 Loss Coefficient and Turning Angle Models . . . 87
5.3 Probabilistic Mean-Line Calculations . . . 90
5.3.1 Six-stage compressor model: baseline airfoil . . . 90
5.3.2 Six-stage compressor model: redesigned airfoils . . . 94
5.4 Impact of Geometric Noise on Compressor Performance . . . 94
5.5 Multiple-Blade Rows . . . 98
5.6 Summary . . . 100

6 Summary and Recommendations **102**

A Principal Component Analysis **106**
A.1 Background . . . 106
A.2 Basic Theory . . . 106
A.3 Three-Dimensional Analysis of IBR Blade Measurements . . . 109

B Point- Vs. Flank-Milled Compressor Blade Rows **113**

C Robustness Via Constrained Probabilistic Optimization **116**

D Mean-Line Compressor Model **119**
D.1 Nomenclature . . . 119
D.2 Baseline Model . . . 119
D.3 Stage formulae . . . 121
D.4 Rotor System Jacobian . . . 123

Bibliography **124**

List of Figures

1-1 Example of geometric variability in manufactured compressor airfoils 9

2-1 Schematic blunt trailing edge modification 17
2-2 IBR mid-span section: PCA modes 19
2-3 Exponential decay of the eigenvalues of $\mathbf{S}$ 20
2-4 IBR mid-span section: Scaled mode 1 (positive) 20
2-5 IBR mid-span section: Scaled mode 3 (positive) 21
2-6 IBR mid-span section: Scaled mode 6 (positive) 21
2-7 Eigenvalues of covariance matrix versus number of samples 24
2-8 Thickness, twist and leading-edge bluntness 26
2-9 Aerodynamic performance trends and bluntness parameter density 27

3-1 IBR through-flow analysis 34
3-2 IBR, $M_1 = 0.90$, axial velocity-density ratio (AVDR): 1.27 35
3-3 IBR: Impact of geometric variability 36
3-4 IBR: Mean and standard deviation vs. noise amplitude 37
3-5 IBR: Impact of geometric variability ($a = 2$) 39
3-6 IBR: Impact of geometric variability ($a = 5$) 39
3-7 IBR: Impact of geometric variability on distributions of loss and turning, $a = 1, 2, \ldots, 8$ 40
3-8 Sample mean, standard deviation and CDF of $1 - X - 0.01X^2$ 41
3-9 IBR: Effect of geometric variability on displacement thickness 41
3-10 IBR: Effect of geometric variability on shape parameter $H = \delta^*/\theta$. 42
3-11 IBR: Effect of geometric variability on boundary layer dissipation coefficient 43
3-12 IBR: Effect of geometric variability on entropy generation 43
3-13 IBR mid section: Statistics versus number of PCA modes, $a = 5$ 45
3-14 DFVLR cascade, $M_1 = 0.82$, AVDR=1 46
3-15 IBR exit Mach number variability 47
3-16 Aerodynamic performance trends with increased leading-edge bluntness . . 48
3-17 DFVLR: Histograms of loss coefficient and turning angle 49
3-18 DFVLR: Effect of geometric variability on airfoil boundary layers 50
3-19 NASA rotor 37 through-flow results 51
3-20 NASA rotor 37, $M_1 = 1.25$, AVDR=1.452 52
3-21 NASA rotor 37 mid section: histograms 53
3-22 R37: Effect of geometric variability on airfoil boundary layers 54

4-1 Parallel probabilistic optimization framework 58

4-2 Airfoil arc length coordinate conventions and modified Chebyshev polynomials $T'_n(x)$, $n = 1, \ldots, 5$ 61
4-3 IBR: Deterministic vs. probabilistic optimization ($a = 1$, $N = 2000$) 64
4-4 IBR: Loss coefficient statistics for redesigned airfoils ($a = 5$, $N = 2000$) . . . 65
4-5 IBR mid-span: Redesigned nominal airfoil shape ($a = 5$) 66
4-6 IBR mid-span: Baseline and mean pressure coefficient 68
4-7 IBR mid-span: Momentum thickness θ/c ($a = 5$) 69
4-8 IBR mid-span: Shape parameter $H = \delta^*/\theta$ ($a = 5$) 70
4-9 IBR mid-span ($a = 5$): $\int_0^x \rho U_e^3 C'_d dx'$ 71
4-10 DFVLR loss coefficient for redesigned airfoils 73
4-11 DFVLR: Scatter of Loss coefficient vs. turning angle 73
4-12 DFVLR cascade: Redesigned nominal airfoil shape 74
4-13 Redesigned DFVLR airfoil: Pressure coefficient 75
4-14 redesigned DFVLR airfoil: Momentum thickness 76
4-15 redesigned DFVLR airfoil: Shape parameter $H = \delta^*/\theta$ 77
4-16 redesigned DFVLR airfoil: $\int_0^x \rho U_e^3 C d' dx'$ 77
4-17 Rotor 37 loss coefficient for redesigned airfoils 79
4-18 Rotor 37: Scatter of Loss coefficient vs. turning angle 79
4-19 Rotor 37: Redesigned nominal airfoil shape 80
4-20 Rotor 37: Pressure Coefficient 81
4-21 Rotor 37: Suction side boundary layer 82

5-1 IBR: Loss coefficient and turning angle vs. incidence, $a = 2$ 89
5-2 IBR mid-span section: Loss coefficient vs. incidence, $a = 5$. (Linear extrapolation for $\alpha > 0.75$.) 91
5-3 IBR mid-span section: Turning angle vs. incidence, $a = 5$. (Linear extrapolation for $\alpha > 0.75$.) 92
5-4 Monte Carlo results of Mean-line compressor model: IBR airfoils ($a = 1$) . . 94
5-5 Probabilistic mean-line results with redesigned airfoils ($a = 1$) 95
5-6 Rotor and stator incidence variability 97
5-7 Stage exit Mach number variability 99

A-1 Transformation T 110
A-2 Three-dimensional geometric modes 111
A-3 Three-dimensional geometric modes (Cont'd) 112

B-1 Measured deviations for sample point and flank-milled IBR 114

C-1 IBR: Mean loss coefficient vs. standard deviation ($a = 5$) 117
C-2 IBR ($a = 5$): Geometric features of "trade-off" redesigns 118

D-1 Compressor model stages 121

List of Tables

2.1 IBR mid-span section: Geometric features of PCA modes. 22
2.2 Eigenvalues covariance matrix versus number of samples 25

3.1 Percent difference in statistics from reduced-order model (with K modes) and full model ($K = mp$) simulations, $a = 5$ 45
3.2 DFVLR random input statistics 47
3.3 NASA Rotor 37 random input statistics 51

4.1 Number of trials, iterations and function evaluations 62
4.2 Summary of performance statistics for redesigned IBR airfoils, $a = 1, 2, 5$ . . 63
4.3 DFVLR: Redesigned airfoil statistics 72
4.4 Rotor 37 redesigned airfoil statistics (MCS $N = 2000$) 78
4.5 Viscous vs. shock loss for R37 redesigned blade 81

5.1 Six-stage compressor, IBR airfoil-based loss and turning models 96
5.2 Six-stage compressor, IBR airfoil-based loss and turning models, 80 blade passages per row 98
5.3 Six-stage compressor, mean loss and mean turning (no variability) 100

B.1 Spanwise maximum deviation intervals (per unit chord) for point- and flank-milled IBR measurements. 113

C.1 IBR $a = 5$: Mean vs. variability trade-off problem constraints 117

D.1 Baseline compressor model parameters 120
D.2 Baseline compressor model stage settings 121
D.3 Baseline six-stage compressor model (1) 122
D.4 Baseline six-stage compressor model (2) 122

Chapter 1

Introduction

1.1 Motivation

Despite the generally accepted notion that geometric variability is undesirable in turbomachinery airfoils, little detailed information is known about the detrimental effects that geometric variability has on the aerodynamic performance of compressor airfoils. Furthermore, open literature regarding origins and characteristics of compressor airfoil shape variability due to manufacturing or wear is scars at best.

Finished airfoils inevitably exhibit deviations from their intended shape and size [9]. Geometric uncertainty may be introduced, for instance, by noisy manufacturing processes or hand-finishing operations. Figure 1-1 illustrates the discrepancies between actual manufactured compressor airfoil sections (dashed lines) and their intended design (solid line).

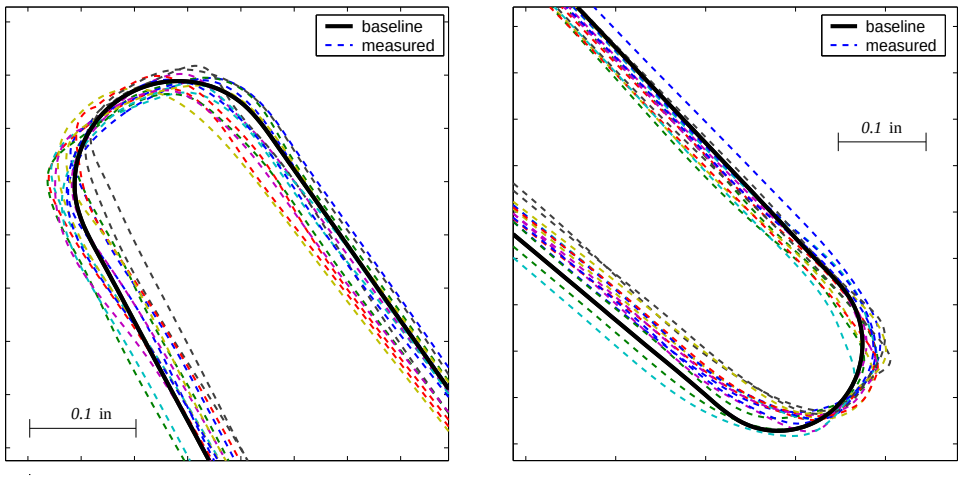

Figure 1-1: Example of geometric variability in manufactured compressor airfoils. Measurements are represented by dashed-lines and the nominal shape by a solid line

As pointed out by Roberts [105], geometric variability in the form of leading-edge erosion in core compressor airfoils may account for an increase of 3% or more on thrust-specific fuel consumption. To put this into perspective, as little as a one percent change in fuel burn can mean the difference between profitability or loss to a fleet operator [35].

Restricting manufacturing tolerances to reduce the amount of geometric uncertainty may be exceedingly costly or otherwise impractical to achieve. Furthermore, normal engine operation leads to changes in compressor and fan airfoil shapes through erosion, corrosion and other means. In addition to geometric variability, perturbations in operating conditions may be simply unavoidable due to the variable environments in which gas turbine engines must operate.

Since little is known in detail about the impact of geometric variability on aerodynamic performance of compressor airfoils, few strategies exist to mitigate the detrimental effects of geometric and operating condition variability on overall compressor performance.

In this work, measured geometric variability from an existing compressor blade is characterized using statistical techniques. The resulting statistical description is used to construct *high-fidelity* models of geometric variability to be used in turn to assess *probabilistically* the impact of geometric noise on airfoil performance. The impact of geometric variability on overall compressor performance is estimated by means of a probabilistic mean-line compressor model. A gradient-based probabilistic optimization methodology for redesigning compressor airfoils is presented and used to redesign three rotor blades.

1.2 Background

Probabilistic techniques applied to structural analysis and design have been in use in the aerospace industry for more than two decades [78]. For instance, NASA has employed probabilistic design methods to assess the reliability of advanced launch systems [16, 111]. Furthermore, NASA has developed a probabilistic structural analysis code, NESSUS (numerical evaluation of stochastic structures under stress), which has been used in static and dynamic analyses of critical structural components of the space shuttle's main engine [87, 109]. The Air Force has likewise been involved in implementing probabilistic design tools in an attempt to decrease the typically large safety factors involved in designing turbine disks [78]. The Air Force has also used probabilistic methods in predicting the life of other critical engine components [129] and airframes [139].

The potential payoffs that may result from judicious application of probabilistic techniques has not escaped the attention of gas turbine engine manufacturers. In the United States, both Pratt and Whitney and General Electric Aircraft Engines have developed probabilistic tools, primarily for structural design. Pratt and Whitney developed a probabilistic design system that brings together deterministic analysis codes and probabilistic methods to address various structural reliability problems [1, 39, 40]. GE Aircraft Engine's AURORA (Approximation Used to Rapidly Obtain Reliability Analysis) system implements a set of techniques collectively known as *fast probability integration* to reduce the computational expense of structural reliability analyses [45, 133]. GE's "Six-Sigma" quality initiative exemplifies the high-level commitment of leading aerospace corporations to the use of statistics and probability throughout their enterprises.

In contrast to the aggressive application of probabilistic techniques to structural analysis and durability, there have been considerably fewer investigations involving *aerothermal* probabilistic analysis and design of turbomachinery components. Probabilistic aerothermal analysis of turbomachinery components is particularly challenging due to the complexity of the physical phenomena encountered. A marked increase in computational requirements appears in direct proportion to the physical complexity of the turbomachinery physics. Until recently, probabilistic treatments of turbomachinery aerothermal analysis and design have

been deemed prohibitively expensive. The advent of relatively affordable parallel hardware is making such considerations possible in a number of practical applications.

Although not particularly abundant in turbomachinery fluid dynamics applications, probabilistic methods are not rare in fluid mechanics at large. For instance, stochastic ideas have found application in the description of turbulent flows [41, 77]. Other examples include recent studies of stochastic versions of Burgers' [12, 43, 64, 132] and Navier-Stokes equations [14] as well as probabilistic treatments of flow in porous media [59]. Recently, attempts to quantify uncertainty in complex fluid-mechanical problems with stochastic inputs have appeared [69].

In the past decade probabilistic methods have been employed in optimizing overall engine cycle parameters as well as individual engine components. For instance, Egorov et al. proposed the use of stochastic optimization techniques for axisymmetric design of axial compressors [10, 31, 32] and other gas turbine engine components [33]. Mavris and coworkers [82, 83] applied probabilistic analysis techniques such as Monte Carlo simulation, fast probability integration and response surface methodology to commercial engine cycle selection.

In recent years, a number of articles dealing with the effects of randomness in aerodynamic shape optimization have appeared. Putko et al. used moment closure methods and Monte Carlo simulation to propagate Mach number and back-pressure uncertainty through a numerical one-dimensional inviscid flow model [101]. Kock et al. implemented a parallel probabilistic analysis and design framework for multidisciplinary optimization and applied it to the preliminary design of a commercial transport aircraft [73]. This work concentrated on preliminary design variables such as wing span, wing area, fuselage length, thrust and weight, rather than on aerodynamic shape design. Huyse demonstrated applied moment closure techniques and statistical decision theory to optimize airfoil shapes in the presence of Mach number uncertainty [61–63]. More recently, Gumbert et al. studied the effect of geometric uncertainty on flexible wing structural design using moment closure methods and a three-dimensional Euler solver [51]. Investigations of the effect of uncertainty on aeromechanical and structural simulation-based design are more numerous than those dealing with aerodynamic shape optimization (e.g., [29, 72, 112]).

Global non-convex optimization methods have also been applied to aerodynamic and turbomachinery shape design, including genetic algorithms [80, 97] and simulated annealing [134, 135]. Despite the initial appeal of these global heuristic methods, their utilization in probabilistic aerodynamic shape optimization is hindered by their typically high computational requirements. Obayashi and Tsukahara [91] presented a comparison of gradient-based, simulated annealing and genetic algorithm methods applied to aerodynamic shape optimization. A family of low-speed NACA airfoils was optimized for maximum lift under two-dimensional inviscid assumptions. The genetic algorithm optimum design was found to produce the best lift coefficient of the three methods, but at six times the cost of the gradient-based method.

Detailed aerodynamic analysis and design requires computer simulations which are often too expensive to be used effectively as part of a design framework. This fact has fueled in recent years the interest on *surrogate-based* optimization methods. A surrogate is a low-order model relating numerical simulation outputs to their inputs. The surrogate (or metamodel) is less expensive to evaluate than the full numerical model and is typically constructed off-line prior to the optimization work. Surrogate optimization relies on the premise that the surrogate, though less accurate, is able to predict the general direction of improvement

which can be advantageously exploited in a constrained optimization algorithm.

Various types of surrogate models have been proposed and used in aerodynamic optimization applications. Among them are polynomial fits, interpolating multivariate splines, kriging models, and neural networks [3, 4, 48, 79, 113, 116]. Garzon and Darmofal used quadratic polynomial surrogates to optimize a transonic compressor airfoil in the presence of geometric variability [44]. Rigorous validation techniques for surrogate model construction in fluid dynamics and heat transfer applications have been presented by Yesilyurt, Otto and coworkers [94, 140].

Although surrogate optimization offers the attractive possibility of simulation-free optimization, the initial construction step may be excessively expensive when a large number of design variables is involved. For instance, the number of simulations required in the construction of a quadratic response surface typically grows exponentially with the number of design variables. In aerodynamic applications, where large numbers of modeshapes are typically employed, this exponential growth in complexity severely hinders the applicability of high-order response surfaces to probabilistic optimization.

Arguably the best-known robust design methods today are those introduced by Taguchi [98]. Taguchi methods (TM) have been in use for more than two decades in the United States as a means to reduce variability in products and processes via parameter redesign [89, 98]. Although used to some degree in the automotive and telecommunications industries, TM have not found wide acceptance in manufacturing industries at large, and are not commonly taught in academic institutions [68]. As pointed out by Parks [96] one of the major limitations of TM is that the underlying assumption of additivity ("linearity") precludes its use in systems dominated by nonlinear interactions. Since such interactions abound in mathematical models of viscous transonic flow applications (as hinted, for instance, by the results presented in Chapters 3–5), TM have not been applied to aerodynamic shape optimization problems.

The impact of corrosion, erosion and ingestion of particulates on gas turbine engine performance has been the subject of various investigations in the past two decades (see for example Ref. [2]). The impact of blade erosion on turbine engine performance has been investigated numerically and experimentally by Tabakoff, Hamed and coworkers [55, 86] among others. Semi-empirical blade erosion models have been proposed by Tabakoff et al. [125].

Among the first rigorous experimental investigations of the effects of leading-edge shape on transonic rotor performance was that of Reid and Urasek [102] in 1973. Using both experimental and numerical techniques Suder et al. [123] found that surface roughness near the blade leading edge results in thicker boundary layers which in turn lead to increased blockage and reduced aerodynamic performance.

The importance of leading-edge shape on engine performance is illustrated by the interest in compressor blade refurbishment operations that offer performance restoration at costs below those of part replacement [35, 103, 105]. The ability to refurbish compressor blades by "recontouring" relies in part in experimental investigations that indicate that chord length variations above the stall chord limit are not significant [104].

1.3 Thesis Objectives

The main objectives of the work reported in this thesis are:

- Construct a high-fidelity model of geometric variability which captures the important features present in data from advanced compressor rotor blades and which is suitable for use in probabilistic analysis and design.
- Employ the model to assess the impact of geometric variability on the aerodynamic performance (profile loss and turning) of transonic compressor blade rows.
- Probabilistically optimize the nominal shapes of compressor airfoils and compare with similarly constrained deterministic redesigns.
- Estimate the impact of geometric variability, including noise amplitude and redesign effects, on the performance of a multistage axial compressor.

1.4 Contributions

The following is a summary of the main contributions of this thesis.

- First application of statistical methods to constructing high-fidelity models of manufacturing variability from surface measurements of existing compressor blades. Using principal component analysis, models of geometric variability suitable for probabilistic analysis and design were constructed from surface measurements of an existing core compressor rotor blade.
- First probabilistic assessment of the impact of geometric variability on aerodynamic performance of compressor blades. The effect of geometric variability found in existing hardware was assessed using Monte Carlo simulation and quasi-two-dimensional cascade analysis codes. Discrepancies between nominal and mean loss coefficient of up to 20% were observed. Loss and turning variability were found to grow linearly with geometric noise amplitude.
- First probabilistic assessment of the impact of blade shape variability on aerothermal performance of multi-stage axial compressors. A probabilistic multi-stage mean-line compressor model was used to estimate the effect of geometric variability on compressor efficiency and pressure ratio. The compressor model included loss coefficient and turning angle statistics derived from the analysis of existing hardware. At five-times the baseline level of blade geometric variability, the discrepancy between nominal and mean polytropic efficiency was found to be about one percentage point. Pressure ratio variability was found to vary linearly with geometric variability amplitude.
- Development of a gradient-based probabilistic optimization method for redesigning compressor airfoils in the presence of geometric variability. Reductions in mean loss coefficient of up to 25% and in loss variability of up to 65% relative to deterministically redesigned airfoils were observed. At the compressor level, compressor simulations using airfoils optimized probabilistically for minimum loss variability exhibited reductions of 30 to 40% in polytropic efficiency variability and nominal-to-mean discrepancy.

1.5 Outline

The thesis follows the order of the aforementioned objectives. Chapter 2 illustrates the use of *principal component analysis*, a well known order-reduction technique, to characterizing and modeling measured geometric variability in compressor blades. Chapter 3 reports the use of probabilistic analysis techniques to assess the impact of geometric variability on the aerodynamic performance of isolated compressor airfoils. Chapter 4 presents a gradient-based probabilistic optimization method for redesigning compressor airfoils in the presence of geometric and inlet flow variability. In Chapter 5, a probabilistic mean-line compressor model is used to assess the impact of geometric variability on overall compressor performance. The last chapter summarizes the contributions of the thesis and offers a few recommendations for future work.

Chapter 2

Characterization of Geometric Variability

Despite general agreement that airfoil shape imperfections are detrimental to aerodynamic performance, limited information can be found in the open literature about their origins and quantitative effects. The lack of characterizations of turbomachinery shape variability is in part due to the random nature of the processes that cause it (i.e., noisy manufacturing processes, foreign object damage, etc.) Nonetheless, high-fidelity models of geometric variability must be constructed in order to assess their impact on aerodynamic performance.

This chapter outlines the basic ideas behind a method to provide such high fidelity models and summarizes its application to the characterization of geometric variability in compressor airfoils. The method, referred to as principal component analysis (PCA), has been used in various fields to reduce the dimensionality of large ensembles of measured or sampled data. In essence, PCA involves finding a statistically optimal basis for representing the scatter of the measured data. PCA results for surface measurements of an existing integrally-bladed rotor are discussed. High-fidelity models of geometric variability suitable for probabilistic analysis and design are constructed. The geometric noise modes resulting from the analysis are found not to correspond in general to customary geometric design and tolerancing parameters of known aerodynamic importance.

In addition to the PCA-based geometric variability model, a leading-edge bluntness mode is introduced to account for airfoil erosion.

2.1 Principal Component Analysis of Airfoil Measurements

Hacker [52] used principal components analysis and other statistical techniques to produce reduced-order models of compressor blade performance. In Hacker's study, heuristically-based models of geometric variability were used in lieu of actual measurements. This section presents results from the application of principal component analysis to a set of actual high-resolution measurements of an high-pressure compressor integrally-bladed rotor (IBR). A two-dimensional analysis is presented in this section. Three-dimensional effects are discussed in Appendix A.

2.1.1 Background

The nominal airfoil geometry is assumed to be defined by p coordinate points $\mathbf{x}_j^0 \in \mathbb{R}^m$, $j = 1, \ldots, p$ where m is typically 2 or 3. Consider a set of n coordinate measurements $\{\hat{\mathbf{x}}_{i,j} \in \mathbb{R}^m \mid i = 1, \ldots, n;\ j = 1, \ldots, p\}$ taken, for instance, with a coordinate-measuring machine. The measurements may correspond to single radial locations ($m = 2$) or entire blade segments ($m = 3$). Index j uniquely identifies specific nominal points and their measured counterparts. Similarly index i identifies a distinct set of measured points, i.e., belonging to a particular blade. The discrepancies from nominal in the coordinate measurements can be expressed as error vectors

$$\mathbf{x}'_{i,j} = \hat{\mathbf{x}}_{i,j} - \mathbf{x}_j^0, \quad i = 1, \ldots, n;\ j = 1, \ldots, p\ .$$

Subtracting from these error vectors their ensemble average

$$\bar{\mathbf{x}}_j = \frac{1}{n} \sum_{i=1}^{n} \mathbf{x}'_{i,j}, \quad j = 1, \ldots, p\ ,$$

gives a centered set of m-dimensional vectors, $\mathcal{X} = \{\mathbf{x}_{i,j} = \hat{\mathbf{x}}_{i,j} - \bar{\mathbf{x}}_j \mid i = 1, \ldots, n;\ j = 1, \ldots, p\}$. Writing the m-dimensional measurements in vector form, $\mathbf{X}_j = [\mathbf{x}_{1,j}^T, \ldots, \mathbf{x}_{n,j}^T]^T$, the *scatter matrix* of set $\mathcal{X}$ is given by

$$\mathbf{S} = \mathbf{X}^T\mathbf{X}.$$

The scatter matrix is related to the covariance matrix $\mathbf{C}$ via $\mathbf{C} = (n-1)^{-1}\mathbf{S}$.

It can be shown (see Appendix A or standard references such as [100] and [67]) that the directions along which the scatter is maximized correspond to non-trivial solutions of the eigenvalue problem

$$\mathbf{S}\mathbf{v} = \lambda\mathbf{v}. \tag{2.1}$$

Because $\mathbf{S}$ is symmetric positive definite, it has in general mp orthonormal eigenvectors $\mathbf{v}_i \in \mathbb{R}^{mp}, i = 1, \ldots, mp$ with corresponding real, non-negative eigenvalues $\lambda_i, i = 1, \ldots, mp$ [130]. The eigenvector corresponding to the largest eigenvalue indicates the direction along which the scatter of the data is maximized. The eigenvector corresponding to the next largest eigenvalue maximizes the scatter along a direction *normal* to the previous eigenvector. It is in this sense that it is said that the eigenvectors of $\mathbf{S}$ provide an *optimal* statistical basis for the decomposition of the scatter of the samples.

The total scatter (or *energy* [8]) E of the data in set $\mathcal{X}$ can be shown to be (see Appendix A)

$$\mathsf{E} \equiv \mathrm{tr}(\mathbf{X}^T\mathbf{X}) = \sum_{j=1}^{mp} \lambda_j\ .$$

In other words, the total scatter of the data set is given by the sum of the eigenvalues of the scatter matrix $\mathbf{S}$.

The PCA synthesis of $\mathbf{S}$ can be shown to be equivalent to the *Singular Value Decomposition* (SVD) of $\mathbf{X}$ in reduced form [130],

$$\mathbf{X} = \mathbf{U}\mathbf{\Sigma}\mathbf{V}^T\ , \tag{2.2}$$

where $\mathbf{\Sigma} = \text{diag}(\sigma_1, \ldots, \sigma_{mp})$, $\sigma_j = \sqrt{\lambda_j}$, $j = 1, \ldots, mp$ and the columns of $\mathbf{V}$ are the corresponding eigenvectors of $\mathbf{S}$. The columns of $\mathbf{A} = \mathbf{U\Sigma}$ are called the amplitude vectors or *principal components* of the data set $\mathcal{X}$ (see Appendix A). The SVD of $\mathbf{X}$ is made unique by requiring that $\{\sigma_j\}_{j=1}^{mp}$ be a non-increasing sequence.

2.1.2 Application

As an application of the PCA formalism outlined above, an integrally-bladed rotor (IBR) consisting of 56 nominally identical blades with inlet tip radius of 9.87 inches and tip-to-hub ratio of 1.172 is considered. The IBR is part of an industrial design axial compressor. The measurements correspond to parts fabricated via flank-milling [138]. Surface measurements of blades from four separate rotors (150 blades in total) were taken using a scanning coordinate-measuring machine (CMM).[1] Each blade was measured at 13 different radial locations. The scanning CMM measurements of each radial station were condensed to 112 points. Axial elongation and untwisting of the blade due to centrifugal forces and thermal loading incurred during operation are assumed small and neglected in the current analysis of geometric variability, as well as in the subsequent aerothermal analyses.

For the present application the 13 separate cross-sectional measurements were stacked together to form a three-dimensional representation of the measured portion of the blade. Using bicubic spline interpolation [21] the nominal geometry, as well as each measured blade, were "cut" along a mid-span axial streamline path of varying radius (see Section 3.3.1). The resulting sets of points are further modified by removing nine points (five from the suction and four from the pressure sides) around the trailing edge, as shown in Fig. 2-1, to produce an airfoil with a blunt trailing edge as required by the blade passage analysis code (see Sect. 3.1.2 and Ref. 27).

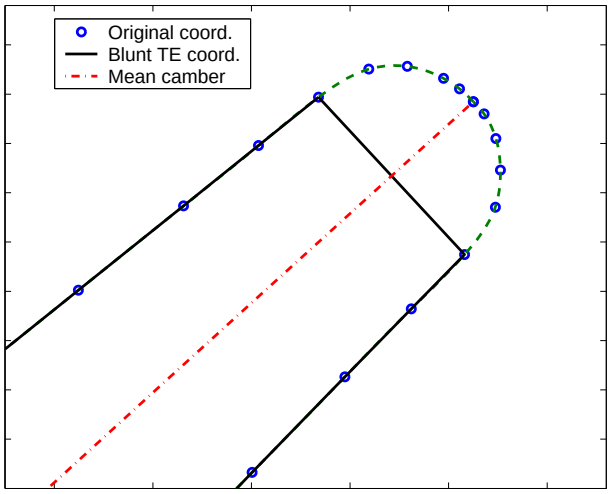

Figure 2-1: Schematic blunt trailing edge modification

Using the notation introduced above, the resulting set $\mathcal{X}$ of two-dimensional mean-centered measurement vectors can be written as $n \times mp$ matrix $\mathbf{X}$ where $n = 224$, $m = 2$ and $p = 103$. The SVD of $\mathbf{X}$ produces diagonal matrix $\mathbf{\Sigma}$ of singular values $\sigma_i = \sqrt{\lambda_i}$

[1] Section 2.3 in Appendix A discusses the impact of number of samples on PCA results.

(arranged in non-increasing order) and orthonormal matrix $\mathbf{V}$ of eigenvectors of the scatter matrix $\mathbf{S}$.

Figure 2-2(a) shows the modal scatter fraction $\lambda_k / \sum_{i=1}^{mp} \lambda_i$ (decreasing) and the partial scatter $\sum_{i=1}^{k} \lambda_i / \sum_{i=1}^{mp} \lambda_i$ (increasing) of the first six eigenmodes of $\mathbf{S}$. The first mode contains 79% of the total scatter in the original measurement set and it clearly dwarfs the scatter fraction of the other modes. For instance, the scatter corresponding to the second most energetic mode is eight times smaller in magnitude than the first.

Figures 2-2(b)–(d) show the directions along which the first three eigenmodes of $\mathbf{S}$,

$$\mathbf{x}_i = \mathbf{x}^0 + \bar{\mathbf{x}} + \sigma_i \mathbf{v}_i, \quad i = 1, 2, 3 \ . \tag{2.3}$$

act with respect to the average geometry $\mathbf{x}^0 + \bar{\mathbf{x}}$. More details of eigenmodes 1, 3 and 6 are shown in Figs. 2-4, 2-5 and 2-6 respectively. An additional scaling factor indicated at the top of each figure was used to distinguish the effect of the eigenmode from the mean geometry. Only the positive mode amplitude contribution is depicted in the figures. Figure 2-4 indicates that the main effects of mode 1 are uniform thickening of the airfoil and azimuthal translation. Mode 3, on the other hand, exhibits a thinning of the airfoil on the suction surface away from the leading edge, with the shape of the latter being maintained. Mode 6 shows more localized effects at both the nose and tail of the airfoil, i.e., a distortion of the leading edge characterized by thickening and the appearance of a bulge on the pressure side. The perturbations on the airfoil nose are noteworthy as the aerodynamic performance of transonic airfoils is known to be sensitive to leading-edge shape and thickness. At the tail of the airfoil, mode 6 causes an increase in thickness and the appearance of ripples on both the suction and pressure surfaces.

Figure 2-2(a) indicates that the first six modes, when combined contain 99% of the total scatter present in the sample. Figure 2-3 depicts the first 50 eigenvalues of $\mathbf{S}$, showing that they decrease in amplitude exponentially fast. This rapid decrease in relative energy of the higher modes suggests that a reduced-order model containing only the first few modes may be sufficient to represent most of the geometric variability contained in the original set of measurements. The construction of such a model is discussed in Sect. 2.2.

The description of modes 1, 3 and 6 suggests a decomposition of the PCA modes into geometric parameters of known aerodynamic and aeromechanic importance. Table 2.1 summarizes percent changes in maximum thickness, maximum camber, leading-edge radius, chord length and cross-sectional area, as well as trailing-edge deflection angles for the first six eigenmodes. In computing the parameter values, the PCA modes were scaled as in Eq. (2.3). The parameter values, except for trailing-edge angle, were computed with XFOIL, an isolated airfoil design and analysis code developed by Drela and Youngren [28]. Trailing-edge angle changes were calculated by comparing mean camber line angles in the vicinity of the trailing edge (5% of the camber line arclength). The row labeled "mean" contains the changes corresponding to the average airfoil, $\bar{\mathbf{x}}$. Table 2.1 suggests that modes 2 and 4 exhibit non-negligible changes in maximum thickness, while modes 4 and 5 cause the largest relative changes in trailing-edge angle. Although to a lesser degree than the mean geometry, modes 2 and 5 also impact the maximum camber. The dominant contribution to leading-edge radius change in the measurement data can be ascribed to the average airfoil. On the other hand, the measured airfoils do not show substantial changes in chord length from the design intent. In summary, it is not clear that any one mode leads to a dominant change in a particular geometric feature; rather each mode contributes to changes in some

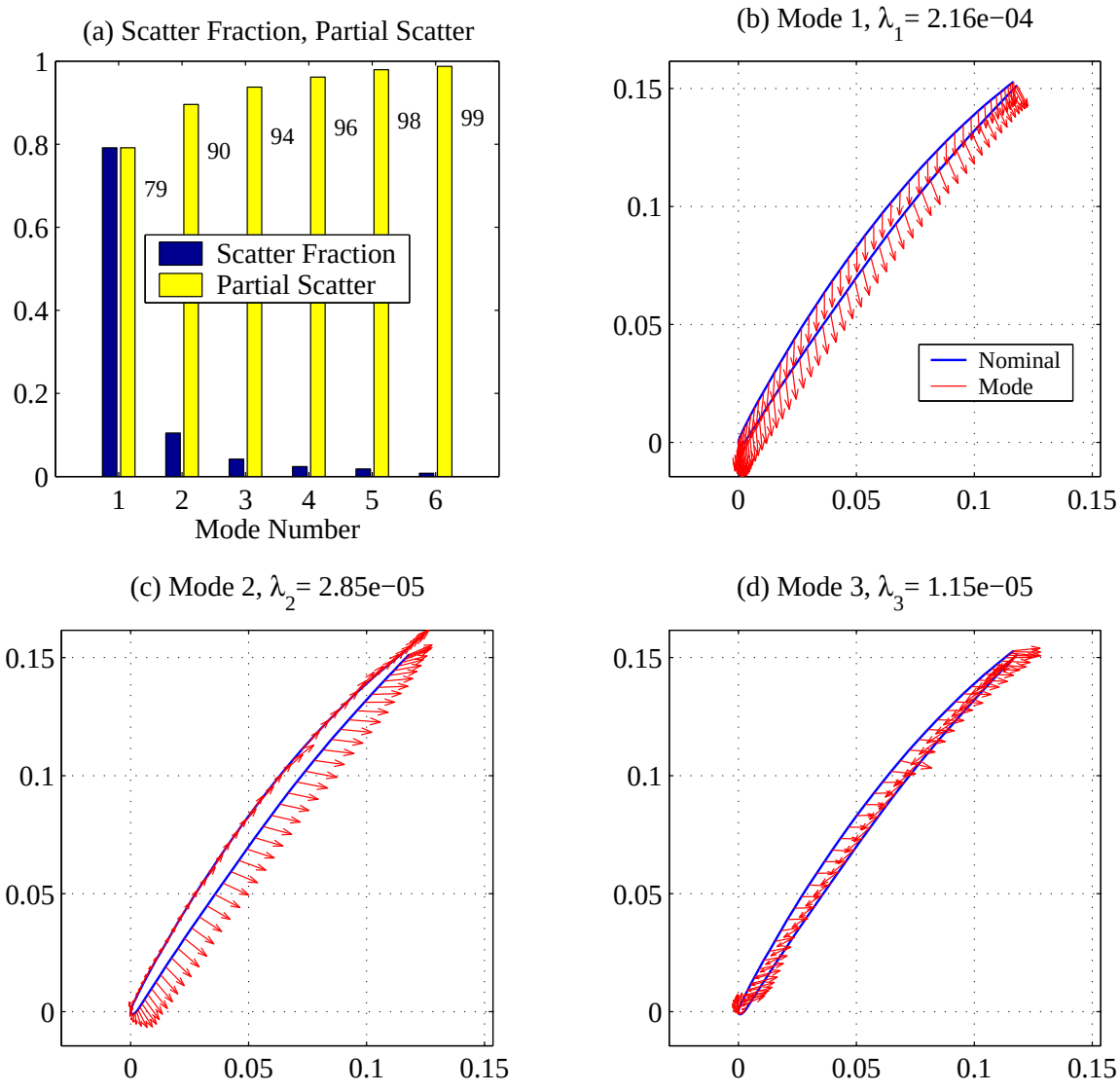

Figure 2-2: IBR mid-span section: PCA modes

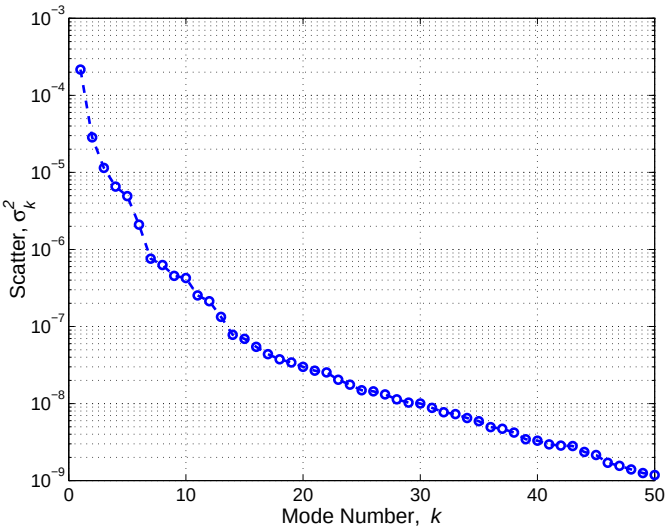

Figure 2-3: Exponential decay of the eigenvalues of **S**

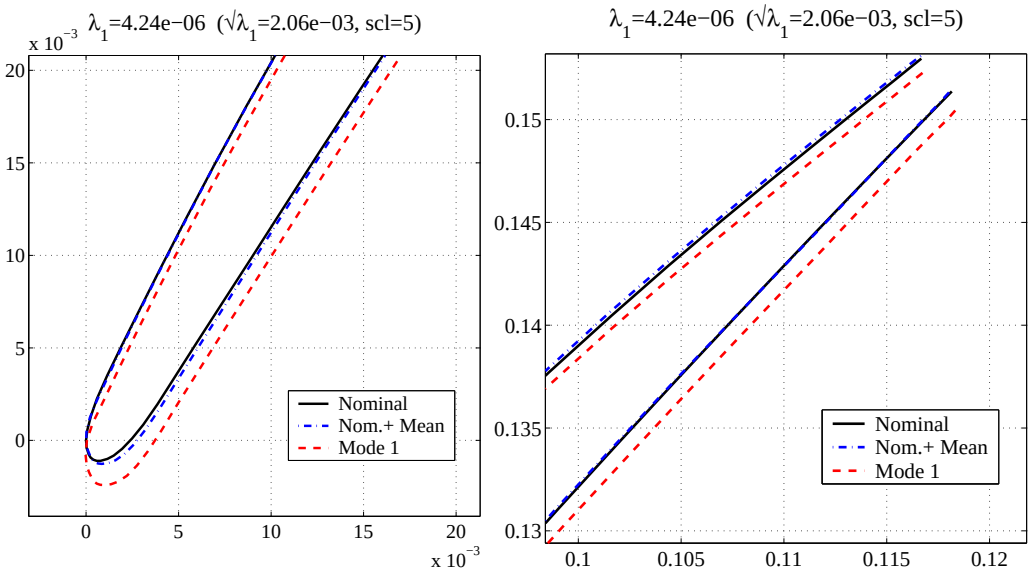

(a) Leading edge

(b) Trailing edge

Figure 2-4: IBR mid-span section: Scaled mode 1 (positive)

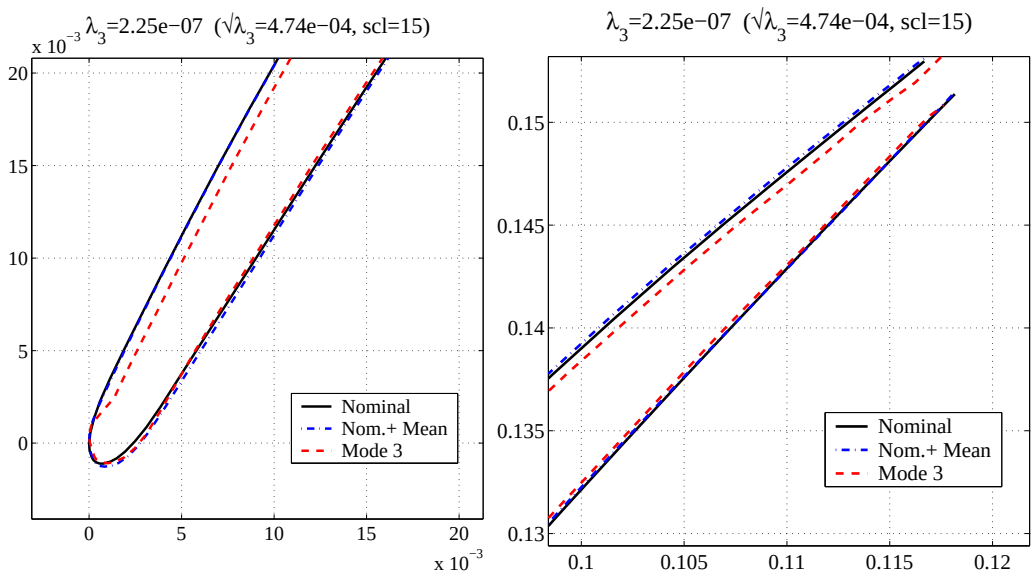

(a) Leading edge (b) Trailing edge

Figure 2-5: IBR mid-span section: Scaled mode 3 (positive)

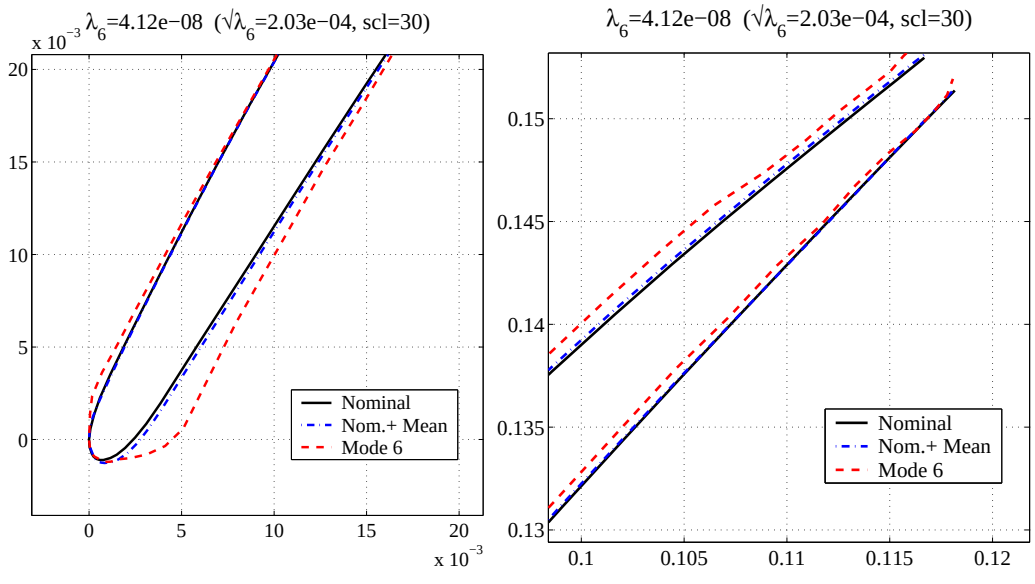

(a) Leading edge (b) Trailing edge

Figure 2-6: IBR mid-span section: Scaled mode 6 (positive)

Table 2.1: IBR mid-span section: Geometric features of PCA modes. Numbered entries are percentage changes with respect to the average airfoil geometry, $\mathbf{x}^0 + \bar{\mathbf{x}}$. TE angle entries are given in degrees. The average geometry is compared to the nominal airfoil.

Mode	Max Thickness (%Δ from $\mathbf{x}^0$)	Max Camber (%Δ from $\mathbf{x}^0$)	LE Radius (%Δ from $\mathbf{x}^0$)	TE Angle (Δ deg from $\mathbf{x}^0$)	Chord (%Δ from $\mathbf{x}^0$)	Area (%Δ from $\mathbf{x}^0$)
Avg	-0.12	-0.98	18.33	0.06	-0.04	-1.03
1	-0.54	-0.06	-4.22	0.00	-0.04	-0.77
2	-1.09	0.28	2.15	0.04	-0.04	-1.27
3	0.53	0.04	1.83	-0.02	0.01	0.85
4	-0.74	0.10	1.34	-0.07	0.02	-0.87
5	-0.11	0.27	4.23	0.06	0.02	-0.01
6	0.03	-0.01	-4.11	0.01	0.00	-0.08
7	0.06	-0.03	3.04	-0.02	0.00	0.02
8	-0.04	0.16	0.65	0.00	0.00	-0.05

of the features to greater or lesser extent.

The above suggests a characterization of actual manufacturing variability involving statistical mode shapes to complement customary tolerancing parameters. Further, by linking individual mode shapes to their impact on aerodynamic performance, a functionally based tolerancing scheme could be devised. This issue will be discussed further in Chapter 3 which addresses the impact of geometric variability on aerodynamic performance of compressor airfoils.

2.2 PCA-Based Models of Geometric Variability

A high-fidelity model of the geometric variability present in $\mathcal{X}$, for use in CFD-based probabilistic aerodynamic analysis, is motivated as follows. Let $Z_i,\ 1 = 1, \ldots, mp$ be independent, identically distributed random variables from $\mathcal{N}(0, 1)$ (normally distributed with zero mean and variance one). By linearity the random vector

$$X = \mathbf{x}^0 + \bar{\mathbf{x}} + \sum_{i=1}^{mp} \sqrt{\lambda_i} Z_i \mathbf{v}_i \tag{2.4}$$

has mean $\mathbf{x}^0 + \bar{\mathbf{x}}$ and total scatter $\sum_{i=1}^{mp} \lambda_i = \mathsf{E}$, i.e., a set of instances of X will have the same mean and unbiased estimator of the variance, as the set of measurements $\mathcal{X}$. Furthermore, the number of samples of X for use in probabilistic analysis, N, can be large; for instance in Monte Carlo simulation $N \gg mp$ may be required (see Chapter 3).

A reduced-order model of $\mathbf{X}$ may be useful in preliminary analyses or when techniques

other than Monte Carlo simulation are to be employed (e.g., moment methods, response surfaces, etc). The rapid decay of the eigenvalues of the scatter matrix of the data (Fig. 2-3) suggests a reduced-order model of X of the form

$$\tilde{X} = \mathbf{x}^0 + \bar{\mathbf{x}} + \sum_{i=1}^{K} \sqrt{\lambda_i} Z_i \mathbf{v}_i$$

where $K < mp$ is a free truncation parameter. For large enough N, as K increases from unity the total variance of $\tilde{X}$ approaches that of X. In fact, the total scatter of a finite set of instances of $\tilde{X}$ is bounded by $\sum_{i=1}^{K} \lambda_i \leq \mathsf{E}$.

As discussed in the next Chapter, although the geometric variability present in measurement samples may be well described by the first few PCA modes, assessing its impact on aerodynamic performance may require including a larger number of modes in the model of geometric variability.

A PCA-based high-fidelity model obtained for the IBR airfoil is used in Chapter 3 to assess probabilistically the impact of manufacturing variability on aerodynamic performance. The impact of individual modes and noise amplitude are also addressed in that Chapter.

2.3 PCA Results Vs. Number of Samples

In the application of PCA to compressor rotor blade measurements discussed above, all available samples (150) were used in the analysis. This section discusses how PCA results (covariance matrix eigenvalues) vary according to the number of samples being considered. For instance, given n measurement samples, there are $\binom{n}{k}$ different ways of selecting $k \leq n$ among them.[2]

Figure 2-7 depicts convergence trends of the first four eigenvalues of the covariance matrix for k measured samples. The average value and standard deviation of each eigenvalue are computed from $\min\left[\binom{n}{k}, 10^4\right]$ random permutations of the indices $\{1 \ldots n\}$. For each random permutation the eigenvalues of the covariance matrix of the corresponding indexed measurements is computed via singular value decomposition. In Fig. 2-7 the average eigenvalues are shown as solid lines and a one-standard-deviation interval about the mean by dashed lines. Table 2-7 shows mean and standard deviation values for the first 12 covariance matrix eigenvalues for 5, 10, 60 and 150 samples. As shown in Fig. 2-7 and further illustrated in Table 2-7, the uncertainty of the first computed covariance matrix eigenvalue is very large for small sample sizes, and decreases monotonically as the sample size is increased. Figure 2-7(d) indicates that the likelihood that a sample subset consisting of less than ∼20 randomly-selected samples will be sufficient to approximate the fourth eigenvalue to within 10% is rather small. It follows that in order to reduce the uncertainty of the PCA due to sample size to acceptable levels, a large fraction of the total number of samples must be considered.

[2] $\binom{n}{k}$ or "*n choose k*" is defined for $k \leq n$ by [108]

$$\binom{n}{k} := \frac{n!}{(n-k)!k!}$$

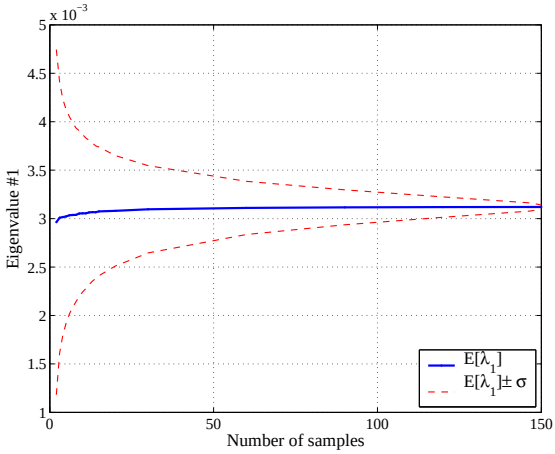

(a) Eigenvalue No. 1

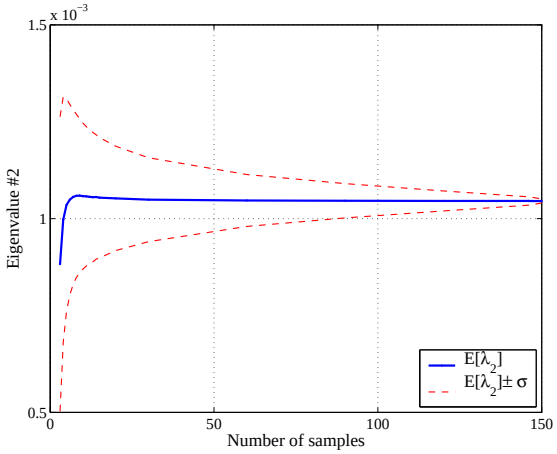

(b) Eigenvalue No. 2

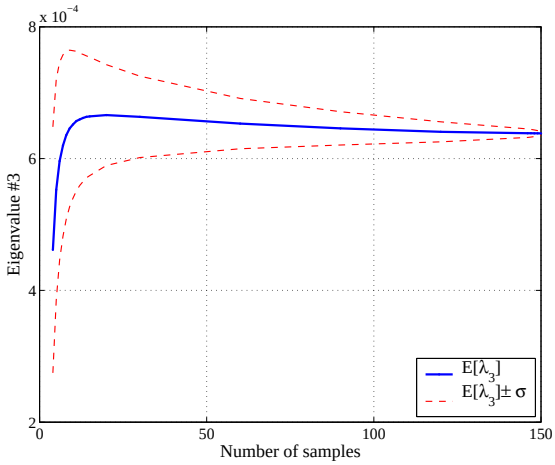

(c) Eigenvalue No. 3

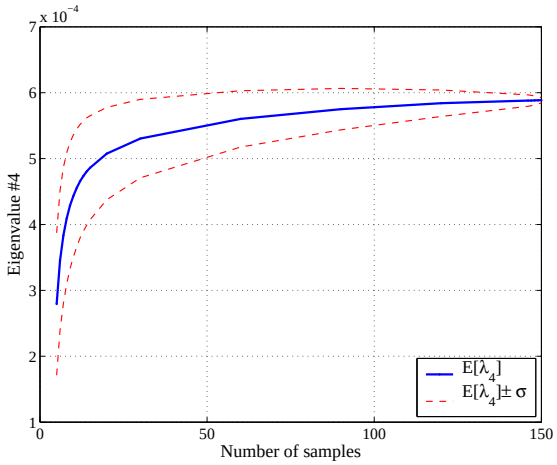

(d) Eigenvalue No. 4

Figure 2-7: Eigenvalues of covariance matrix versus number of samples

Table 2.2: Eigenvalues covariance matrix versus number of samples

N_{smpl}	5		10		60		150	
n	$\mathbb{E}[\lambda_n]$ $\times 10^3$	σ_{λ_n} $\times 10^3$	$\mathbb{E}[\lambda_n]$ $\times 10^3$	σ_{λ_n} $\times 10^3$	$\mathbb{E}[\lambda_n]$ $\times 10^3$	σ_{λ_n} $\times 10^3$	$\mathbb{E}[\lambda_n]$ $\times 10^3$	σ_{λ_n} $\times 10^3$
1	3.0219	1.1010	3.0546	0.8124	3.1103	0.2745	3.1198	0.0192
2	1.0353	0.2741	1.0580	0.1883	1.0467	0.0669	1.0454	0.0047
3	0.5528	0.1675	0.6518	0.1118	0.6531	0.0382	0.6383	0.0029
4	0.2793	0.1080	0.4434	0.0925	0.5602	0.0427	0.5886	0.0039
5			0.2840	0.0666	0.4083	0.0355	0.4214	0.0025
6			0.1786	0.0369	0.2142	0.0164	0.2119	0.0012
7			0.1258	0.0246	0.1794	0.0153	0.1907	0.0013
8			0.0908	0.0184	0.1310	0.0083	0.1306	0.0007
9			0.0629	0.0147	0.1126	0.0074	0.1152	0.0007
10					0.0975	0.0062	0.1006	0.0006
11					0.0848	0.0060	0.0927	0.0006
12					0.0712	0.0043	0.0725	0.0004

2.4 Other Methods of Describing Geometric Noise

As pointed out earlier, the statistical characterization afforded by principal component analysis can be used in modeling geometric variability for probabilistic simulation and optimization purposes. However, high-resolution measurements of new or used airfoils are not available in many turbomachinery design situations. In the absence of this type of data, heuristic information such as expert opinion and past experience may be used in describing geometric variability. Furthermore, known statistical characterizations may be used to construct geometric variability models for similar airfoils (e.g., airfoils fabricated by the same process).

Examples of additional geometric modes of possible aerodynamic interest to probabilistic simulations include perturbations to thickness and camber distributions, twist, leading-edge shape perturbations, overall chord-length changes, trailing-edge angle variations, etc. The aerodynamic performance of transonic and supersonic airfoils is sensitive to thickness distribution, particularly to the value and location of its maximum. For instance, in axial compressor blade passages the maximum thickness influences the shock structure and flow passing capabilities. Similarly, transonic airfoils are sensitive to variations in leading-edge thickness and shape, as pressure distribution, boundary layer transition, separation and reattachment depend to some degree on the shape of the leading-edge.

Thickness, camber, leading edge bluntness and twist modes are used in the sequel to model airfoil geometric variability when manufacturing or wear data are not available. The thickness perturbation consists of a smooth distribution acting along the directions normal to the suction or pressure surfaces of the airfoil. The thickness distribution is given by

$$f(x) = ax^{\alpha-1}(1-x)^{\beta-1}$$

for $0 < x < 1$, where α and β are distribution parameters which control the location of

maximum thickness increase and how fast the mode dies out as it approaches the leading and trailing edges. The parameter a controls the amplitude of the thickness perturbation. Figure 2-8(a) shows the effect of applying the thickness mode with parameters $a = 0.01$ chord lengths, $\alpha = \beta = 4$ to a sample compressor airfoil. Figure 2-8(a) also shows the effect of twist which under the present two-dimensional restriction is implemented as a solid-body rotation about the airfoil's centroid.

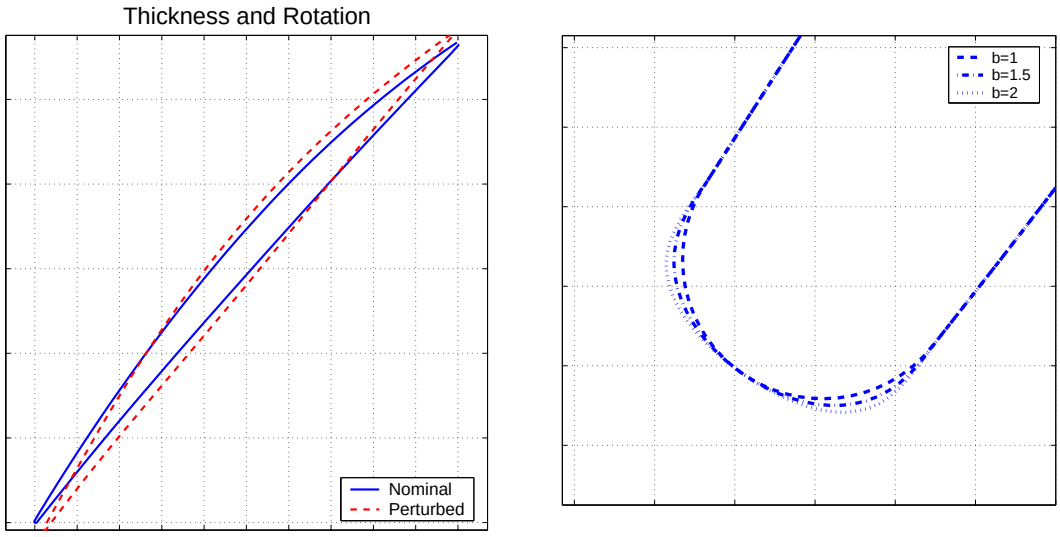

(a) Thickness, twist

(b) Leading edge bluntness

Figure 2-8: Thickness, twist and leading-edge bluntness

Leading edge shape variability is of particular interest in assessing the impact of wear on airfoil performance. Aircraft engines, for instance, ingest foreign particles that erode the leading edges of fan and compressor blades [102]. A leading-edge bluntness mode is implemented by fitting a profile to the "nose" of the airfoil section. The profile is defined by

$$g(x) = [4x(1-x)]^{1/b}$$

for $0 < x < 1$ where $b \geq 1$ serves a "bluntness" parameter. For $b = 1$, $g(x)$ is a concave-down parabola centered at $x = 1/2$ with maximum value of 1. As b increases so does the bluntness of the leading edge. Only values of b greater than or equal to unity are pertinent to the present application. Figure 2-8(b) shows the nose of an airfoil to which three different profiles with b values of 1, 1.5 and 2 have been fitted.

Although the other heuristic geometric noise modes discussed here can be assumed to be normally distributed, the impact of erosion on the leading edge is more likely to result in an increase, rather than a reduction, of the leading-edge radius [104]. It follows that a symmetric distribution (as is the Gaussian distribution) that equally favors smaller and larger leading edge radii is not appropriate. Therefore, bluntness is modeled here as a

random variable X_b with Beta probability density, i.e.,

$$f_{X_b}(x) = \begin{cases} \frac{x^{\alpha-1}(1-x)^{\beta-1}}{B(\alpha,\beta)} & , \ 0 < x < 1 \\ 0 & , \ \text{otherwise} \end{cases}$$

where

$$B(\alpha,\beta) = \int_0^1 x^{\alpha-1}(1-x)^{\beta-1}dx = \frac{\Gamma(\alpha)\Gamma(\beta)}{\Gamma(\alpha+\beta)} \ .$$

The mean and variance of X_b thus defined can be shown to be [108] (see also Chapter 3)

$$\mathbb{E}[X_b] = \frac{\alpha}{\alpha+\beta} \ , \qquad \text{Var}(X_b) = \frac{\alpha\beta}{(\alpha+\beta)^2(\alpha+\beta+1)}.$$

The amount of asymmetry or *skewness* of X_b—as indicated by its third central moment—can be found to be [88]

$$\frac{2(\beta-\alpha)\sqrt{\alpha+\beta+1}}{(\alpha+\beta+2)\sqrt{\alpha\beta}} \ .$$

As suggested in Refs. 105 and 103, the leading-edge radius of eroded airfoils has been observed to increase to twice the baseline value. The amount of leading-edge shape distortion will depend on many factors such as thickness distribution and wear rate. A continuous Beta distribution in the interval $[0.8, 2.0]$ with parameters $\alpha = 2$, $\beta = 4$ is assumed for the leading-edge bluntness mode. Figure 2-9 shows the density function of X_b for the chosen parameters; the dashed line indicates the location of the mean value. The standard deviation and skewness of X_b are 0.21 and 0.81 respectively, indicating that the distribution of X_b is weighed toward values higher than the average.

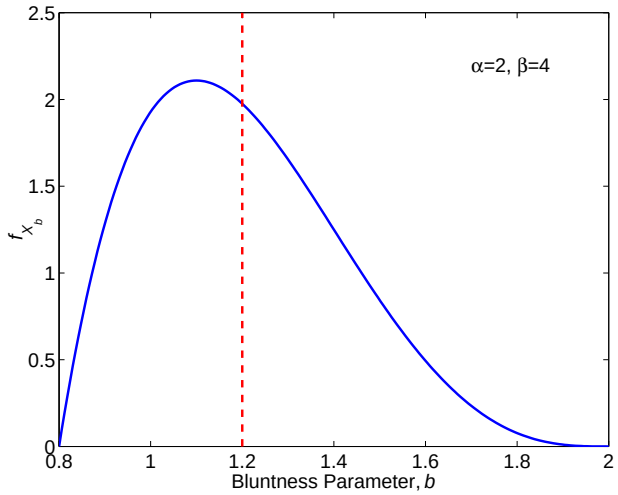

Figure 2-9: Aerodynamic performance trends and bluntness parameter density

The selection of input statistics for the discrete modes mentioned above is discussed in Chapter 3 as part of assessing their impact to aerodynamic performance of isolated compressor airfoils.

2.5 Summary

This chapter outlines a procedure for characterizing the geometric variability of compressor blades by means of Principal Component Analysis (PCA). PCA is a technique used in various fields to reduce the dimensionality of large ensembles of measured or sampled data. In the present context PCA is used to obtain high-fidelity and reduced-order models of geometric variability from compressor airfoil measurements. The high-fidelity statistical characterization thus afforded provides a model of geometric variability suitable for probabilistic simulation and optimization. PCA results for CMM measurements of an existing integrally-bladed rotor were presented. The geometric variability in the original sample was found to be well represented with less than ten discrete modes. The geometric noise modes were found in general not to correspond uniquely to single geometric design and tolerancing parameters of known aerodynamic importance. Additional modes of geometric variability pertaining to airfoil wear were also discussed.

Chapter 3

Impact of Geometric Variability On Compressor Blade Aerodynamics

Numerical codes implementing techniques from computational fluid dynamics (CFD) have for many year been used to analyze and design turbomachinery blading. However, there have been few rigorous attempts to use CFD tools to assess the impact of geometric variability on compressor blading performance, due primarily to the excessive computational expense involved. In this Chapter, the quasi-2D flow analysis code MISES was used as part of a probabilistic analysis framework to assess the impact of geometric and inlet flow condition uncertainty on the aerodynamic performance of transonic compressors. Blade row total pressure loss coefficient and turning were the selected measures of aerodynamic performance. Three rotor blades are considered, with inlet Mach numbers in the range of common high pressure axial compressor operation. The inlet Mach numbers considered are 0.82, 0.90 and 1.25. The geometric noise models are based on the PCA results of Chapter 2. The input variability is found to affect the expected values of loss and turning as well as their the uncertainty. It is observed that the amplitude of the geometric noise variability is linearly related to increase of output variability. The relative mean-shift—or difference between the nominal and expected values—is found to be larger in the subsonic-inlet cases than in the supersonic one, but the latter exhibits more variability in both loss coefficient and turning. The relative contribution of the average geometry of the noise model to mean shift decreases as the noise variability is increased.

3.1 Aerodynamic Performance Assessment

3.1.1 Background

The aerodynamic performance of a compressor rotor may be summarized by the changes in total enthalpy and entropy in the flow across the blade row, i.e., the amount of work transfered to the fluid and the losses (profile, endwall, shock) accrued in the process.

Applying the first law of thermodynamics and conservation of angular momentum to a control volume surrounding a stream-tube across the blade passage leads to the Euler

turbine equation

$$\Delta h_t = \omega(r_2 v_2 - r_1 v_1) \ , \tag{3.1}$$

where Δh_t denotes the change in total enthalpy; ω, r and v denote wheel speed, radius and flow velocity, and the subscripts 1 and 2 stand for inlet and exit respectively. Eq. (3.1) relates the change in total enthalpy per unit mass Δh_t to the change in angular momentum per unit mass across the passage. For small radial changes across the blade row, Eq (3.1) reduces to

$$\Delta h_t = \omega r \left[u_1 \tan\beta_1 - u_2 \tan(\beta_1 + \vartheta) \right]$$

where u and β are the the axial flow velocity and relative flow angle respectively and ϑ denotes the flow turning, $\vartheta \equiv \beta_2 - \beta_1$.

An appropriate choice for a measure of loss in an adiabatic machine is entropy generation [23]. The increase in entropy results in a decrease of the stagnation pressure rise compared to the ideal (isentropic) value. In what follows the loss coefficient is defined as the drop in total pressure from the ideal value at passage exit scaled by the difference between inlet total and static pressure,

$$\varpi = \frac{p^0_{T_2} - \bar{p}_{T_2}}{p_{T_1} - p_1} \ . \tag{3.2}$$

In Eq. (3.2), $p^0_{T_2}$ is the ideal (isentropic) total pressure at the passage exit,

$$p^0_{T_2} = \frac{\gamma - 1}{\gamma} h_0 \rho_{0_{\text{ref}}} \left(\frac{h_0}{\mathbf{I}} \right)^{\frac{1}{\gamma - 1}} .$$

The *rothalpy*, $\mathbf{I}$,

$$\mathbf{I} = h + \frac{|\mathbf{u}|^2}{2} - \frac{(\Omega r)^2}{2}$$

is invariant in the rotating frame of reference and $h_0 = \mathbf{I} + \frac{1}{2}(\Omega r)^2$, where Ω is the wheel speed and r the streamtube radius. In MISES the reference quantity $\rho_{0_{\text{ref}}}$ is taken to be unity. Finally $\bar{p}_{T_2}$ is the mass-averaged total pressure at the passage exit. Details of MISES' cascade loss calculation can be found in Appendix C of Ref. 141.

3.1.2 Blade row aerodynamic analysis: MISES

MISES (Multiple blade Interacting Streamtube Euler Solver) is an interactive quasi-two-dimensional viscous flow analysis package [27] used for turbomachinery analysis and design. MISES' flow solver, ISES can be used to analyze and design single or multi-element airfoils over a wide range of flow conditions. ISES incorporates a zonal approach in which the inviscid part of the flow is described by the projection of the steady-state 3-D Euler equations onto an axisymmetric stream-surface of variable thickness and radius. The resulting two-dimensional equations are discretized in conservation form over a streamline grid. The viscous parts of the flow (boundary layers and wake) are modeled by means of a two-equation integral boundary layer formulation [24]. The viscous and inviscid portions of the flowfield are coupled through the displacement thickness and the resulting nonlinear system of equation is solved using the Newton-Raphson method [141].

ISES can model transitional, trailing-edge and shock-induced separation [141] and recent modifications allow for boundary layer suction and blowing [85]. MISES has recently been used to design high-pressure ratio conventional and counter-rotating compressors [70, 85] as

well as aspirated fan stages [114]. Preliminary MISES results from the present study were used by Häcker [52] to create reduced order models of the impact of shape variability on compressor blade performance.

A feature of MISES that is particularly relevant to probabilistic analysis is its speed. For the cases discussed herein, typical execution times are 3 to 10 seconds per trial on a current commodity CPU. [1].

3.2 Probabilistic Analysis

Conceptually, the computed loss coefficient and turning may be seen as functions of n independent variables representing the geometry of the flow passage and m variables representing other flow parameters,

$$\varpi = \varpi(x, y), \quad \vartheta = \vartheta(x, y)$$

where $x \in \mathbb{R}^n$ denotes the vector of geometric parameters and $y \in \mathbb{R}^m$ contains the remaining parameters. Both ϖ and ϑ are deterministic functions of x and y, that is, for given x and y, there is a unique value of ϖ.

Consider next a continuous random vector X with joint probability density function f_X [108]. For fixed flow parameters y, the expected value of $\varpi(X, y)$ is defined by

$$\mu_\varpi := \mathbb{E}_X[\varpi(X, y)] = \int_{\mathbb{R}^n} \varpi(X, y) f_X(x)\, dx \ , \tag{3.3}$$

and the variance of $\varpi(X, y)$ is given by

$$\sigma_\varpi^2 := \mathrm{Var}(\varpi(X, y)) = \mathbb{E}_X[(\varpi(X, y) - \mu_\varpi)^2] \ . \tag{3.4}$$

Similar expressions follow for mean μ_ϑ and variance σ_ϑ^2 of turning. It is often useful in comparing the variability of outputs with dissimilar expected values to consider their coefficient of variability (COV), defined as the ratio of the standard deviation to the mean of a given random variable, e.g. the COV of loss coefficient is defined to be

$$V_\varpi := \frac{\sigma_\varpi}{\mu_\varpi} \ .$$

In general the functional dependence of ϖ on the geometric parameters x is too involved to allow for closed form evaluation of the integrals in definitions (3.3) and (3.4). However, numerical approximations can be obtained via numerical probabilistic analysis techniques. One such technique, the Monte Carlo method, is described below and later applied to estimating the effect of geometric and inlet flow condition variability for three compressor airfoils. Garzon and Darmofal [44] applied and compared two other probabilistic analysis techniques, response surface methodology and probabilistic quadrature, to assessing the impact of geometric variability on aerodynamic performance. In that study, probabilistic quadrature outperformed quadratic response surfaces in predicting mean and standard deviation of loss coefficient. Mean loss coefficient predictions by probabilistic quadrature were in good agreement with Monte Carlo predictions, but standard deviations were in general under-predicted.

[1] Intel 1.8 GHz Xeon processor

3.2.1 Monte Carlo Simulation

The systematic application of Monte Carlo method to scientific problems dates from the 1940s (see Ref. [56], Sect. 1.2 for a more detailed historical account). During World War II Monte Carlo methods were used to solve neutron diffusion problems. After the war Ulam, Fermi and von Neumann showed how Monte Carlo methods can be used to obtain approximate solutions to otherwise intractable deterministic problems [56].

Monte Carlo methods are numerical techniques used to approximate multivariate integrals via statistical sampling, a procedure also known as *random quadrature* [128]. The Monte Carlo method can be applied to both deterministic and probabilistic problems. Applications of the former type include approximating multidimensional integrals [37] and solving partial differential equations numerically [50, 53, 110]. In the present context the Monte Carlo method is used to estimate probabilistic moments (mean and variance) of deterministic functions having random arguments, that is, mean and variance of loss coefficient and turning for compressor blade rows subjected to geometric variability.

A frequently used unbiased estimator of the mean of a function g of one random variable X is the arithmetic average, i.e., for sample size N the estimator of the mean of $g(X)$ is simply

$$\hat{\mu}_g = \frac{1}{N}\sum_{i=1}^{N} g(x_i)$$

which has standard error

$$\sigma_{\hat{\mu}_g} = \frac{\sigma_g}{\sqrt{N}}$$

where σ_g is the standard deviation of $g(X)$. In practice σ_g is not generally known, however it can be approximated with the unbiased estimator of the variance of $g(X)$,

$$\hat{\sigma}_g^2 = \frac{1}{N-1}\sum_{i=1}^{N}\left[g(X_i) - (\hat{\mu}_g)\right]^2 = \frac{1}{N-1}\left[\sum_{i=1}^{N} g(X_i)^2 - N\hat{\mu}_g^2\right] .$$

The standard error of $\hat{\sigma}_g^2$ is given approximately by

$$\sigma_{\hat{\sigma}_g^2} \simeq \frac{\sigma_g^2}{\sqrt{N/2}}$$

with equality holding only when $g(X)$ is normally distributed [56]. It follows from the above expressions that the standard error of the estimators of mean and variance of $g(X)$ decrease with the square root of the sample size.

It is often instructive to consider central moments higher than the second one. The ratio of the third central moment to the cube of the standard deviation, called the *skewness coefficient*, provides a measure of asymmetry [7]. Mooney [88] recommends the following expression as an unbiased estimator of skewness coefficient

$$\hat{s} = \frac{\frac{1}{N}\sum_{i=1}^{N}(g(x_i) - \hat{\mu}_g)^3}{\left[\frac{1}{N}\sum_{i=1}^{N}(g(x_i) - \hat{\mu}_g)^2\right]^{3/2}} .$$

Many improvements to the basic Monte Carlo algorithm have been introduced to reduce

the number of evaluations required to achieve a given tolerance level. Among them are importance sampling, stratification, control variates, conditional Monte Carlo, etc. [37, 65, 84, 128]. In the current implementation simple Monte Carlo sampling will be used in all simulations.

One of the attractive features of Monte Carlo simulation is that parallelization of concurrent calculations can be readily implemented in shared memory architectures as well as on heterogeneous machines linked over a network. In the present context each function evaluation consisted of grid generation, flow-field analysis and post-processing steps that were automated and parallelized using shell scripts. All probabilistic simulations reported in this thesis were carried out on a 10-node Beowulf cluster at the Aerospace Computational Design Laboratory, MIT. Each node was equipped with dual 1.8 GHz Xeon processors. Depending on the application (see next section), 2000 MISES trials required on the order of one to three hours of execution time.

3.3 Applications

This section presents results from probabilistic aerodynamic analyzes of three transonic compressor rotor blades subjected to geometric variability. The airfoils and their inlet conditions are representative of typical transonic sections found in core compressors rotors. The first airfoil, denoted IBR, corresponds to the mid-span section of the integrally-bladed rotor discussed in Section 2.1. The second case, denoted DFVLR belongs to a transonic cascade with relative inlet Mach number of 0.82. The last case is the mid-span section of the NASA Stage 37 experimental rotor at relative inlet Mach number of 1.25.

3.3.1 Integrally-bladed rotor, mid-span section

The integrally-bladed rotor is part of the fifth stage of an experimental core compression system. The rotor consists of 56 blades with inlet tip radius of 9.87 inches and hub-to-tip ratio of 0.85.

The axisymmetric viscous flow package MTFLOW was used to perform the initial through-flow calculation for the IBR and R37 cases (Sect. 3.3.3 below). MTFLOW implements a meridional streamline grid discretization of the axisymmetric Euler equations in conservation form. Total enthalpy at discrete flowfield locations and constant mass along each streamtube are prescribed directly. This allows MTFLOW to incorporate localized effects of swirl, entropy (loss) generation and blockage due to rotating or static blade rows without having to solve, in addition, differential continuity and energy equations [25, 85].

The following operating conditions were assumed in the through-flow analysis: mass flow rate of 20 kg/sec, wheel speed of 1200 rad/sec ($U_{\text{tip}} = 301$m/sec) and axial inlet flow (no swirl). In addition the stage inlet static temperature and pressure were taken to be 390 K and 200 kPa resulting in an inlet axial Mach number of 0.43. Figure 3-1(a) shows the pressure coefficient contours computed with MTFLOW for the specified flow conditions. Figure 3-1(b) depicts the approximately mid-span stream path considered in the analysis.

Figure 3-2(a) shows the cross section of the nominal IBR blade along the specified stream path. The inlet relative Mach number and flow angle are 0.90 and 62.64 degrees respectively[2] and the Reynolds number based on inlet tip radius is 3×10^6. Figure 3-2(b)

[2] A correction in inlet flow angle predicted by MTFLOW was needed to minimize passage losses

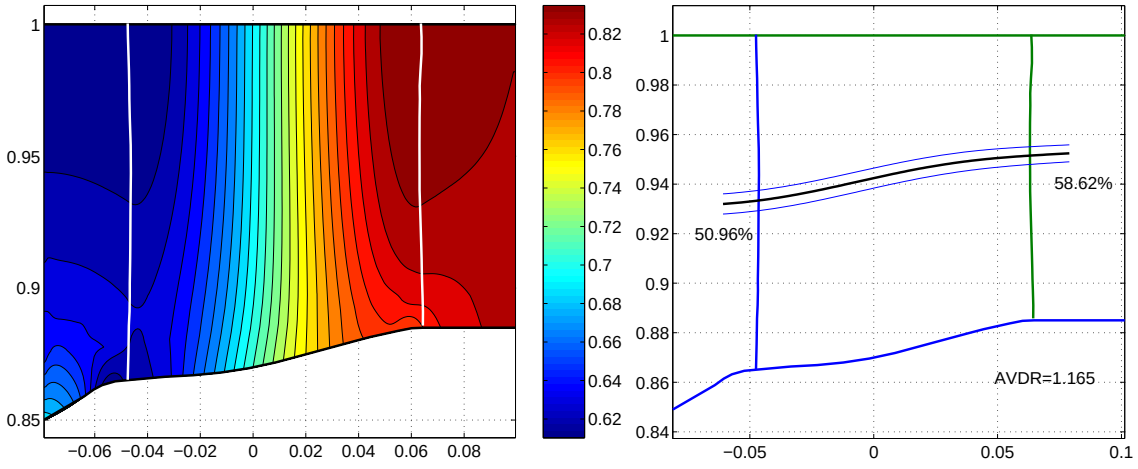

(a) Pressure coefficient

(b) Stream tube

Figure 3-1: IBR through-flow analysis

shows the pressure distribution on the suction and pressure surfaces of the airfoil. After a short pre-compression entry region a shock appears on the suction surface followed by mild compression until about two-thirds of the chord length; from there the flow is further decelerated until the trailing edge is reached. On the concave side an adverse pressure gradient exists until about mid-chord, followed by a plateau. The baseline loss coefficient and turning were computed by MISES to be 0.027 and 14.40° respectively.

The noise model employed in the probabilistic analysis is the PCA-based model described in Chapter 2. The model is given by

$$\tilde{X} = \mathbf{x}^0 + \bar{\mathbf{x}} + \sum_{i=1}^{K} \sqrt{\lambda_i} Z_i \mathbf{v}_i$$

where $\mathbf{x}^0 + \bar{\mathbf{x}}$ is the average geometry, λ_i and $\mathbf{v}_i$ are the i^{th} eigenvalue and corresponding eigenvector of the scatter matrix of measurements, and the Z_i $i = 1, \ldots, K$ are independent, standard normally distributed random variables (i.e., from $\mathcal{N}(0, 1)$). As was discussed in Chapter 2, each measured blade was "cut" along the path shown in Fig. 3-1(b) and the resulting two-dimensional cross section was used in constructing the scatter matrix. For the present calculations all modes were included, i.e., $K = mp$. The effect of varying the cut-off parameter K is explored at the end of this sub-section.

The probabilistic analysis consisted of computing the loss coefficient and turning of blades formed by perturbing the nominal geometry (i.e., instances of $\tilde{X}$) while holding all other input parameters fixed.

The convergence criterion used for the Monte Carlo simulations was

$$\left| \hat{\sigma}_{\varpi}^{N} - \hat{\sigma}_{\varpi}^{N-n} \right| < \varepsilon$$

where the superscripts indicate the number of samples taken. In the present study $\varepsilon = 10^{-5}$ and $n = 10$ were used. Results from numerical experimentation suggested that $N = 2000$

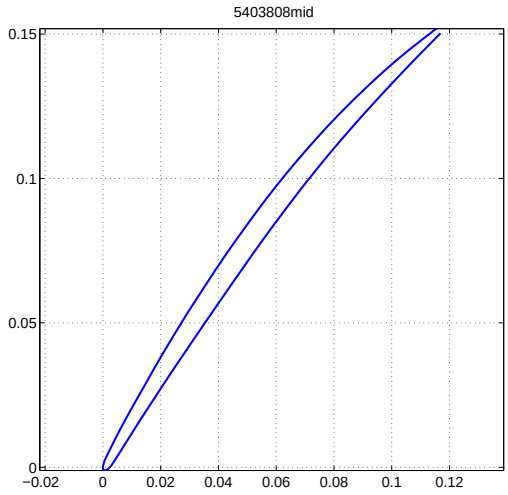

(a) Blade section

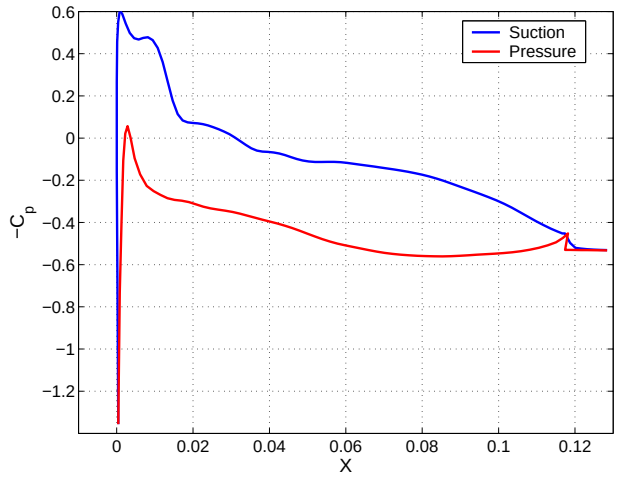

(b) Pressure coefficient

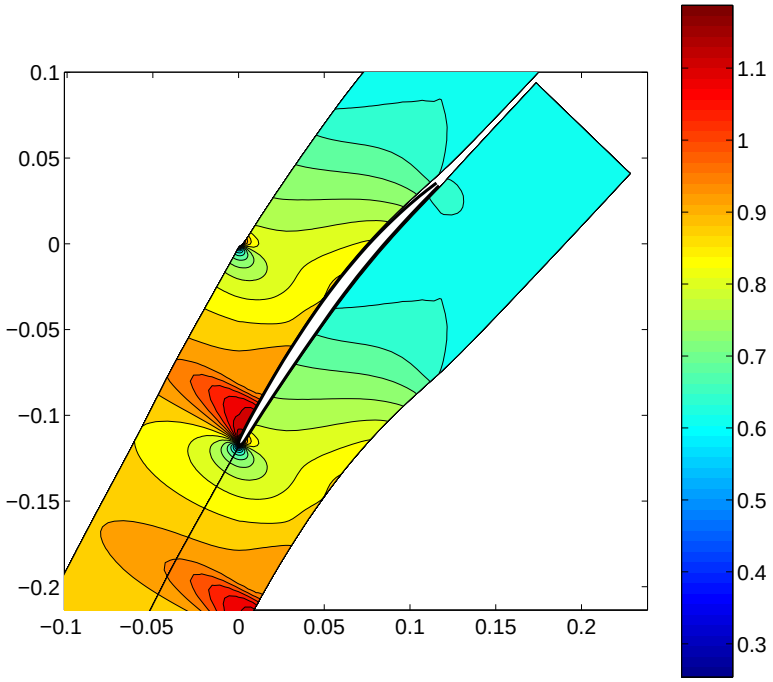

(c) Mach number contours

Figure 3-2: IBR, $M_1 = 0.90$, axial velocity-density ratio (AVDR): 1.27

trials were typically sufficient to achieve the required tolerance for all the cases reported here.

Figure 3-3 shows histograms of loss coefficient and turning. The abscissa represents the values of the output variable, while the ordinate indicates the relative number of trials that fall within each of the equal-length intervals subdividing the abscissa. In the limit of large number of trials, $N \to \infty$, the outline of the histogram bar plot approaches the continuous distribution of the output variable. The two vertical dashed lines indicate the nominal (baseline) and mean values.

The estimated mean loss coefficient is about 4% higher than the baseline (noiseless) value, while the mean turning is about 1% lower than nominal. The estimated variabilities of loss coefficient and turning are small, with a coefficient of variability of about 0.03 and a deviation of less than one-tenth of one degree respectively. The loss coefficient density is less symmetric (with positive skewness coefficient) than that of the turning.

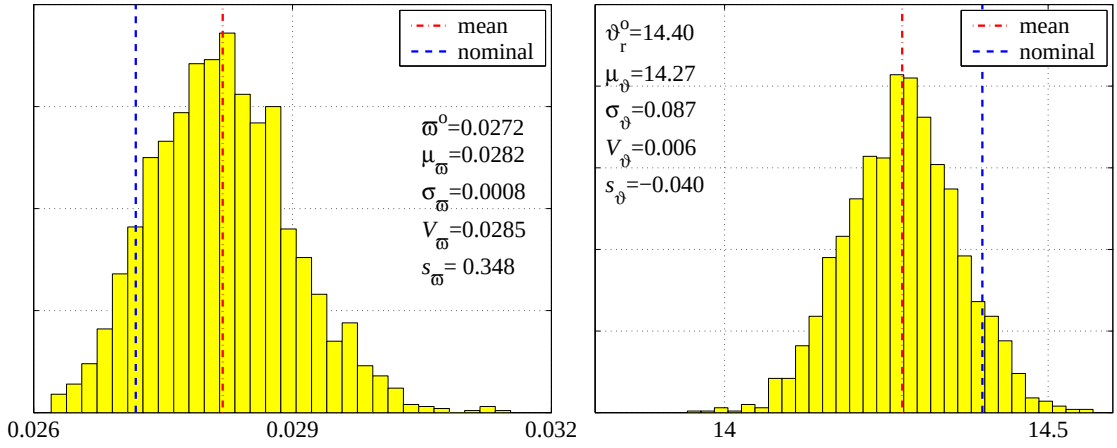

(a) Loss Coefficient

(b) Turning Angle

Figure 3-3: IBR: Impact of geometric variability

The small impact of geometric variability on aerodynamic performance is not surprising given the small geometric variability present in the measurement samples. Production airfoils, manufactured with processes that are less tightly controlled than the current flank-milled IBR case, may be expected to exhibit higher levels of geometric variability. Appendix B illustrates the differences in shape variability between two IBRs manufactured with point and flank milling respectively. As shown in the appendix, an IBR fabricated via the more common point milling process can exhibit a ten-fold or larger increase in geometric variability compared to a flank milled IBR.

To explore the impact of increased manufacturing noise amplitude on the aerodynamic performance statistics, a series of Monte Carlo simulations were performed with various levels of geometric noise. In these the geometric noise model was modified to take the form

$$\tilde{X} = \mathbf{x}^0 + \bar{\mathbf{x}} + \sum_{i=1}^{K} a\sqrt{\lambda_i} Z_i \mathbf{v}_i \ . \tag{3.5}$$

where a is a geometric variability amplitude. Figure 3-4 summarizes the Monte Carlo estimates of mean and standard deviation of the outputs of interest for $a = 1, \ldots, 8$. In

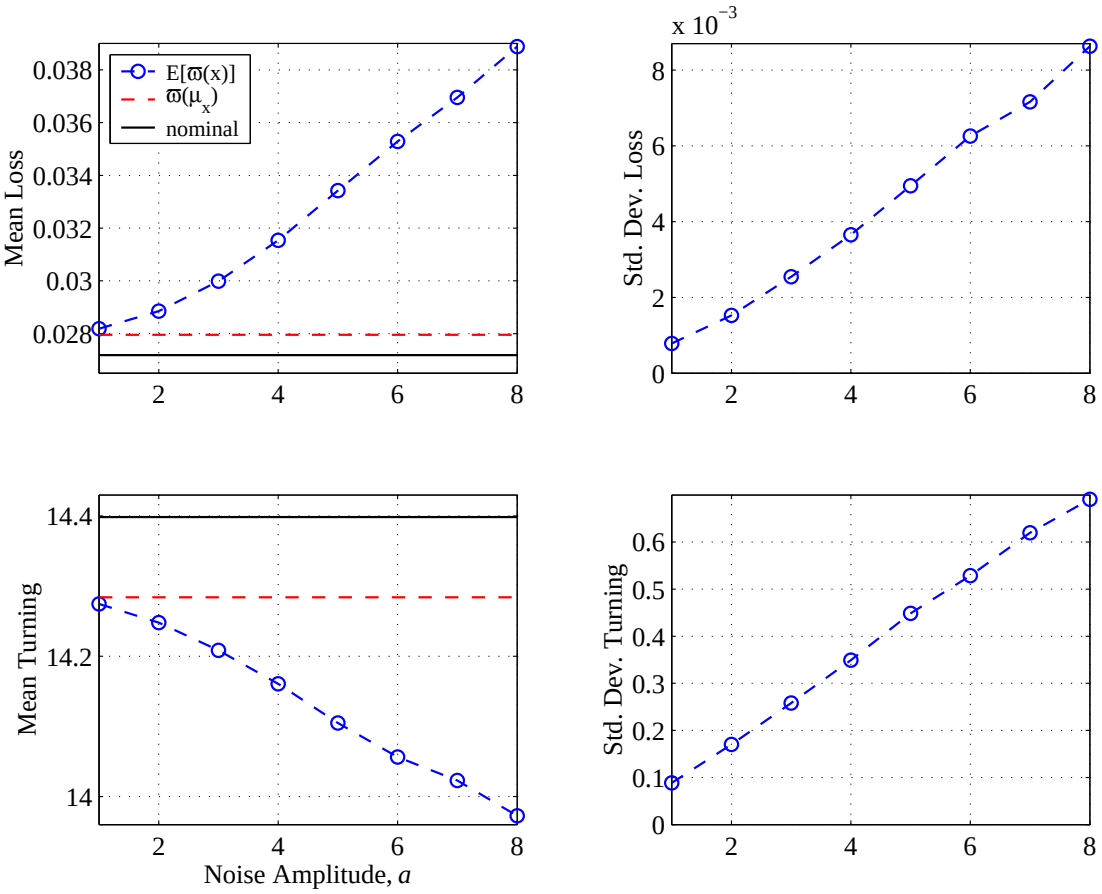

Figure 3-4: IBR: Mean and standard deviation vs. noise amplitude

the figure the horizontal dashed line indicates the loss and turning corresponding to the average geometry, $\mathbf{x}^0 + \bar{\mathbf{x}}$. Similarly the baseline loss and turning are indicated by solid lines. At the original noise level, $a = 1$, the average geometry dominates the difference in loss coefficient and turning from the baseline values, i.e., the geometric variability about the average geometry has little effect on the "mean shift." For a noise amplitude of $a = 2$, the effect of the geometric variability becomes noticeable; in the case of the loss coefficient the noise contributes about half of the total shift. For $a = 4$ the contribution of the average geometry to the turning angle shift from nominal is only half of the total. For $a > 4$ the shift from nominal in both loss and turning is dominated by the variability of the measurements, rather than by the average geometry. One implication of the increase in relative importance of the scatter is that controlling the manufacturing process by "re-centering" the target geometry may not be sufficient to effectively improve the mean performance.

As mentioned above, at the level $a = 1$ the loss coefficient mean-shift is about 4% while the COV is less than 3%. In contrast, at $a = 2$ the loss coefficient mean-shift and COV are 6% and 5% respectively; and at $a = 5$ the corresponding values are 23% and 15%.

Mean loss coefficient and turning depicted in Fig. 3-4 do not appear to vary linearly with geometric noise amplitude in the vicinity of $a = 1$. Rather the amount of curvature

indicates a higher-order dependence. On the other hand, the increase in loss and turning variability—as measured by their estimated standard deviation—increases nearly linearly with geometric noise amplitude, at the approximate rates of $0.001/a$ for loss and $0.1/a$ degrees for turning. This behavior can be explained by considering a quadratic approximation to the loss coefficient; namely

$$\hat{\varpi}(x) = \hat{\varpi}_0 + c_1 x + c_2 x^2 \ ,$$

where x is a noise variable. In particular consider a centered normal variable $X \sim \mathcal{N}(\mu_X, \sigma_X^2)$ with $\mu_X = 0$. Then, letting a stand for noise amplitude,

$$\begin{aligned} \mathbb{E}[\hat{\varpi}(aX)] &= \hat{\varpi}_0 + c_1 a \mathbb{E}[X] + c_2 a^2 \mathbb{E}[X^2] \\ &= \hat{\varpi}_0 + c_2 a^2 \sigma_X^2 \ . \end{aligned}$$

In words, the mean-shift in loss coefficient under the assumed quadratic dependence and centered noise is seen to depend quadratically on the noise amplitude.

The effect of increasing the geometric variability is further illustrated in Figs. 3-5 and 3-6 which show histograms of loss coefficient and turning angle corresponding to noise amplitudes of $a = 2$ and $a = 5$ respectively. In addition to larger mean shift and higher variability for both loss coefficient and turning, the figures show an increase in skewness from 0.5 at $a = 1$ to 0.75 at $a = 2$ and 1.2 at $a = 5$. In other words, values of loss coefficient higher than the average are more widely dispersed than those lower than average. The increase in asymmetry provides further evidence of the nonlinear dependence of viscous loss generation on noise amplitude. In contrast, the turning distribution remained fairly symmetric (low skewness coefficient) for all three cases. Figure 3-7 shows plots of computed cumulative distribution functions (CDF)[3] of loss and turning for values of a ranging from one to eight. The nominal and average-airfoil values are indicated by dashed and dash-dot vertical lines respectively and the arrows indicate the direction of increasing a. Figure 3-7(a) shows how the high-end "tails" of the distributions become thicker as a increases. For $a = 1$ the probability that the loss coefficient will take on values smaller than nominal is only about 15%, while at $a = 8$ that probability has dropped nearly to zero.

As shown in Fig. 3-7(b), the CDFs of turning seem to all cross in the vicinity of the nominal value. To see how this behavior arises consider a quadratic approximation to the turning angle of the form

$$\hat{\vartheta}(x) = \hat{\vartheta}_0 + c_1 x + c_2 x^2 \ .$$

Taking as before $X \sim \mathcal{N}(\mu_X, \sigma_X^2)$ with $\mu_X = 0$, then

$$\begin{aligned} \mathbb{E}[\hat{\vartheta}(aX)] &= \hat{\vartheta}_0 + c_1 a \mathbb{E}[X] + c_2 a^2 \mathbb{E}[X^2] \\ &= \hat{\vartheta}_0 + c_2 a^2 \sigma_X^2 \ . \end{aligned}$$

[3]The distribution function $F : \mathbb{R} \mapsto [0, 1]$ of a random variable X is defined by $F(b) = P\{X \leq b\}$, i.e., the probability that X takes on a value smaller than or equal to b.

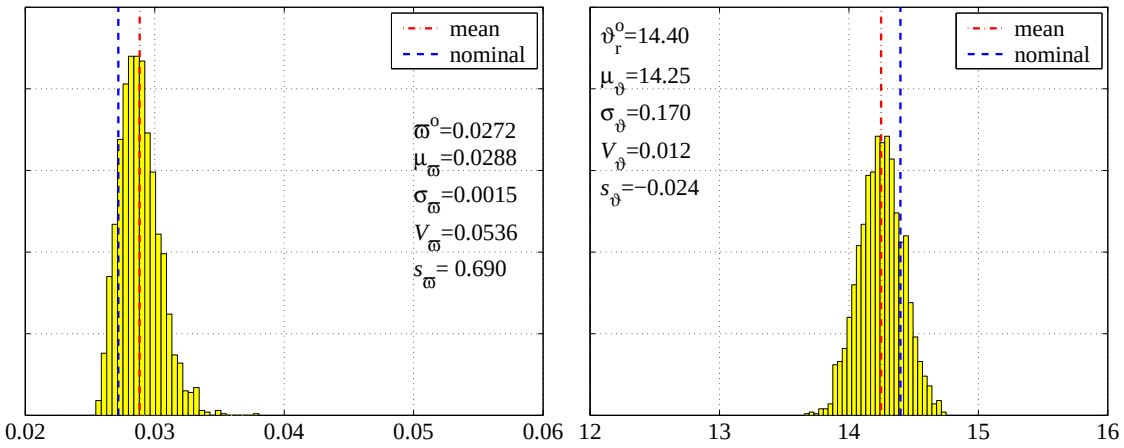

(a) Loss Coefficient (b) Turning Angle

Figure 3-5: IBR: Impact of geometric variability ($a = 2$)

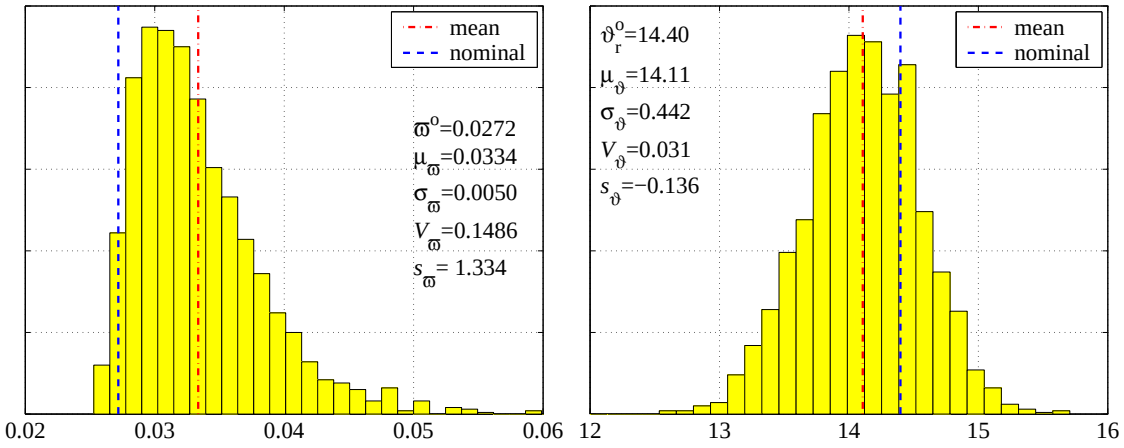

(a) Loss Coefficient (b) Turning Angle

Figure 3-6: IBR: Impact of geometric variability ($a = 5$)

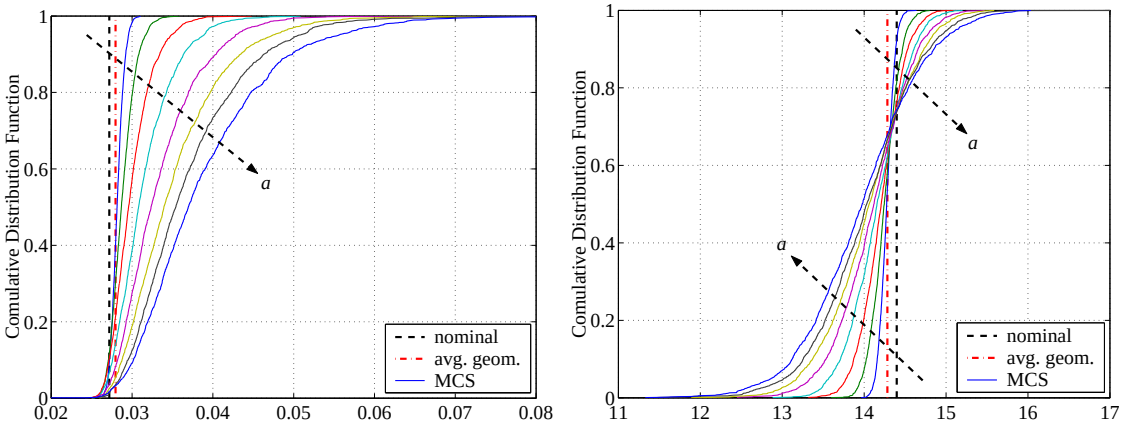

(a) Loss Coefficient

(b) Turning Angle

Figure 3-7: IBR: Impact of geometric variability on distributions of loss and turning, $a = 1, 2, \ldots, 8$

The variance of $\hat{\vartheta}(aX)$ is

$$\begin{aligned}\mathrm{Var}(\hat{\vartheta}(aX)) &= \mathbb{E}\left[\left(\hat{\vartheta}(aX) - \mathbb{E}[\hat{\vartheta}(aX)]\right)^2\right] \\ &= \mathbb{E}\left[\left(c_1 aX + c_2 a^2(X^2 - \sigma_X^2)\right)^2\right]\end{aligned}$$

Using the moment-generating function for normally distributed functions [115], the third and fourth moments of X can be readily found to be $\mathbb{E}[X^3] = 3\mu_X\sigma_X^2 + \mu_X^3 = 0$ and $\mathbb{E}[X^4] = \mu_X^4 + 6\mu_X^2\sigma_X^2 + 3\sigma_X^4 = 3\sigma_X^4$, so that

$$\mathrm{Var}(\hat{\vartheta}(aX)) = c_1^2 a^2 \sigma_X^2 + 2c_2^2 a^4 \sigma_X^4 = c_1^2 a^2 \sigma_X^2 \left(1 + \frac{2c_2^2 a^2 \sigma_X^2}{c_1^2}\right)$$

It follows that when

$$2\left(\frac{c_2 a \sigma_X}{c_1}\right)^2 \ll 1$$

we can expect approximately linear growth of σ_ϑ with noise amplitude a and a mean shift that depends quadratically on a. The trend is illustrated by an example in Fig. 3-8 for $\mathrm{Var}(\hat{\vartheta}_0) = 1$, $c_1 = -1$ and $c_2 = -0.01$ (cf. Fig. 3-4 and 3-7). Because c_2 is small compared to c_1, the contribution of the mean shift is dwarfed by that of the variance in the CDF plot, causing the curves to cross in the vicinity of the mean value, in the manner of Fig 3-7(b).

The impact of geometric variability on boundary layer thickness is illustrated in Figs. 3-9 for noise levels (a) $a = 1$ and (b) $a = 5$. The figures show plots of nominal and mean momentum thickness (θ/c) on the suction and pressure sides (indicated in the plots by SS and PS respectively). The dashed and dot-dashed lines indicate the nominal values—i.e., without geometric noise—while the solid lines indicate the mean values from Monte Carlo simulation. The error bars indicate to a one-standard-deviation interval about at the mean. The discrepancy between nominal and mean momentum thickness values is more

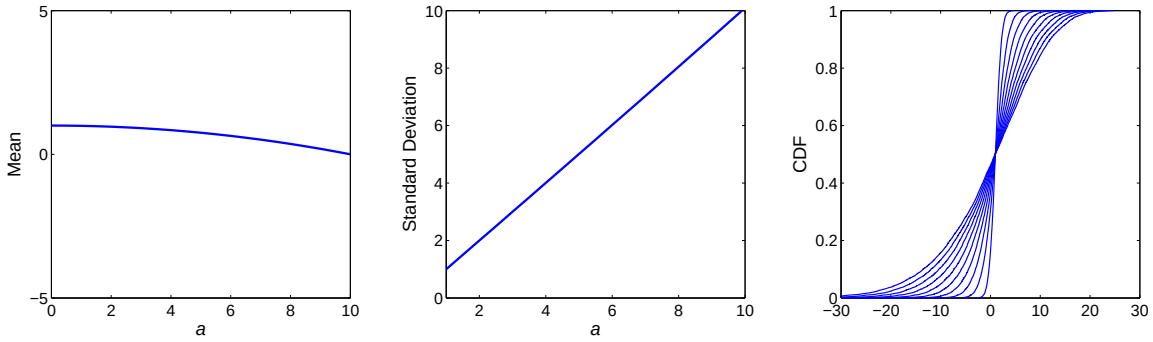

Figure 3-8: Sample mean, standard deviation and CDF of $1 - X - 0.01X^2$

pronounced on the pressure side, as is variability. At the higher noise level the impact on the pressure side momentum thickness variability and mean-shift is more evident.

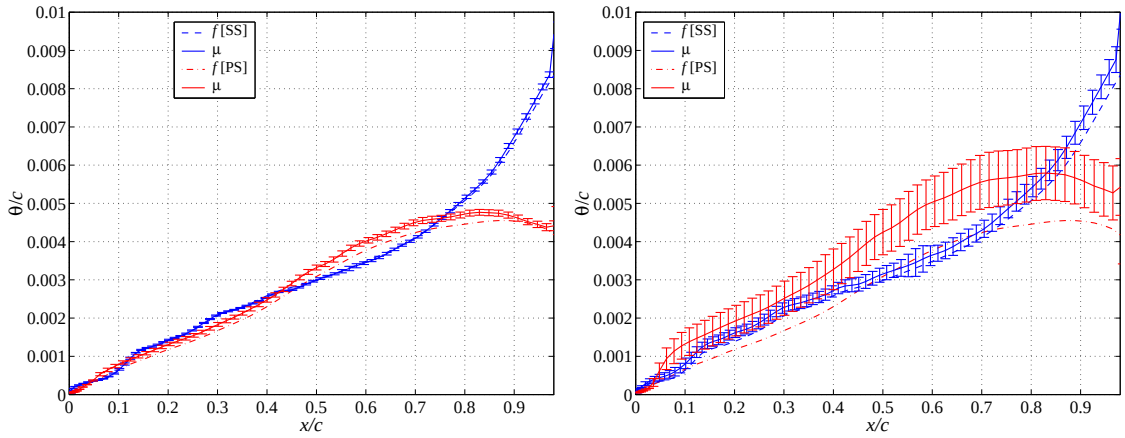

(a) $a = 1$ (b) $a = 5$

Figure 3-9: IBR: Effect of geometric variability on displacement thickness. Mean indicated by solid lines, one-standard deviation interval by error bars. [SS]: suction side, [PS]: pressure side

Figures 3-10 show nominal and statistical plots of shape parameter H (i.e., the ratio of displacement to momentum thicknesses) at noise levels $a = 1$ and 5. H may be thought of as an indicator of boundary layer "health", with values above four indicating possible downstream boundary layer separation [19]. The nominal values of shape parameter are higher near the airfoil nose, reaching four on the pressure side at about $x/c = 0.05$ and then dropping below two for most of the airfoil chord on both sides. The mean-shift and variability of H is more pronounced on the pressure side, especially at $x/c = 0.05$. The effect becomes more evident at that location at the higher variability level (Fig. 3-10(b)).

As discussed by Cumpsty [19] [4], the momentum thickness itself does not necessarily indicates the mechanism by which losses are created. A more appropriate quantity to

[4]Sect. 1.5; see also Denton [23]

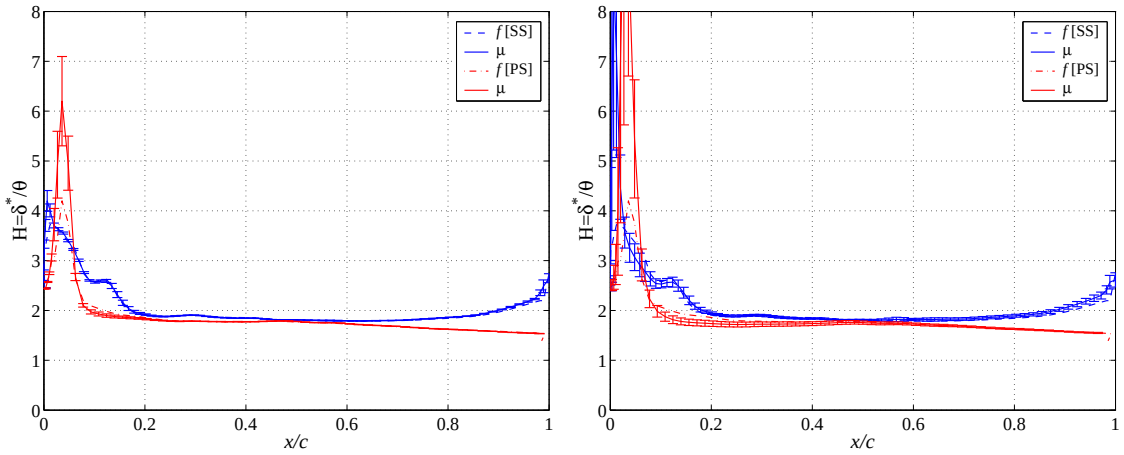

(a) $a = 1$ (b) $a = 5$

Figure 3-10: IBR: Effect of geometric variability on shape parameter $H = \delta^*/\theta$.

consider is the boundary layer dissipation coefficient, defined by

$$C'_d = \int_0^\delta \frac{\tau}{\rho U_e^2} \frac{\partial}{\partial y} \left(\frac{u}{U_e} \right) dy \ , \tag{3.6}$$

where τ stands for shear stress, U_e is the boundary layer edge velocity, ρ stands for density, δ is the boundary layer thickness and u is the component of the flow velocity along the dominant flow direction x (x, and its normal direction y, here stand for boundary layer coordinates).

As shown by Denton [23] the cumulative value of $\rho U_e^3 C'_d$ over the interval $0 \leq x' \leq x$,

$$\int_0^x \rho U_e^3 C'_d dx' \ , \tag{3.7}$$

is a measure of the rate of entropy generation per unit span [5] in the boundary layer. Figures 3-11 show nominal and statistical plots of $\rho U_e^3 C'_d$ at noise levels $a = 1, 5$. The highest nominal and mean values occur on the airfoil nose on the pressure side and at about 10% chord on the suction side. Local mean dissipation values are higher on the suction side of the airfoil but the variability is larger on the pressure side.

Figures 3-12 show cumulative values of $\rho U_e^3 C'_d$ as per Eq. (3.7). The rate of entropy generation is about three times higher on the suction side than on the pressure side. The nominal-to-mean shift is more pronounced on the pressure side, as is the variability. The final entropy generation rate uncertainty and mean shift are more evident at the $a = 5$ noise level.

Although using Monte Carlo simulation—with its weak dependence on number of input variables—rests importance from consideration of reduced order models of geometric variability, additional information that can be obtained from considering groups of modes

[5] Assuming that the process takes place at some fixed reference temperature T_{ref}

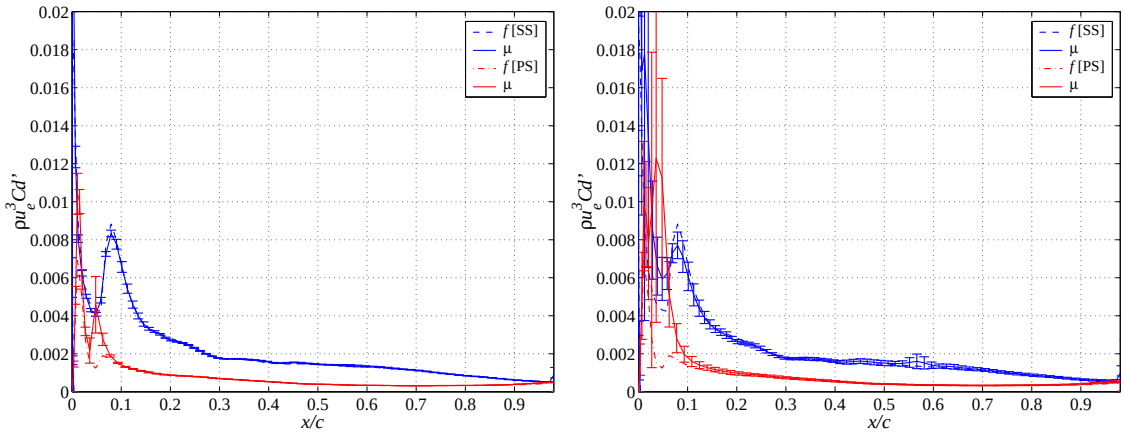

(a) $a = 1$ (b) $a = 5$

Figure 3-11: IBR: Effect of geometric variability on boundary layer dissipation coefficient

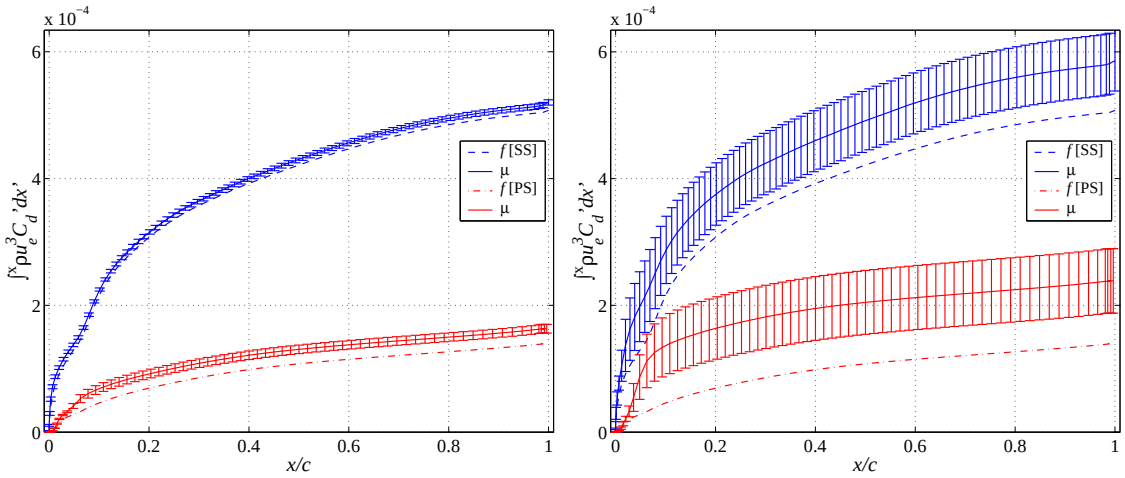

(a) $a = 1$ (b) $a = 5$

Figure 3-12: IBR: Effect of geometric variability on boundary layer entropy generation as per Eq. (3.7). Mean indicated by solid lines, one-standard deviation interval by error bars. [SS]: suction side, [PS]: pressure side

separately. Figure 3-13 presents statistics of loss and turning according to the number of PCA modes used in the geometric noise model (denoted K in Eq. 3.5) for noise amplitude $a = 5$. For each value of K, a Monte Carlo simulation with $N = 5000$ trials was performed. Baseline and average-geometry values are denoted by constant dashed lines, while the values corresponding to $K = mp$ (all modes) are shown by a solid line. The average-geometry contribution to mean loss constitutes a relatively small fraction of the total shift from nominal, as pointed out earlier. The scatter due to the first six modes is responsible for about 90% of the total loss coefficient mean shift. Similarly, the first six modes taken together produce close to 90% of the turning mean-shift obtained when all modes are considered. The first six modes are also the most influential on loss coefficient variability, as indicated by its standard deviation plot. The first two modes clearly dominate turning angle variability. Table 3.1 shows percent differences between statistics reduced-order and full model simulations for noise level $a = 5$. Using only the first PCA mode, mean loss is under-predicted by 15% and the error in standard deviation of loss and turning is 56 and 71% respectively. It takes 15 modes to reduce the error in standard deviation of loss coefficient to 7%. Beyond $K = 15$ comparisons stop being meaningful due to lack of resolution in Monte Carlo simulation.

3.3.2 DFVLR transonic cascade

The second application considered in this chapter corresponds to the 45%-span section of a compressor blade row with design pressure ratio of 1.51 and tip Mach number of 1.38 [119], denoted here as DFVLR. Quasi-2D analysis of the DFVLR case using MISES for Mach numbers ranging from 0.82 to 1.1 and axial velocity-density ratios (AVDR) between 1 and 1.184 were conducted and reported by Youngren [141]. For the probabilistic analysis of this airfoil, inlet Mach number $M_1 = 0.82$, inlet flow angle $\beta_1 = 55.95°$, AVDR = 1 and constant stream-tube radius (2-D cascade) were taken as the baseline conditions.

Figure 3-14(a) shows the DFVLR airfoil cross section (stagger angle $\xi = 48.5°$). Figures 3-14(b) shows the pressure distribution on the surfaces of the airfoil, while 3-14(c) depicts the Mach number contours in the flow passage. The loss coefficient and turning computed by MISES for the specified baseline conditions are $\varpi^0 = 0.0297$ and $\vartheta^0 = 9.26°$ respectively.

Three geometric noise modes and Mach number variability are considered. The former group is comprised of thickness, twist and leading-edge bluntness modes. The selection of these geometric noise modes was based primarily on two arguments. First, the statistical analysis of existing hardware reported in Chapter 2 suggested that these modes are strong contributors to shape variability. Secondly, these modes are known to directly impact transonic and supersonic airfoil aerodynamics, as discussed in Section 2.4.

Twist, thickness and Mach number are modeled as normally distributed, independent random variables, $X_{\text{tw}}, X_{\text{th}}, X_M$. The parameters used to define their distributions in the present application, namely mean and standard deviation, are summarized in Table 3.2. The thickness variable is scaled with respect to the nominal chord length. Twist is given in units of degrees.

Detailed information about geometric variability in compressor airfoils, particularly twist and thickness, is not readily available in the open literature. Thus the values summarized in Table 3.2 were obtained by scaling the amplitude and mode shape results from the two-dimensional PCA study reported in Chapter 2 to the DFVLR section. Figure 3-15 shows histograms of exit Mach number from probabilistic simulations of the IBR case

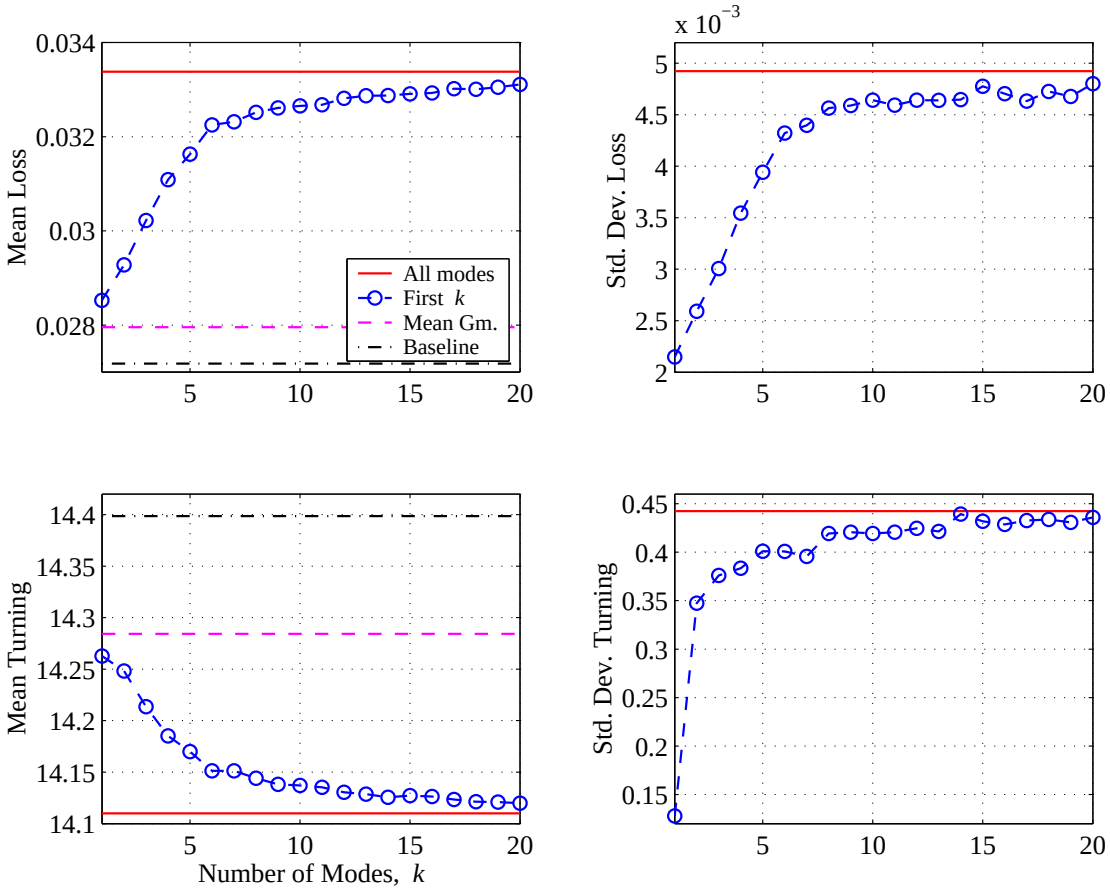

Figure 3-13: IBR mid section: Statistics versus number of PCA modes, $a = 5$

Table 3.1: Percent difference in statistics from reduced-order model (with K modes) and full model ($K = mp$) simulations, $a = 5$

K	μ_{ϖ}	σ_{ϖ}	μ_{ϑ}	σ_{ϑ}
1	-14.5	-56.4	1.08	-71.1
5	-5.2	-20.0	0.43	-9.3
10	-2.2	-5.7	0.19	-5.2
15	-1.4	-3.0	0.12	-2.4
20	-0.8	-2.5	0.07	-1.4

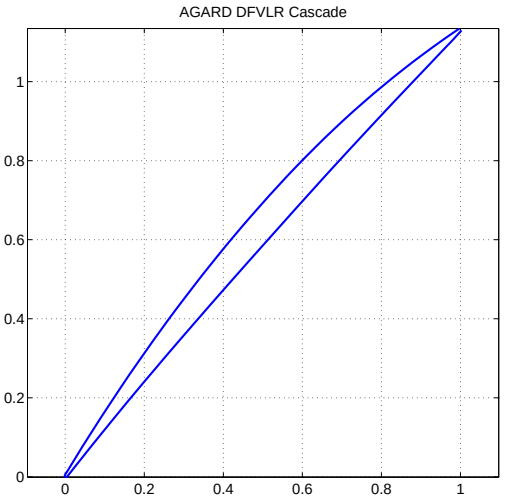

(a) Blade section

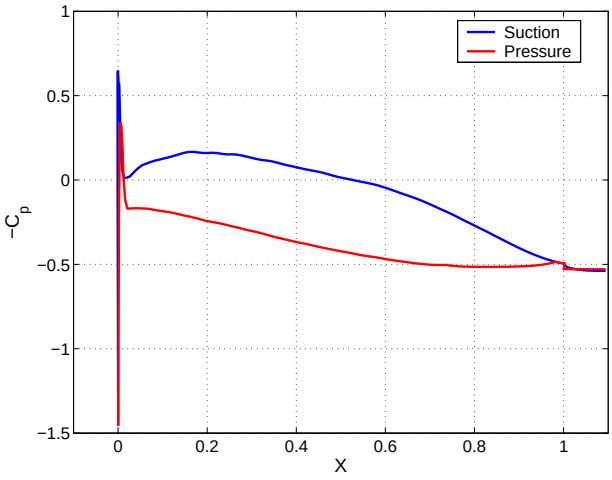

(b) Pressure coefficient

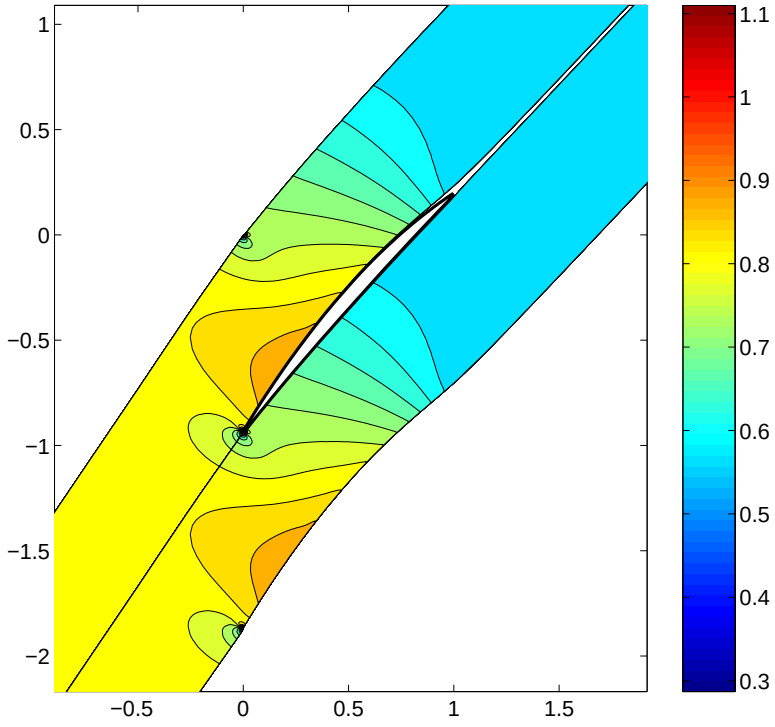

(c) Mach number contours

Figure 3-14: DFVLR cascade, $M_1 = 0.82$, AVDR=1

Table 3.2: DFVLR random input statistics

Mode	Mean	Std. Dev.
Thickness (c.l.)	0	0.002
Twist (deg)	0	1
Mach Number	0.82	0.01

discussed previously. The standard deviations for the $a = 1$ and $a = 5$ noise amplitude cases suggest a reasonable range of inlet Mach number variability to explore would be $0.003 \leq \sigma_M \leq 0.011$. In the DFVLR and R37 cases the higher level of inlet Mach number variability, $\sigma_M = 0.01$ was used.

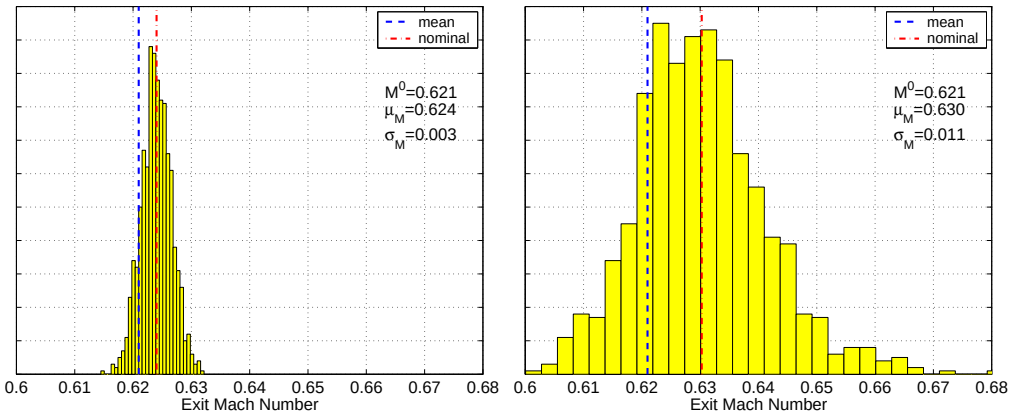

(a) $a = 1$ (b) $a = 5$

Figure 3-15: IBR exit Mach number variability

The leading-edge shape variability was introduced to account for both manufacturing imperfections and wear; it is modeled here via the bluntness mode described in Section 2.4. Figure 3-16(a) illustrates the impact of increasing the leading-edge bluntness of the DFVLR airfoil while keeping other geometric and flow conditions fixed. Figure 3-16(b) shows the modified leading-edge shapes for various values of bluntness parameter values. The degradation in performance is shown in the figure as an increase in loss coefficient and a decrease in turning. When the bluntness parameter has been increased to three, the loss coefficient has gone up by approximately 8% while the turning has decreased by about 1.5%. At an increase in b of 3 the increase in loss is about 17% while the turning has decreased by about 2.8%. The larger relative impact on the loss coefficient is to be expected since the loss generation for this low-Mach-number transonic case is primarily due to viscous effects, and the leading edge shape will directly impact the boundary layer transition and growth. The effect of leading-edge bluntness can be expected to be more pronounced for higher Mach number cases, as the loss due to leading-edge thickness has been shown to scale with M^2_{inlet} [71].

Figure 3-17 shows histograms of loss coefficient and turning angle resulting from the

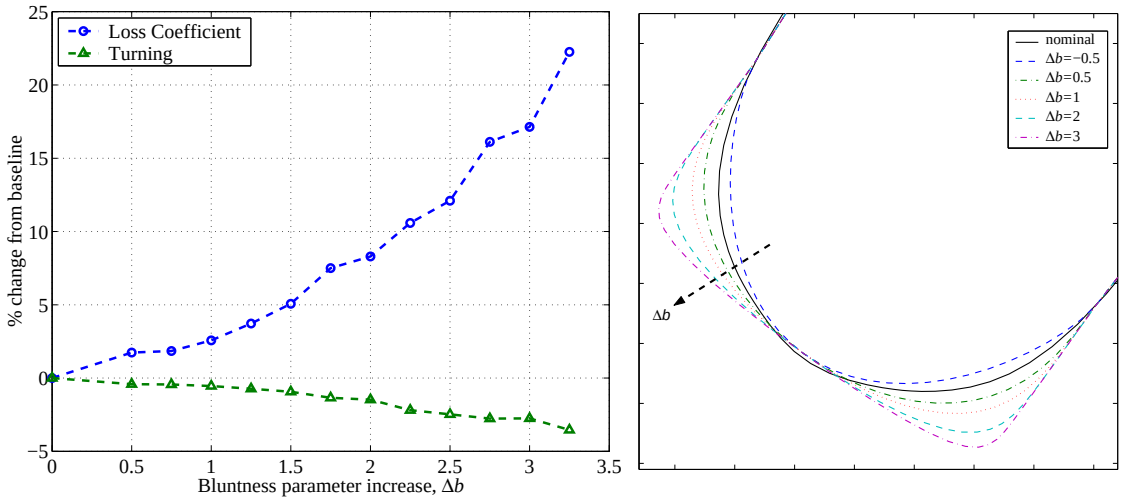

(a) (b)

Figure 3-16: Aerodynamic performance trends with increased leading-edge bluntness

Monte Carlo simulation. The results indicate that the expected value of loss coefficient in the presence of the prescribed geometric and inlet flow condition variability is about 0.032, an increase of 6% from the baseline value. The predicted standard deviation is about 0.002, which corresponds to a variability of 6% as represented by the coefficient of variability V_{ϖ}. The skewness coefficient is about 1.8, indicating that $\varpi(X)$ is noticeably asymmetric, with values higher than the average being more dispersed than those smaller and not normally distributed. The skewness of $\varpi(X)$ indicates that geometric or inlet condition perturbations are more likely to cause a deterioration, rather than an improvement, in the aerodynamic performance of the blade passage. This behavior is typical of airfoils that have been optimized for particular operating conditions or without consideration to noisy geometry or inputs.

In contrast to the loss coefficient statistics, the mean turning angle differs little from the baseline value (less than 0.2% change) but the coefficient of variability is higher than that of the loss, at about 0.1. The turning distribution is more symmetric than the loss coefficient distribution, as indicated by its smaller skewness coefficient.

Figure 3-18(a)–(d) show nominal, mean and standard deviation values of momentum thickness, shape parameter, dissipation and boundary layer entropy generation rate. The nominal and mean momentum thickness have similar values until 70% chord after which the suction side thickness grows faster to become twice as large as the pressure side thickness at the trailing edge. The mean-shifts are not as pronounced as in the IBR case (cf Fig. 3-9). The nominal shape parameter is highest in the immediate vicinity of the airfoil nose. H is below two until 80% chord, after which it grows to three on the suction side. Boundary layer dissipation, as indicated by $\rho U_e^3 C_d'$ is highest and most variable in the vicinity of the leading edge. Nominal and mean local dissipation values are higher on the suction side and are also more variable on the aft 70% chord. The total nominal entropy generation rate is about 2.5 times higher on the suction side. The final mean-shift and standard deviation are

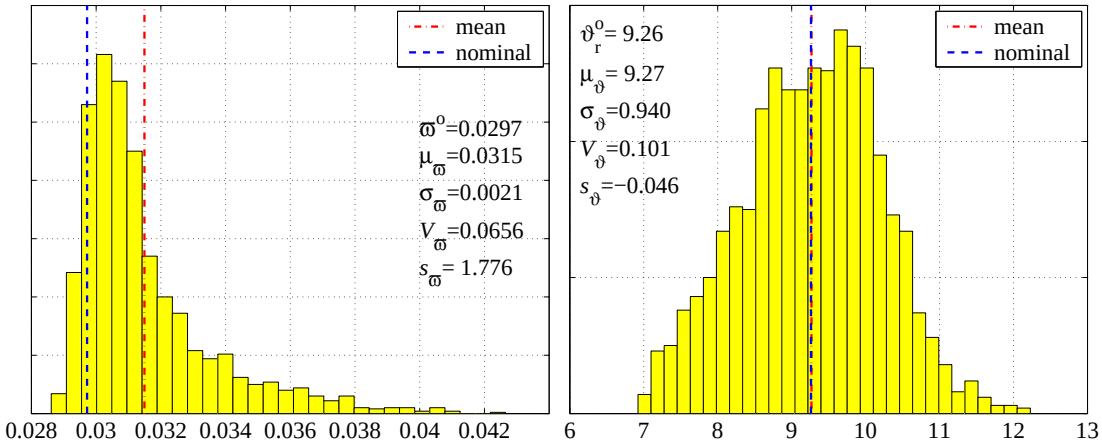

(a) Loss coefficient

(b) Turning angle

Figure 3-17: DFVLR: Histograms of loss coefficient and turning angle

twice and five times larger on the pressure side than on the suction side, respectively.

3.3.3 NASA rotor 37, mid-span section

NASA rotor 37 (R37) is an experimental compressor rotor designed at NASA Glenn Research Center. This has been used for experimental and numerical studies of turbomachinery phenomena such as endwall blockage development [122] and tip clearance effects [17, 121]. The rotor consists of 36 blades having inlet hub-to-tip diameter ratio of 0.7 and aspect ratios of 1.19 with an inlet tip radius of 0.252 m. The design hub and tip relative inlet Mach numbers are 1.13 and 1.48 respectively. The design tip speed is 454 m/sec at a wheel speed of 1800 rad/sec. The choking mass flow rate, $\dot{m}_{\text{ch}}$ is 20.9 ($\pm$0.14) kg/sec [30, 120].

An axial Mach number of 0.43—corresponding to a mass flow rate of of $0.95\dot{m}_{\text{ch}}$ at standard temperature and pressure—was assumed at the inlet of the test region. Exit swirl conditions were imposed according to experimental measurement data provided by Strazisar [120]. A radial maximum-blade-thickness distribution was used to impose the inviscid area blockage. Figure 3-19a shows the flow path, axial blade projection and pressure coefficient contours computed with MTFLOW.

Figure 3-19(b) shows the streamtube path selected for blade passage analysis, which corresponds roughly to the mid-span radial station. Inlet relative Mach number ($M_1 = 1.25$), inlet flow angle ($\beta_1 = 66.21$)[6] and back pressure ($P_2/P_{T_1} = 0.65$) calculated with MTFLOW for this streamtube, as well as the axial variation of streamtube radius and thickness were used as inputs for the baseline blade-to-blade passage analysis. The area velocity-density ratio computed by MTFLOW for this streamtube was 1.452 and the corresponding Reynolds number based on inlet tip radius was 2.33×10^6. Nominal total pressure loss coefficient and turning were computed by MISES to be $\varpi^0 = 0.084$ and $\vartheta^0 = 14.7°$ respectively.

Figure 3-20(a) shows the cross section of the R37 blade along the selected stream path. Figure 3-20(b) depicts pressure distributions on the airfoil suction and pressure sides. The

[6]Some adjustment in M_1 was required to reduce the passage total pressure loss.

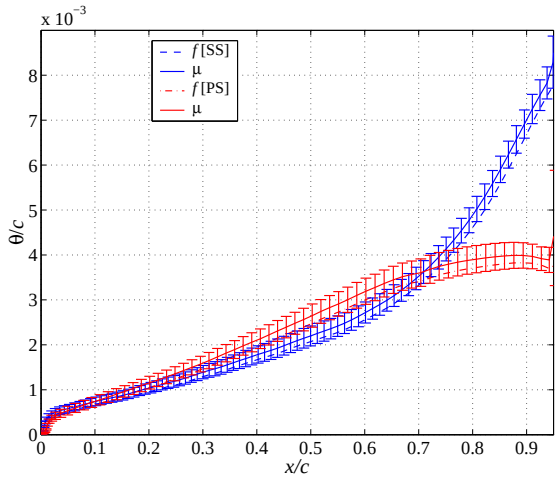

(a) Displacement thickness θ/c

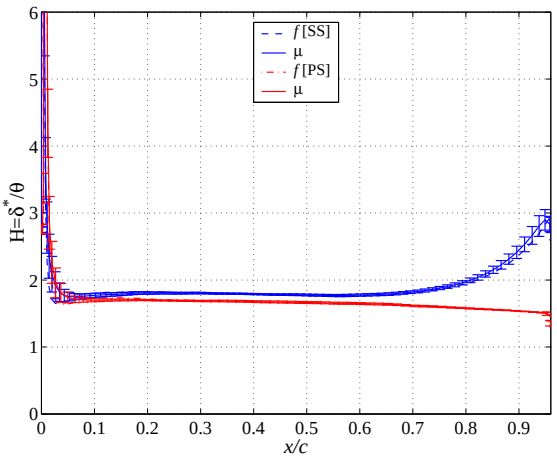

(b) Shape parameter $H = \delta^*/\theta$

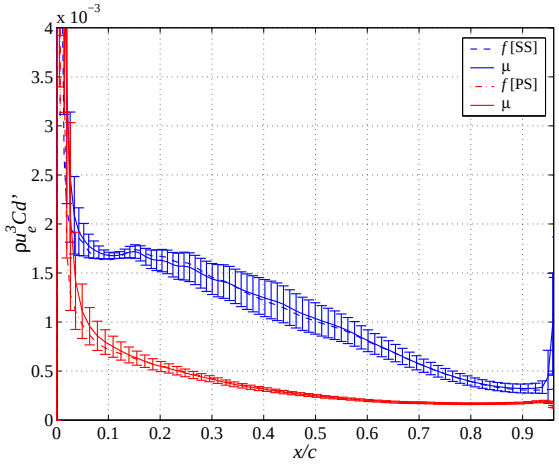

(c) $\rho U_e^3 C_d'$

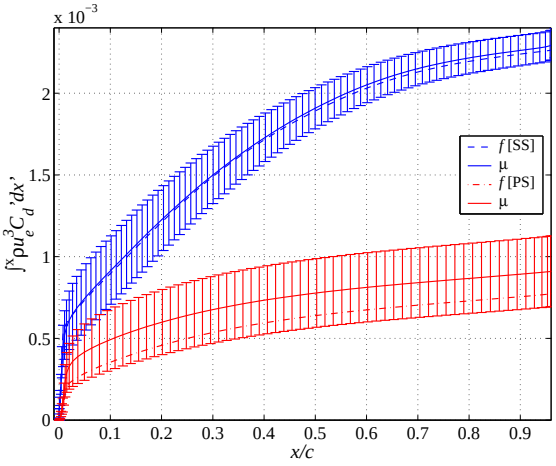

(d) $\int_0^x \rho U_e^3 C_d' dx'$

Figure 3-18: DFVLR: Effect of geometric variability on airfoil boundary layers

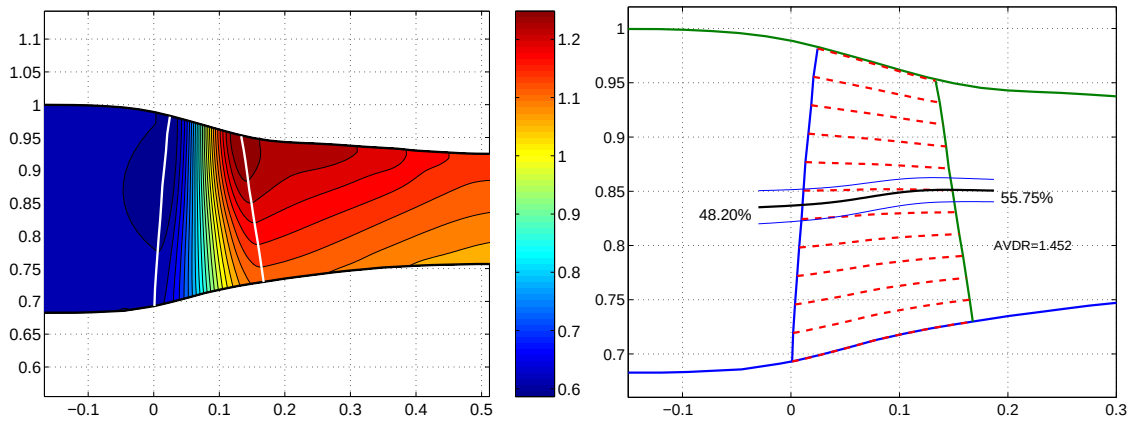

(a) Pressure coefficient

(b) Stream tube

Figure 3-19: NASA rotor 37 through-flow results

suction-side pressure distribution is characterized by a shock near the mid-chord location. Downstream of the shock there is further compression. On the concave side, the pressure is relatively constant. Near the blunt trailing edge the flow is accelerated again. The acceleration at the entry region, between the leading edge and the passage throat on the pressure side, is due to a slight mismatch in the inlet flow conditions caused perhaps by not including end-wall blockage. Figure 3-20(c) shows Mach number contours. At the given operating condition point the bow and passage shocks have coalesced and the impingement point on the suction surface is just upstream of the passage throat.

Table 3.3: NASA Rotor 37 random input statistics

Mode	Mean	Std. Dev.
Thickness (c.l.)	0	0.001
Twist (deg)	0	1
Mach Number	1.25	0.01

As with DFVLR airfoil, three geometric noise modes and Mach number variability are considered in the probabilistic analysis. The geometric noise modes are again thickness, twist and leading-edge bluntness. The input noise statistics were obtained by scaling the amplitude and mode shape results from the two-dimensional PCA study of the IBR blade reported in Chapter 2. The statistics of the normal modes, namely thickness, twist and Mach number, are summarized in Table 3.3. Thickness is scaled with respect to the nominal chord length and twist is given in degrees. For the leading-edge bluntness mode a Beta distribution in the interval $[0.8, 2.0]$ with parameters $\alpha = 2$, $\beta = 4$ was assumed (see Fig. 2-9).

Figure 3-21 shows histograms of loss coefficient and turning angle which are different to those of the IBR and DFVLR cases. The shift in mean loss coefficient from the baseline value is only 2%, while the coefficient of variability is roughly 11%. The increase in loss

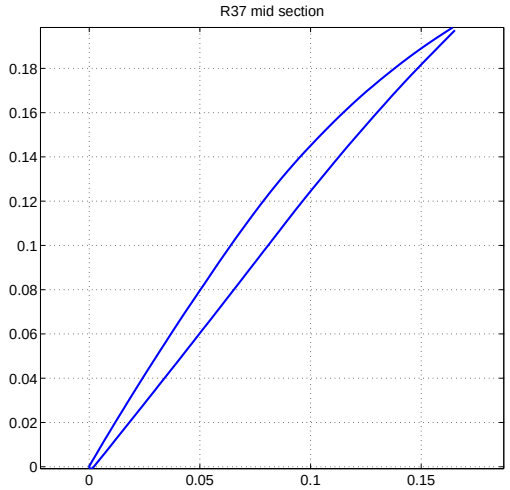

(a) Blade section

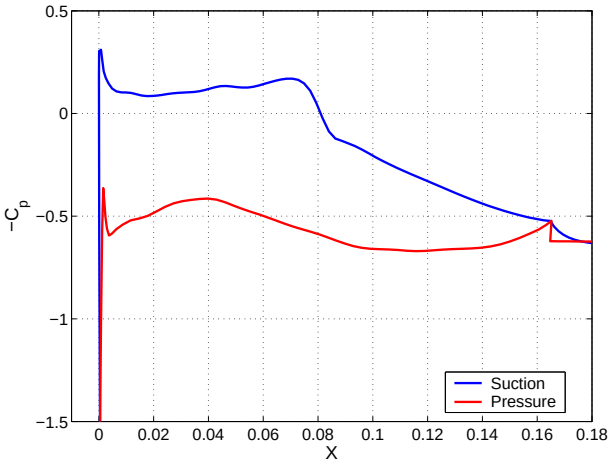

(b) Pressure coefficient

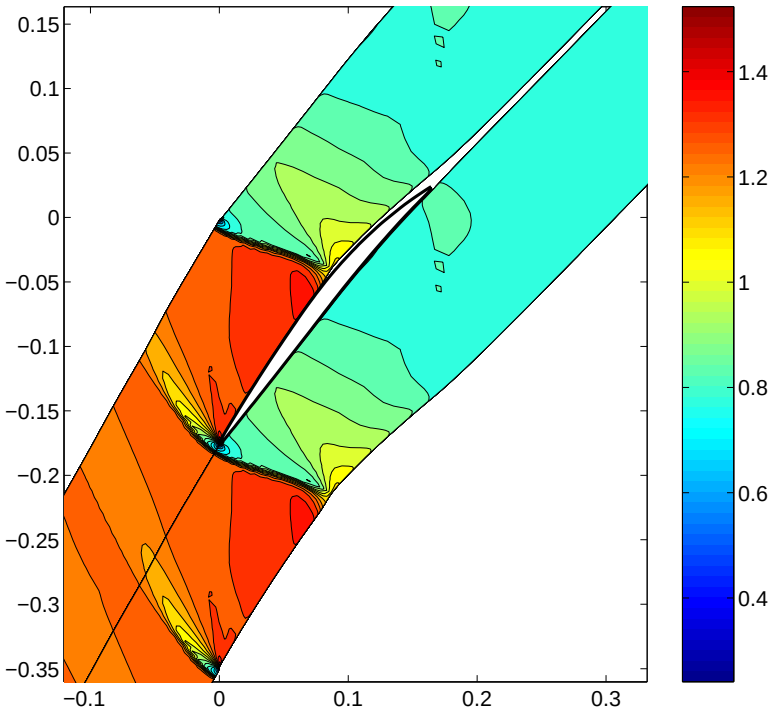

(c) Mach number contours

Figure 3-20: NASA rotor 37, $M_1 = 1.25$, AVDR=1.452

variability can be expected given the higher inlet Mach number of the present case. The skewness coefficient is about 0.3, in agreement with a discernible amount of asymmetry in the loss distribution. The shift in mean turning is negligible, but not so the variability:

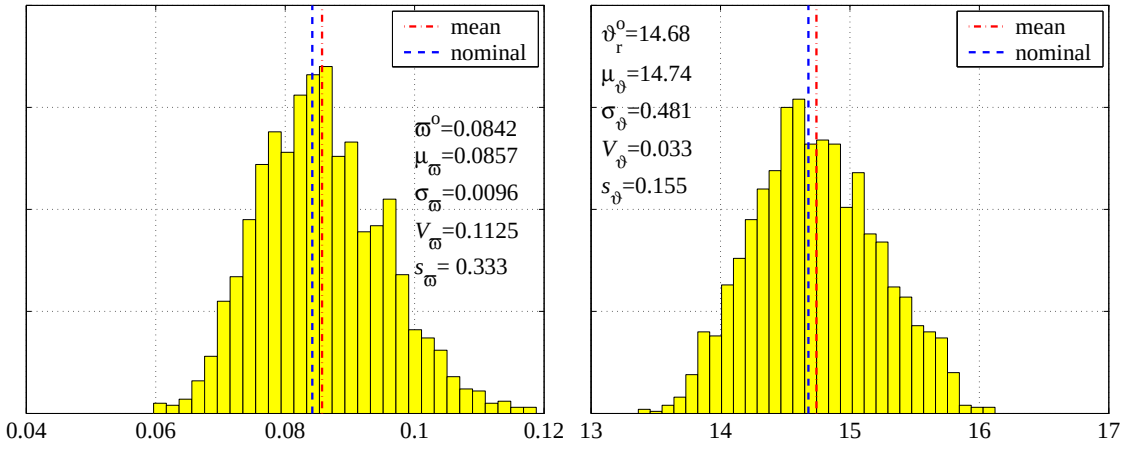

(a) Loss coefficient

(b) Turning angle

Figure 3-21: NASA rotor 37 mid section: histograms

its six-sigma interval spans nearly 3 degrees. As will be discussed in Chapter 6, this small amount of variability in turning angle can have a strong impact on overall compressor performance, especially on pressure ratio.

Figures 3-22 shows plots of momentum thickness, shape parameter, dissipation and boundary layer entropy generation rate. At the trailing edge, the nominal and mean momentum thicknesses are three times larger on the suction side than on the pressure side. The momentum thickness variability is also larger on the suction side, especially on the aft 50% chord. Nominal and mean shape parameter values are highest in the vicinity of the airfoil nose and at mid chord on the suction side. The high mean and variability of mid-chord shape parameter values occur where the passage shock impinges on the suction surface, indicating that the shock interacts with the turbulent boundary layer causing it to separate.

Boundary layer dissipation, as shown in Figs. 3-22(c), is higher and more variable on the suction side than on the pressure side, particularly behind the shock impingement location. The total mean entropy generation rate on the suction side is about six times that of the pressure side, and at least three times more variable. The suction side entropy generation rate variability becomes more pronounced on the aft 40% of the airfoil, behind the shock impingement location.

3.4 Summary

In this Chapter, the impact of geometric and inlet flow condition variability on aerodynamic performance of three compressor blade passages was assessed. The probabilistic analysis consisted of Monte Carlo simulations using the quasi-2D cascade analysis code MISES. Geometric noise models were based on the PCA results of Chapter 2. The IBR test case,

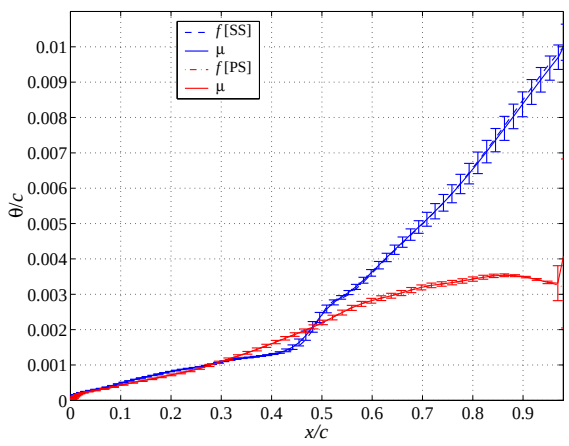

(a) Displacement thickness θ/c

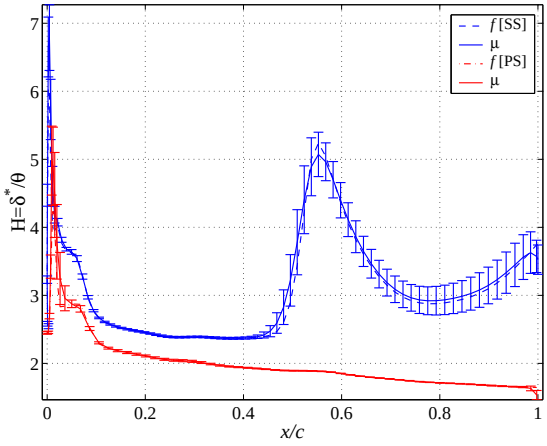

(b) Shape parameter $H = \delta^*/\theta$

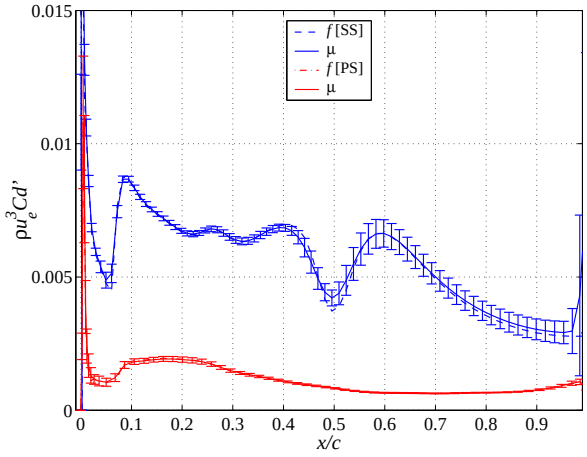

(c) $\rho U_e^3 C_d'$

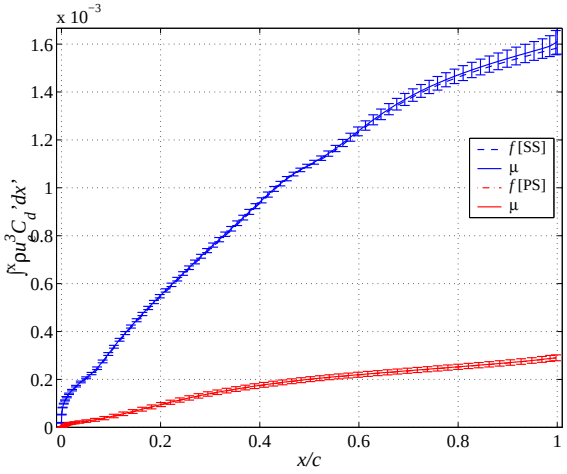

(d) $\int_0^x \rho U_e^3 C_d' dx'$

Figure 3-22: R37: Effect of geometric variability on airfoil boundary layers

discussed previously in Chapter 2, corresponds to an integrally-bladed rotor passage with inlet Mach number of 0.9. At the original noise level found in the PCA analysis of surface measurements, the loss coefficient mean-shift was found to be about 4% while the COV is less than 3%. At double of baseline geometric noise amplitude, the loss coefficient mean-shift and COV are 6% and 5% respectively. At a more realistic $a = 5$ geometric variability level the loss COV 15% and the mean loss is 23% higher than nominal. The amplitude of the geometric noise variability had a linear effect on the increase of output variability. As the noise variability was increased, the relative contribution of the average geometry to mean shift decreased. The loss coefficient distribution became less symmetric as the noise leveled increased.

The DFVLR test case, a two-dimensional cascade with inlet Mach number of 0.82, exhibited loss coefficient mean-shift and COV of 6% when subjected to leading-edge bluntness, inlet Mach number, thickness and twist variability. In contrast, the mean turning differed by less than 0.2% from the baseline value (less than 0.2% change) but its coefficient of variability is about 10%. The R37 case, corresponding to the mid-span section of the NASA rotor 37 experimental rotor, showed a loss coefficient mean shift of 2%, while its coefficient of variability was more than 10%. The shift in mean turning was negligible but the six-sigma interval spanned nearly 3 degrees.

Chapter 4

Probabilistic Optimization of Compressor Blade Sections

The previous chapters showed that variability in shape and operating condition degrade actual compressor performance. In this Chapter a probabilistic gradient-based approach to compressor blade optimization is outlined. Probabilistic objectives, constraints and corresponding gradients are approximated using Monte Carlo simulation. The probabilistic simulations are driven externally by nonlinear optimization software. The design modes included orthogonal surface modes and blade stagger.

Three airfoils introduced in previous Chapters are optimized both deterministically and probabilistically and then subjected to simulated geometric variability to assess its impact on their performance. Two of the airfoils optimized deterministically for minimum loss coefficient, without geometric or inlet flow variability considerations, exhibited lower expected performance and increased variability than those designed probabilistically. Reductions in mean loss coefficient of 25% and in loss variability of 65% were observed.

Different mechanisms for loss variability reduction are noticed between subsonic inlet flows, in which viscous dissipation in the boundary layers dominates the generation of entropy, and supersonic flows, in which shock losses are prevalent. In the two subsonic inlet cases considered, a small thickness increase on the pressure side near the leading edge caused to a reduction in the rate of flow deceleration and had a positive effect in reducing entropy generation variability. In the supersonic inlet case, a decrease in the flow deceleration rate downstream of the shock impingement location on the suction side helped reduce the loss variability caused by shock-boundary layer interaction.

4.1 Gradient-Based Probabilistic Optimization

Turbomachinery airfoils are typically designed for optimal aerodynamic performance at some nominal operating point such as cruise. Single-point optimization is known to produce airfoils that may perform poorly off-design [62]. This phenomenon is of particular concern when optimizing transonic airfoils and when the number of geometric design parameters is high [26], which is commonly the case in turbomachinery applications. An alternative to single-point optimization is to generalize the objective function under consideration to a weighted sum involving multiple operating points [34]. This approach has the drawback, however, that the best relative weights that appear in the generalized objective function are

not generally known in advance. Also, it has been observed that multi-point optimization may lead to undesirable localized features such as surface waviness or exceedingly thin sections [26].

As mentioned above, traditional probabilistic optimization techniques tend to suffer from either prohibitive computational requirements or from excessive dependence on heuristics. In this section a gradient-based probabilistic optimization method for compressor airfoil shape optimization is outlined. The major advantage of present method is that sensitivity information can be used to accelerate the design space exploration, as well as to provide a sensible stopping criterion.

In the presence of variability—geometric or otherwise—the design goals themselves change. For instance, while a deterministic objective may be to minimize the total pressure loss provided turning is preserved, in the presence of variability a more meaningful goal would be to minimize the *expected* or *mean* passage loss subject to mean turning constraints. Symbolically,

$$\begin{aligned} \mu^*_{\varpi} &= \min_{\mathbf{x}\in\Omega} \mathop{\mathbb{E}}_{\theta} [\varpi(\mathbf{x},\theta)] \\ \text{such that} \quad & \vartheta_l \leq \mathop{\mathbb{E}}_{\theta} [\vartheta(\mathbf{x},\theta)] \leq \vartheta_u \ , \end{aligned} \tag{4.1}$$

where $\mathbf{x} \in \Omega \subset \mathbb{R}^n$ is an n-dimensional design vector, θ is a random vector representing geometric or flow variability and $\mathbb{E}_\theta$ stands for the operation of expectation with respect to θ. (Other functional dependencies of ϖ and ϑ are suppressed to simplify the notation.) ϑ_l and ϑ_u stand for lower- and upper-bound constraints on the mean turning angle.

Alternatively, the probabilistic optimization objective may be to reduce the loss coefficient variability, subject to mean turning and mean loss constraints, that is

$$\begin{aligned} \sigma^*_{\varpi} = \min_{\mathbf{x}\in\Omega} & \left\{ \mathop{\mathbb{E}}_{\theta} \left[\left(\varpi(\mathbf{x},\theta) - \mathop{\mathbb{E}}_{\theta} [\varpi(\mathbf{x},\theta)] \right)^2 \right] \right\}^{\frac{1}{2}} \\ \text{s.t.} \quad & \vartheta_l \leq \mathop{\mathbb{E}}_{\theta} [\vartheta(\mathbf{x},\theta)] \leq \vartheta_u, \\ & \mathop{\mathbb{E}}_{\theta} [\varpi(\mathbf{x},\theta)] \leq \varpi_u, \end{aligned} \tag{4.2}$$

where ϖ_u stands for the maximum allowable mean passage loss coefficient. This objective amounts to minimizing the uncertainty of the realized loss coefficient in the presence of geometric variability.

The sequential quadratic programming (SQP) method was employed in solving the nonlinear programs (4.1) and (4.2). SQP is a widely used gradient-based method for solving nonlinear constrained problems. At each iteration of the main algorithm, the Hessian of a Lagrangian function, formed by adding the objective function to the weighted sum of nonlinear constraints, is approximated using a quasi-Newton updating method. A quadratic programming subproblem is formed with the approximate Hessian and the resulting direction used in a line search procedure. Further details may be found in references such as [38] and [11]. The MATLAB [1] Optimization Toolkit implementation of the SQP algorithm was used to drive the probabilistic optimization procedure as shown in Fig. 4-1. Hessian matrix approximations were carried out using the Broyden-Fletcher-Goldfarb-Shanno (BFGS) updating [127].

[1]The Mathworks, Inc., Natick, MA, `http://www.mathworks.com`

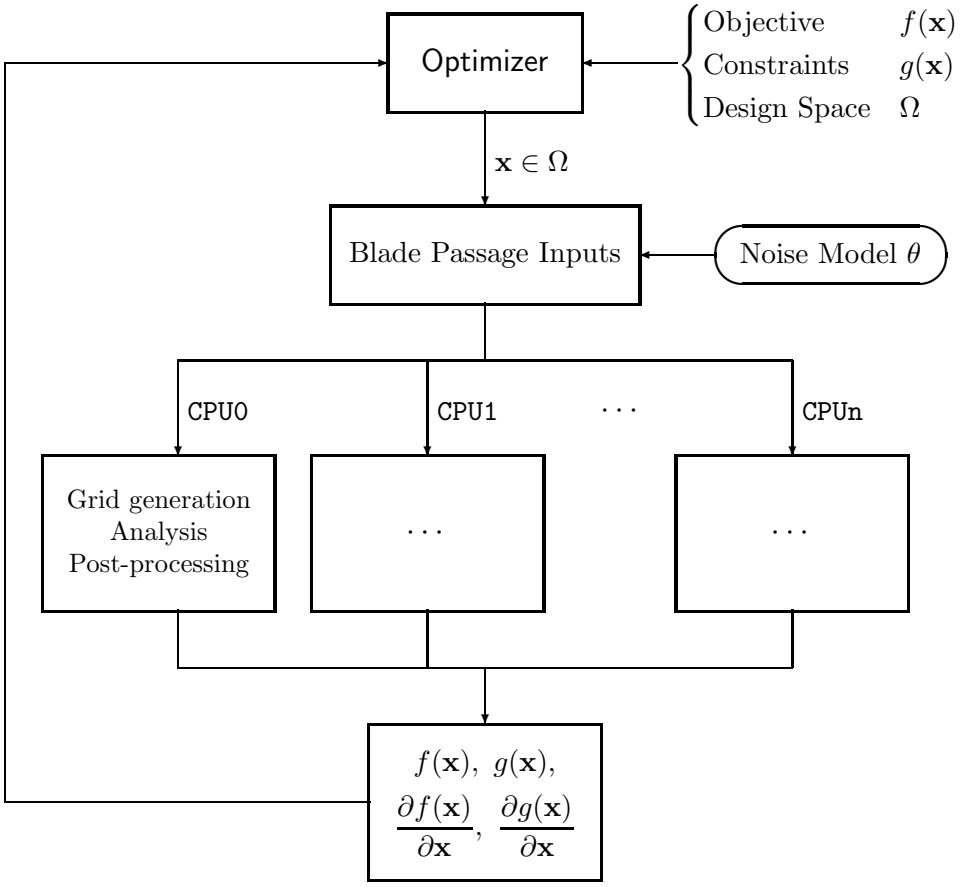

Figure 4-1: Parallel probabilistic optimization framework

The gradient information required by the probabilistic optimization algorithm, namely the Jacobian of the loss coefficient and turning with respect to the design variables, can be obtained from the sensitivity information provided by the flow solver. Under the assumption that the noise vector θ is independent of the design vector $\mathbf{x}$, it follows by linearity that

$$\begin{aligned}
\frac{\partial}{\partial x_i} \mathop{\mathbb{E}}_{\theta} [\varpi(\mathbf{x}, \theta)] &= \mathop{\mathbb{E}}_{\theta} \left[\frac{\partial}{\partial x_i} \varpi(\mathbf{x}, \theta) \right] \quad i = 1 \ldots n \\
\frac{\partial}{\partial x_i} \mathop{\mathbb{E}}_{\theta} [\vartheta(\mathbf{x}, \theta)] &= \mathop{\mathbb{E}}_{\theta} \left[\frac{\partial}{\partial x_i} \vartheta(\mathbf{x}, \theta) \right] \quad i = 1 \ldots n \ .
\end{aligned}$$

Similarly, after some manipulation,

$$\frac{\partial}{\partial x_i} \left\{ \mathop{\mathbb{E}}_{\theta} \left[\left(\varpi - \mathop{\mathbb{E}}_{\theta} [\varpi] \right)^2 \right] \right\}^{\frac{1}{2}} = \frac{\mathbb{E}_\theta \left[\varpi \frac{\partial \varpi}{\partial x_i} \right] - \mathbb{E}_\theta [\varpi] \, \mathbb{E}_\theta \left[\frac{\partial \varpi}{\partial x_i} \right]}{\left\{ \mathbb{E}_\theta \left[(\varpi - \mathbb{E}_\theta [\varpi])^2 \right] \right\}^{\frac{1}{2}}} \quad i = 1 \ldots n \quad (4.3)$$

Since the objectives and nonlinear constraints in (4.1) and (4.2) are probabilistic quantities, their functional evaluation implies the use of probabilistic analysis techniques. In Chapter 3, the Monte Carlo simulation (MCS) method was used to assess the impact of geometric and Mach number variability on loss coefficient and turning angle. The disadvan-

tage of using MCS in the present context is the excessive amount of computation required to accurately predict the variability of nonlinear functions such as the loss coefficient. Instead, in the optimization procedure, the mean and variance of loss and turning, as well as their derivatives with respect to the design variables, are replaced with *surrogates* consisting of "low-order" Monte Carlo predictions, i.e., using a small number of trials. For instance, the surrogate of $\mathbb{E}_\theta[\partial\varpi/\partial x_i]$ used during optimization is given by

$$\frac{1}{N}\sum_{j=1}^{N}\frac{\partial\varpi(\mathbf{x},\theta_j)}{\partial x_i} \ .$$

Similarly, the surrogate of (4.3) is given by

$$\frac{1}{N\sqrt{\hat{\sigma}_\varpi^2}}\sum_{j=1}^{N}\left[\varpi(\mathbf{x},\theta_j)-\hat{\mu}_\varpi\right]\frac{\partial\varpi(\mathbf{x},\theta_j)}{\partial x_i}$$

where

$$\hat{\mu}_\varpi=\frac{1}{N}\sum_{j=1}^{N}\varpi(\mathbf{x},\theta_j) \quad \text{and} \quad \hat{\sigma}_\varpi^2=\frac{1}{N-1}\sum_{j=1}^{N}\left[\varpi(\mathbf{x},\theta_j)-\hat{\mu}_\varpi\right]^2 \ .$$

The number of Monte Carlo trials, N, becomes another free parameter that may be selected according to the severity of the nonlinear behavior in a given application. Furthermore, N may be allowed to vary as the optimization proceeds to improve the resolution of the objective and constraints near the boundary of Ω or in the vicinity of extrema. Numerical experimentation suggested that values of N in the range of 40 to 100 were sufficient to successfully redesign transonic airfoils in the presence of geometric and inlet Mach number variability (see Sect. 4.2 below for concrete examples).

The current gradient-based approach assumes that sensitivities of output functions with respect to design variables are available to the optimizer. In aerodynamic shape optimization a number of methods have been introduced for this purpose. Finite difference approximations, although readily implementable, are often inadequate to simulation-based aerodynamic shape optimization [13, 36]. As an alternative to finite-difference approximations, automatic differentiation codes have been developed to simplify the task of computing discrete sensitivity approximations using existing flow solvers [126]. A more accurate, but initially more demanding approach, involves solving separate sensitivity equations derived from linearized versions of the governing equations [20, 131]. Adjoint methods, pioneered in fluids applications by Jameson [66], provide linearized sensitivity information at little additional computational expense [46]. CFD software implementing both continuous and discrete adjoint formulations have been available for some time [47, 90]. Socha presents a succinct summary of methods for sensitivity analysis of stochastic systems [118].

In MISES the sensitivity derivatives of various output flow quantities with respect to the design variables are available as by-products of the flow solution algorithm. The Jacobian matrix that is generated and factored at each step of the Newton-Raphson procedure contains the sensitivity derivatives of the flow solution with respect to global unknowns including the geometric design modes. Derivatives of flow dependent quantities, such as the loss coefficient or exit flow angle, are obtained by linearizing the quantity of interest with respect to the flow variables and applying chain-rule differentiation [141].

As discussed in Appendix C of Ref. 141, the linearized sensitivity information is in

general only valid in a small neighborhood around the current design point. Therefore care must exercised in selecting the maximum step-size that the optimizer can take during the line-search procedure.

4.2 Applications

4.2.1 Objectives and Constraints

To compare the behavior of redesigned airfoils in the presence of geometric variability three optimization problems are considered: one deterministic and two probabilistic. The deterministic program seeks to minimize the loss coefficient without considering geometric variability. This is expressed as

$$\begin{aligned} \varpi^* &= \min_{\mathbf{x}\in\Omega} \varpi(\mathbf{x}) \\ \text{s.t.} \quad \vartheta_l &\leq \vartheta(\mathbf{x}) \leq \vartheta_u \ , \end{aligned} \tag{DML}$$

where ϑ_l and ϑ_u are low- and high-turning constraints respectively. In contrast, the second program seeks to minimize the *mean* value of loss coefficient, subject to mean turning constraints:

$$\begin{aligned} \mu^*_\varpi &= \min_{\mathbf{x}\in\Omega} \mathop{\mathbb{E}}_{\theta} [\varpi(\mathbf{x},\theta)] \\ \text{s.t.} \quad \vartheta_l &\leq \mathop{\mathbb{E}}_{\theta} [\vartheta(\mathbf{x},\theta)] \leq \vartheta_u \ . \end{aligned} \tag{MML}$$

The objective of the third redesign is to reduce the *variability* of loss coefficient, as measured by its standard deviation, subject to mean turning and mean loss constraints,

$$\begin{aligned} \sigma^*_\varpi &= \min_{\mathbf{x}\in\Omega} \left\{ \mathop{\mathrm{Var}}_{\theta}(\varpi(\mathbf{x},\theta)) \right\}^{\frac{1}{2}} \\ \text{s.t.} \quad \vartheta_l &\leq \mathop{\mathbb{E}}_{\theta} [\vartheta(\mathbf{x},\theta)] \leq \vartheta_u, \\ & \mathop{\mathbb{E}}_{\theta} [\varpi(\mathbf{x},\theta)] \leq \varpi_u, \end{aligned} \tag{MSL}$$

for a given upper expected loss coefficient constraint ϖ_u. In what follows the three problems and their resulting redesigned geometries will be denoted DML (deterministic minimum loss), MML (minimum mean loss) and MSL (minimum standard deviation of loss) respectively.

Appendix C illustrates the use of probabilistic constrained optimization to carry out robust parameter design. In the sample application, the design space is explored by constraining mean performance at different levels and minimizing variability.

4.2.2 Geometric Design Modes

The design mode shapes used to optimize the baseline geometries consisted of modified Chebyshev polynomials of the first type, i.e.,

$$T'_n(x) = \frac{1}{n+1} \begin{cases} 1 - 2x - \cos[(n+1)\arccos(1-2x)], & n \text{ even} \\ 1 - \cos[(n+1)\arccos(1-2x)], & n \text{ odd} \end{cases}$$

$x \in [0,1]$, acting along the direction normal to the pressure or suction surfaces of the airfoil. The geometric modes that modify the airfoil geometry are then given by

$$g_k(s) = \begin{cases} a_k T'_{\frac{k+1}{2}}(-s)\hat{n}(s), & -1 \le s \le 0 \\ 0, & 0 < s \le 1 \end{cases}$$

for odd k and

$$g_k(s) = \begin{cases} 0, & 0 < s \le 1 \\ a_k T'_{\frac{k}{2}}(s)\hat{n}(s), & -1 \le s \le 0 \end{cases}$$

for k even, where $-1 \le s \le 1$ is the airfoil surface arc length coordinate, with negative values along the suction side and positive on the pressure surface as shown in Fig. 4-2. In principle the geometric design modes thus defined provide an orthonormal basis onto which to expand surface modifications to the interior of the airfoil surfaces(i.e., away from the leading and trailing edges). In addition to the surface-normal modes, a solid body rotation mode was included to allow for blade stagger changes. Axial chord length modifications were not considered. (See Ref. [44] for examples of leading and trailing edge droop modes used in probabilistic compressor airfoil optimization).

In MISES the airfoil geometry is represented by cubic splines which facilitates the calculation of the normal directions at any position on the surface of the airfoil. Figure 4-2(b) shows the modified Chebyshev polynomial mode shapes. The vector of design parameters $\mathbf{x} \subset \mathbb{R}^n$ is formed by the collection of modeshape amplitudes a_k, $k = 1, \ldots, n$ and a rotation angle ξ.

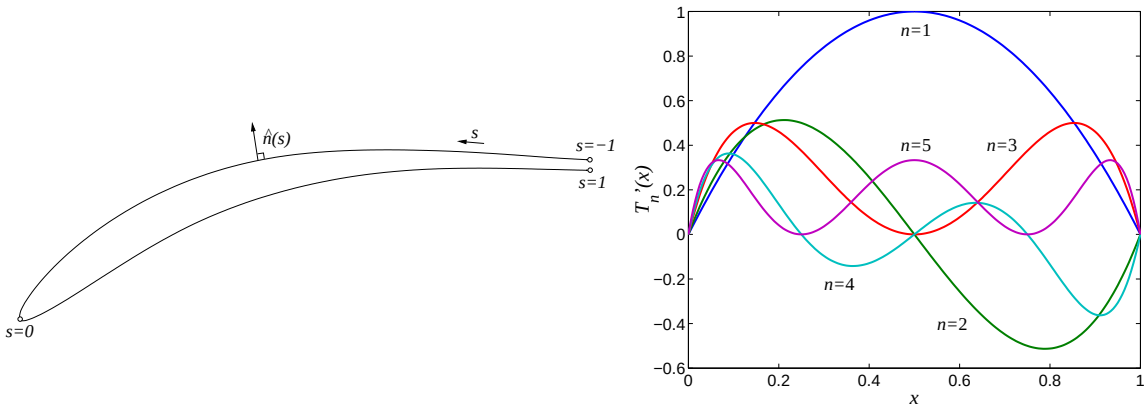

(a) (b)

Figure 4-2: Airfoil arc length coordinate conventions and modified Chebyshev polynomials $T'_n(x)$, $n = 1, \ldots, 5$

4.2.3 IBR Rotor Mid-Span

The IBR airfoil was previously introduced in Chapters 2 and 3. The trade space selected to redesign this airfoil was $\Omega = [-0.008, 0.008]^n \times [-0.05, 0.05] \subset \mathbb{R}^{n+1}$ where the a_k's (amplitudes of modified Chebyshev polynomials) are given in fractions of chord length

and the stagger angle in radians. Eight parameters ($n = 8$) were used to redesign the IBR, DFVLR and R37 airfoils; that is, the first four modified Chebyshev polynomials described above acting independently on convex and concave airfoil surfaces. Although the use of Monte Carlo simulation lessens the impact of number of design variables on computational expense, a relatively low number of design modeshapes was employed to preclude the formation of undesirable localized geometric features (e.g., surface "waviness" or "bumps").

The boundaries of the tradespace hypercube were selected so as to permit large baseline shape modifications without allowing unphysical geometries, i.e., collapsed airfoils. No other thickness constraints were explicitly incorporated in the problems as the emphasis in the present investigation is on aerothermal rather than aeromechanical performance. The same design space was explored in all three redesign cases. All optimization calculations started from the baseline geometry, i.e., initial guess $\mathbf{x}^0 = \mathbf{0}$.

The prescribed turning constraints were $14.4^\circ \leq \vartheta \leq 14.5^\circ$ in the deterministic case and $14.4^\circ \leq \mathbb{E}_\theta[\vartheta] \leq 14.5^\circ$ for the probabilistic programs.

The PCA-based geometric noise model discussed in Chapters 2 and 3 was used to perturb the baseline airfoil to simulate geometric variability during optimization. As in Chapter 3, three levels of geometric variability were considered, $a = 1$, 2 and 5.

Table 4.1 summarizes the number of trials used in estimating loss and turning statistics, as well as the number of SQP iterations and functional evaluations required to achieve convergence. Absolute convergence tolerances of 10^{-5} on $\Delta f(\mathbf{x})$ and $\|\Delta\mathbf{x}\|$ were imposed for the three redesign cases. The increase in computational expense incurred in going from

Table 4.1: Number of trials, iterations and function evaluations

Program	N_{opt}	# SQP iter	# $f(\mathbf{x})$ eval	# MISES runs
DML	-	13	151	151
MML	100	42	138	13800
MSL	100	16	56	5600

deterministic to probabilistic optimization can be seen by comparing the entries of the last column in Table 4.1, which shows number of MISES runs required for each optimization. Despite the large number of MISES evaluations required, the use parallel hardware greatly reduced the total wall-clock time. As mentioned earlier parallelization of Monte Carlo simulation trials can be readily implemented using simple shell scripts and the resulting speed-ups increase nearly linear with the number of processors used. In addition, since the same population of perturbed airfoils was used throughout the optimization procedure, the resulting MISES states were saved and reused to initialize the subsequent calculations, greatly decreasing the overall computing time.

The number of trials used during the optimization, N_{opt}, was selected by numerical experiments in which the total computational expense was weighed against the degree of improvement achieved. It was found that the number of trials required depends also on the level of geometric variability. The sample values presented in Table 4.1 correspond to PCA-based noise level $a = 1$.

The relatively small number of trials required to achieve the levels of improvement reported below serve as motivation for the proposed approach to probabilistic optimization.

During the optimization step the emphasis is not on accurately predicting loss and turning statistics, but rather on driving the redesign in the general direction of statistical improvement, as given by the gradients of the probabilistic objectives (e.g., Eq. (4.3)).

Figure 4-3 shows histograms of final Monte Carlo simulations ($N = 2000$) for the redesigned IBR airfoil at baseline geometric noise level. The performance statistics are also summarized in Table 4.2. In all final Monte Carlo simulations, the fraction of successful trials (i.e., those for which MISES converged to a physically acceptable solution) was upward of 99% of the total. Comparing the results for the baseline and deterministically redesigned airfoils, it is observed that both nominal and mean loss coefficient have decreased by about 18%. Similarly, the loss COV decreased by about 25%.

The probabilistically redesigned airfoils exhibit lower loss coefficient variability than either the baseline airfoil or—more appropriate for comparison—the deterministically redesigned airfoil. The MML redesign has the same nominal and mean loss coefficient as the DML redesign, but exhibits about 8% less variability. On the other hand, when optimizing for reduced variability, as in the MSL case, the COV of loss coefficient has been reduced by 54% when compared with the deterministic redesign and by 65% from the baseline design; the mean-shift for the MSL redesign is 17% lower than for the mininum loss airfoils. On the other hand, the MSL redesign produces about 5% higher nominal and mean loss coefficient than the DML and MML airfoils. The mean turning constraint has been satisfied by the three redesigned airfoils and the standard deviation of turning angle is less than one-tenth of one degree in all cases.

Table 4.2 summarizes aerodynamic performance statistics for the redesigned IBR airfoils at geometric noise amplitudes $a = 1$, 2 and 5. At the noise level $a = 2$, where the impact of the geometric noise scatter becomes comparable to that of the mean geometry. The shift in mean loss from its nominal value is about 5% for both the baseline and deterministic redesigns, but the latter produced 20% less variability in loss coefficient.

Table 4.2: Summary of performance statistics for redesigned IBR airfoils, $a = 1, 2, 5$

a	Design	ϖ^0	μ_ϖ	$\sigma_\varpi \times 10^3$	$\%V_\varpi$	ϑ^0	μ_ϑ	σ_ϑ	$\%V_\vartheta$
1	Base	0.0272	0.0282	0.804	2.850	14.40	14.27	0.087	0.612
	DML	0.0224	0.0230	0.490	2.130	14.50	14.40	0.074	0.515
	MML	0.0224	0.0230	0.450	1.960	14.60	14.50	0.076	0.521
	MSL	0.0235	0.0242	0.238	0.985	14.57	14.49	0.083	0.575
2	Base	0.0272	0.0288	1.550	5.36	14.40	14.25	0.170	1.19
	DML	0.0224	0.0235	0.998	4.24	14.50	14.38	0.148	1.03
	MML	0.0224	0.0235	1.020	4.35	14.58	14.46	0.150	1.04
	MSL	0.0239	0.0249	0.670	2.69	14.60	14.49	0.165	1.14
5	Base	0.0272	0.0334	4.95	14.9	14.40	14.11	0.442	3.13
	DML	0.0224	0.0271	3.52	13.0	14.50	14.25	0.397	2.79
	MML	0.0231	0.0274	3.47	12.7	14.73	14.49	0.410	2.83
	MSL	0.0243	0.0278	2.78	10.0	14.68	14.47	0.414	2.86

For $a = 2$, the MML redesign has roughly the same statistics as the deterministically redesigned airfoil, with slightly larger loss COV. On the other hand, the minimum-variability redesign, MSL, produced a 37% smaller loss COV than the deterministic redesign. The

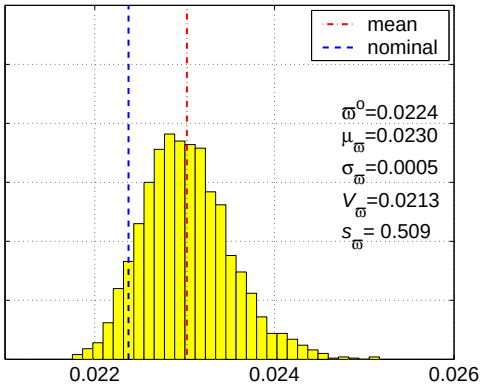

(a) DML: Loss Coefficient

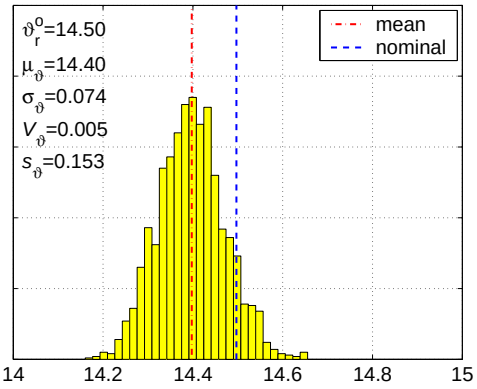

(b) DML: Turning Angle

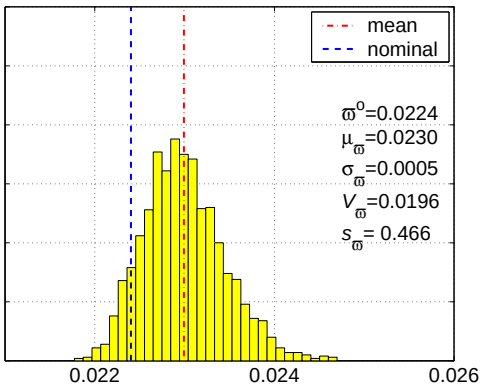

(c) MML: Loss Coefficient

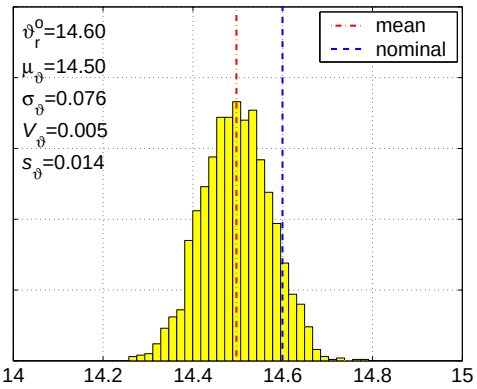

(d) MML: Turning Angle

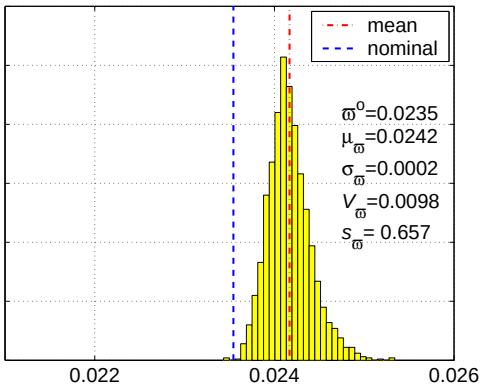

(e) MSL: Loss Coefficient

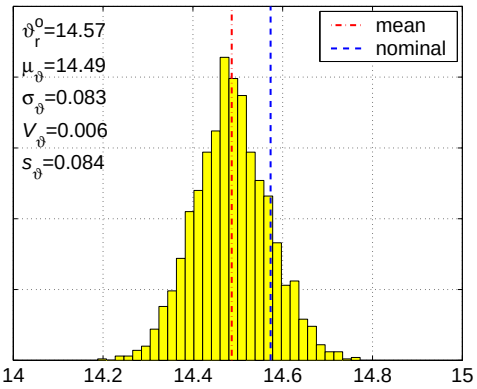

(f) MSL: Turning Angle

Figure 4-3: IBR: Deterministic vs. probabilistic optimization ($a = 1$, $N = 2000$)

reduction in variability from the DML to MSL redesigns was accompanied by an increase in mean loss coefficient of roughly 6%. In addition, at the $a = 2$ noise level there is little difference in the turning variability among the redesigned airfoils (although in all cases it is lower than the baseline design) and the mean turning constraints have been satisfied.

At the more realistic $a = 5$ noise level (see Appendix B) the trends are similar to those at $a = 2$. The DML and MML exhibit similar values of nominal and mean loss coefficient and loss COV. The reduction in loss COV between the deterministic and MSL redesigns is 30%, and the latter exhibits a 26% smaller loss mean shift. The decrease in variability can also be appreciated graphically in Fig. 4-4 which shows histograms of loss coefficient at the $a = 5$ noise level.

Figure 4-4 also shows the change in skewness incurred as the geometric noise amplitude increased from $a = 1$ to $a = 5$. At the original noise level, the loss skewness coefficient is 0.3 for the baseline airfoil and 0.7 for the MSL redesign, while at the $a = 5$ level the corresponding values are 1.2 and 1.5. The increase in skewness highlights the larger contribution to loss variability of the geometric scatter as noise amplitude increases.

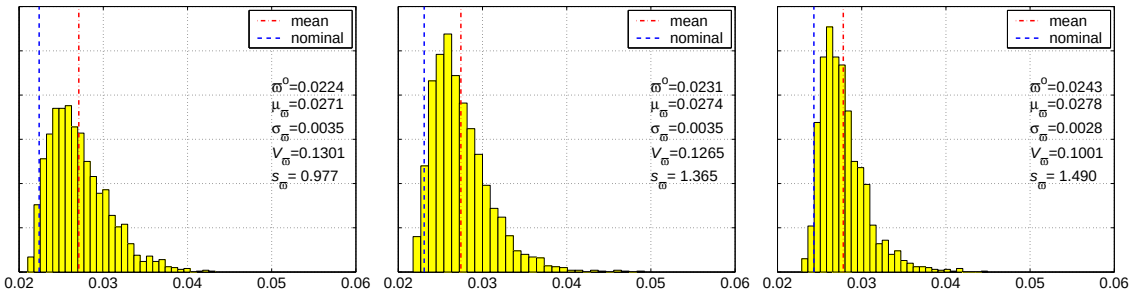

(a) DML (b) MML (c) MSL

Figure 4-4: IBR: Loss coefficient statistics for redesigned airfoils ($a = 5$, $N = 2000$)

Figure 4-5 compares the baseline and redesigned nominal airfoil's geometric characteristics for the $a = 5$ case. Figure 4-5(a) shows the effect of the stagger mode which acts as a solid-body rotation of the airfoil about its trailing edge. The change in stagger for the redesigned airfoils is about two degrees for the minimum-loss redesigns and $\frac{1}{2}^\circ$ for the MSL airfoil. In Fig. 4-5(b), showing airfoil sections at zero stagger angle, the vertical axis has been scaled by a factor of 10 to facilitate comparison. Figures 4-5(c) and (d) depict mean camber and thickness respectively. A feature common to the three redesigns is an increase in airfoil thickness, particularly on the forward half of the airfoil on the suction side, and near the trailing edge on the pressure side. The DML and MML airfoil shapes are qualitatively the same, with a shifting forward (toward the leading-edge) of the maximum camber location from about 60% chord to 45% chord and a pronounced thickening on the aft 40% of the pressure surface. The latter change is needed to meet the mean turning constraint requirement and may be avoided by adding a trailing-edge deflection mode; it is more pronounced on the deterministically redesigned airfoil. The minimum-loss airfoils are in general thicker than the original one, but somewhat thinner than the MSL redesign on the forward 20% chord and again mid-chord. Unlike the baseline and minimum-loss airfoils, the MSL redesign shows a thickening on the forward 20% of the pressure side. The MSL

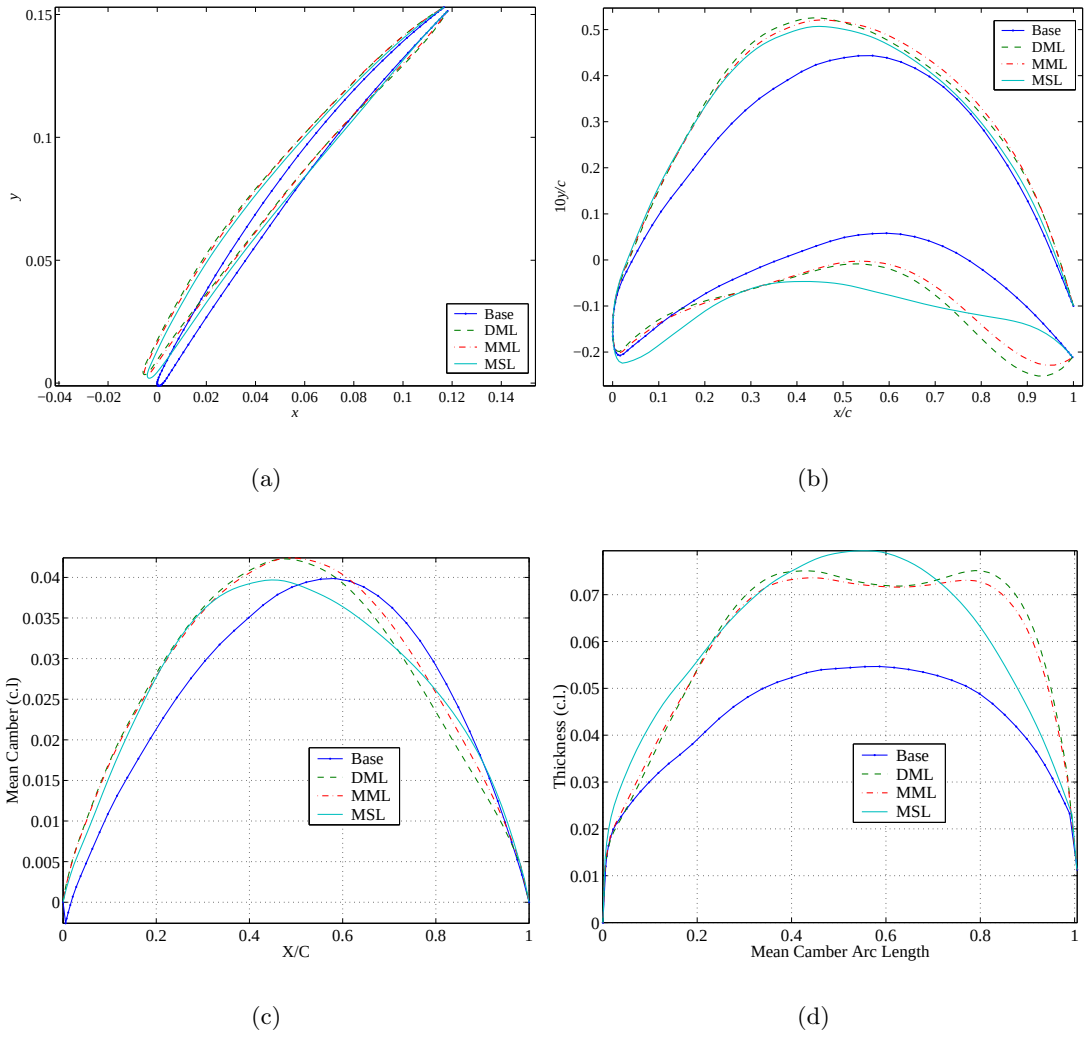

(a) (b)

(c) (d)

Figure 4-5: IBR mid-span: Redesigned nominal airfoil shape ($a = 5$)

maximum thickness occurs slightly behind mid-chord unlike the minimum-loss airfoils. The MSL maximum camber occurs at about 45% chord, but has roughly the same value as the baseline airfoil (about 5% less than the minimum-loss blades). Similar geometric trends were observed in the redesigned airfoils at noise levels $a = 1$ and $a = 2$. The effects of these geometric modifications on aerodynamic performance are discussed next.

Figure 4-6 shows plots of nominal and mean pressure coefficient on the surface of the baseline, DML and MSL airfoils for the three noise levels considered. In all cases, the minimum-loss airfoil shows a less pronounced initial flow deceleration than baseline on the suction side, followed by a small plateau and a steep pressure recovery region near the trailing edge. Beyond the stagnation point on the pressure side of the DML airfoil, the flow accelerates and then experiences a steeply adverse pressure gradient until about 10% chord. In the aft 20% of the pressure surface the flow first accelerates and then diffuses rapidly near the trailing edge, in accordance to the pronounced airfoil thickening noted earlier. The nominal and mean reductions in loss coefficient from the baseline case can be attributed in part to the milder diffusion that the flow experiences because of the re-cambering toward on the forward section of the airfoils. The corresponding pressure distributions are reminiscent of typical "controlled diffusion" airfoils [58].

In contrast to the minimum loss airfoils, the MSL redesigns present a less adverse pressure gradient along the first 20% of the pressure surface chord, as a consequence of the local thickening and increased camber. This features is common to MSL redesigns at all three noise levels. The effect of the milder pressure gradient is illustrated in Fig. 4-7 which shows plots of momentum thickness (θ/c) on the suction and pressure sides (indicated in the plots by SS and PS respectively) of the DML and MSL redesigned airfoils. The dashed and dot-dashed lines indicate the nominal values—i.e., without geometric noise—while the solid lines indicate the mean values from Monte Carlo simulation; the error bars correspond to a one-standard-deviation interval centered at the mean. The deterministic redesign produces lower nominal momentum thickness (dashed line) than the MSL airfoil, but in the presence of geometric variability the mean-shift and variability are clearly larger for the former.

The effect of MSL redesign on performance variability is illustrated further in Fig. 4-8, showing plots of boundary layer shape parameter $H = \delta^*/\theta$ near the leading-edge of the DML and MSL airfoils. Values of H above four indicate possible downstream flow separation [19]. On the pressure side, the DML airfoil has considerably larger mean shape parameter values and more variability than the MSL airfoil. Although nominal shape parameter values on the pressure side do not exceed four, the DML mean values are as high as 10 near $x/c = 0.03$ where the standard deviation is approximately nine. In contrast, the MSL pressure side shape parameter mean values do not exceed seven with a standard deviation of about six. It follows that the MSL airfoil is less likely to exhibit values of H above four (indicating possible separation) on the pressure side than the DML airfoil.

Figure 4-9 compares the cumulative values of $\rho U_e^3 C_d'$ along the suction and pressure surfaces of the redesigned airfoils. The impact of geometric variability on boundary layer dissipation coefficient, C_d', and entropy generation rate was discussed previously in Chapter 3 (see Eqs. (3.6) and (3.7)). Of the four, the baseline airfoil produces the highest cumulative nominal and mean values of $\rho U_e^3 C_d'$ at the trailing edge. By comparison, the minimum-loss optimized airfoil produced lower final nominal loss generation rate values on the pressure side with somewhat reduced uncertainty. The nominal value of $\int \rho U_e^3 C_d' dx$ along on the pressure side are similar for the three redesigned airfoils, but the MSL redesign shows the smallest mean shift and less variability at the trailing edge.

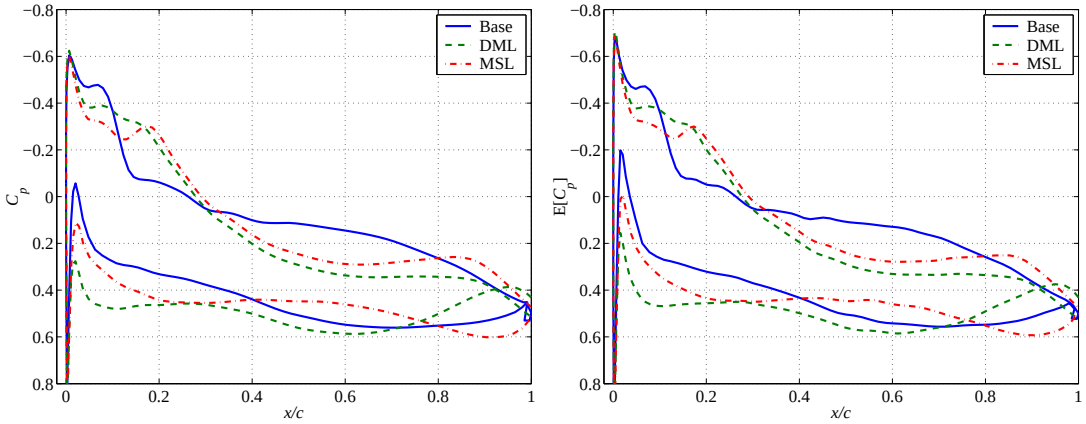

(a) C_p, $a = 1$

(b) $\mathbb{E}[C_p]$, $a = 1$

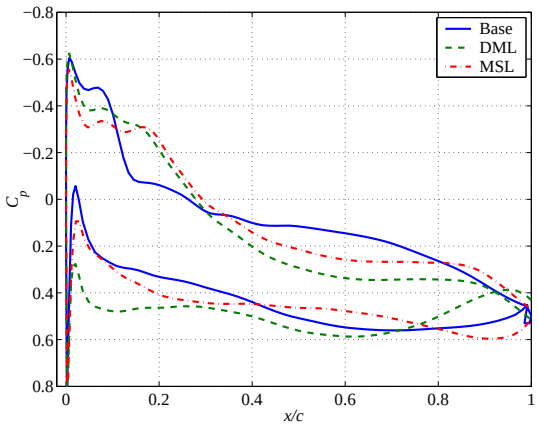

(c) C_p, $a = 2$

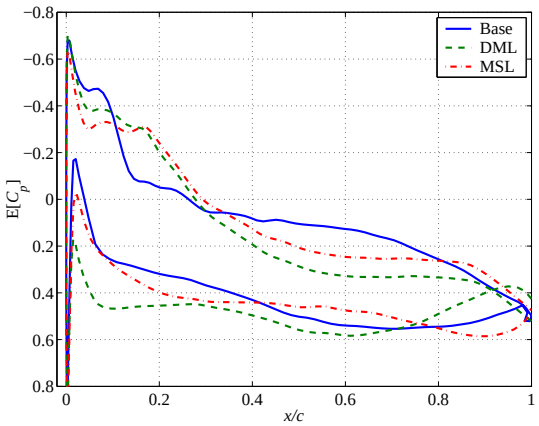

(d) $\mathbb{E}[C_p]$, $a = 2$

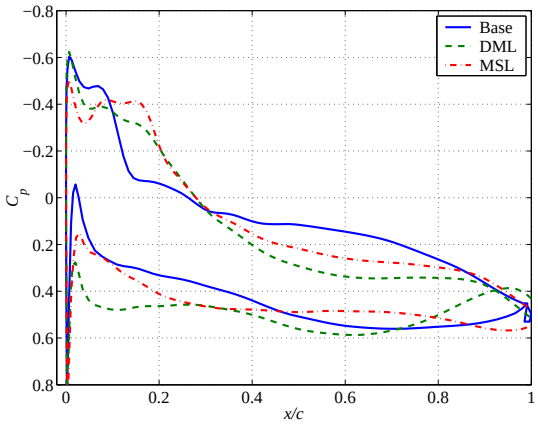

(e) C_p, $a = 5$

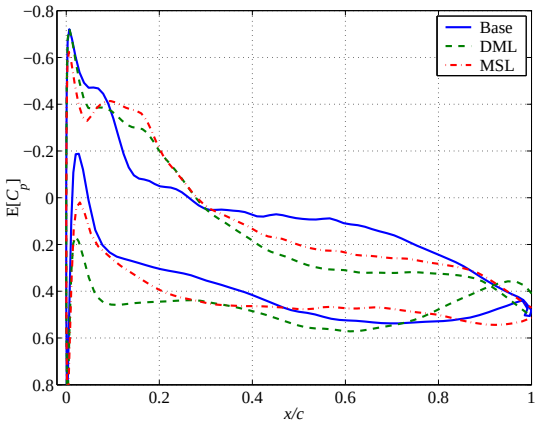

(f) $\mathbb{E}[C_p]$, $a = 5$

Figure 4-6: IBR mid-span: Baseline and mean pressure coefficient

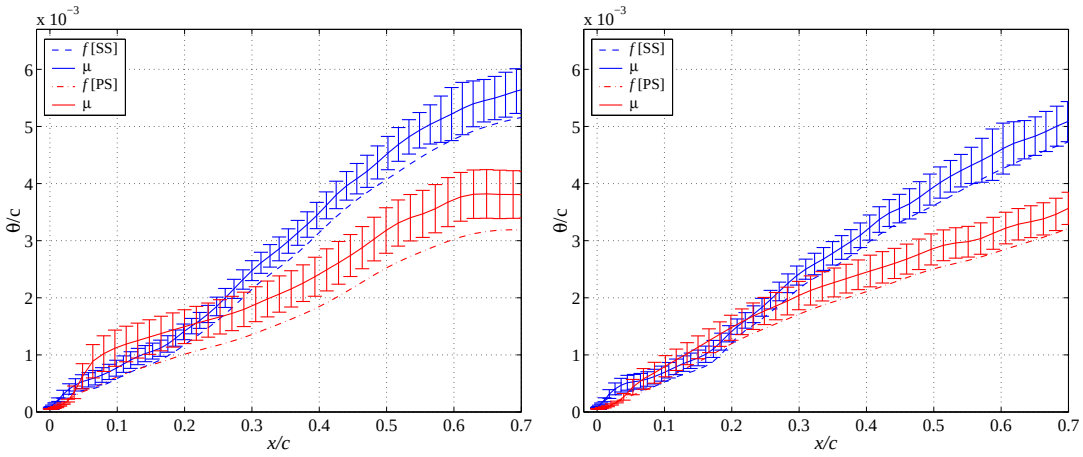

(a) DML

(b) MSL

Figure 4-7: IBR mid-span: Momentum thickness θ/c ($a = 5$)

The redesigned airfoils result in a less pronounced rate of increase of $\mathbb{E}[\int \rho U_e^3 C_d' dx]$ than the baseline geometry on the first 10% of the pressure surface. The MSL redesign has higher average values of $\int \rho U_e^3 C_d' dx$ on the suction and pressure sides, which explains in part its higher mean total pressure loss when compared with the DML and MML airfoils.

4.2.4 DFVLR Cascade Airfoil

In redesigning the nominal shape of the DFVLR airfoil, the tradespace was selected to be $\Omega = [-0.01, 0.01]^n \times [-0.05, 0.05]$ where again the mode amplitudes a_k are given in chord lengths. As in the previous case, $n = 8$ surface-normal and one stagger modes were used. The prescribed turning constraints were $9^\circ \leq \vartheta \leq 9.5^\circ$ and $9^\circ \leq \mathbb{E}_\theta[\vartheta] \leq 9.5^\circ$ for the deterministic and probabilistic problems respectively. In the latter $N_{\text{opt}} = 100$ trials were used to compute the loss and turning statistics as well as those of their sensitivity derivatives during the optimization procedure. The optimization algorithm's absolute tolerances were again 10^{-5} on both $\Delta f(\mathbf{x})$ and $\|\Delta \mathbf{x}\|$. The noise model used to simulate geometric and inlet flow condition variability was the same as that described in Chapter 3 in the context of assessing the impact of geometric noise on aerodynamic performance. Three geometric modes were considered: twist, overall section thickness change and leading edge bluntness. In addition Mach number variability was considered. The input noise statistics were summarized in Table 3.2 on page 47.

Table 4.3 summarizes the final loss coefficient and turning statistics for the baseline and redesigned sections computed via Monte Carlo simulation ($N = 2000$). As required, the deterministic redesign exhibits lower nominal loss than the baseline design (a 17% decrease). Accordingly the expected value of the loss coefficient has dropped by a similar proportion. However, the loss coefficient for the deterministically redesigned blade exhibits 14% higher COV than the baseline design. When compared with the deterministic redesign, the probabilistic MML redesign shows similar nominal and mean loss coefficient values. In contrast, the loss variability of the probabilistic minimum-loss redesign is 32% lower than

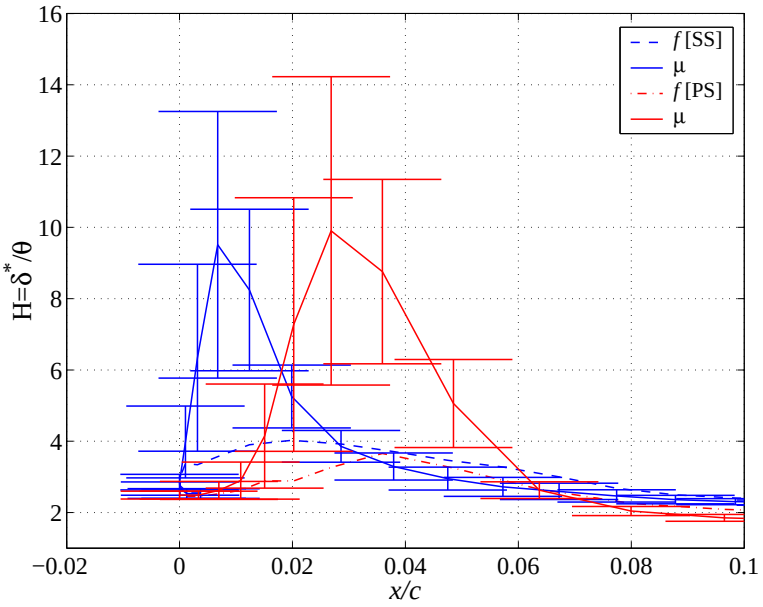

(a) DML

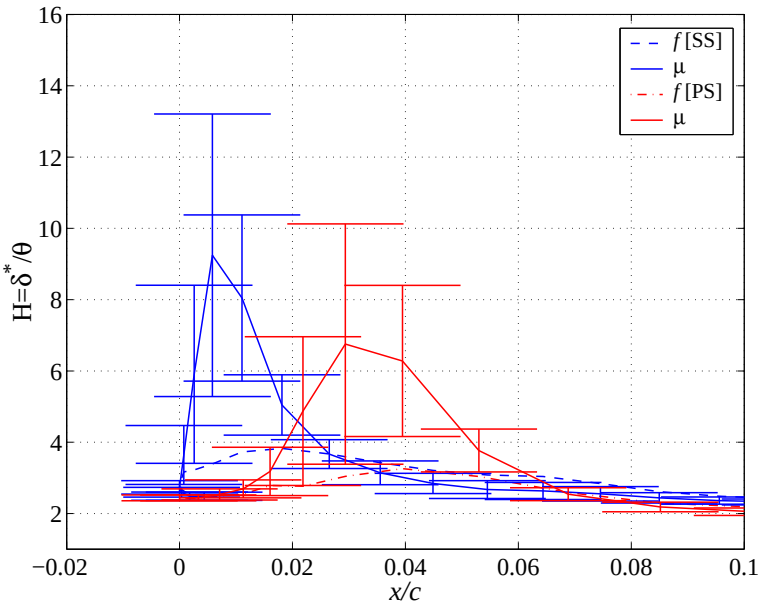

(b) MSL

Figure 4-8: IBR mid-span: Shape parameter $H = \delta^*/\theta$ ($a = 5$)

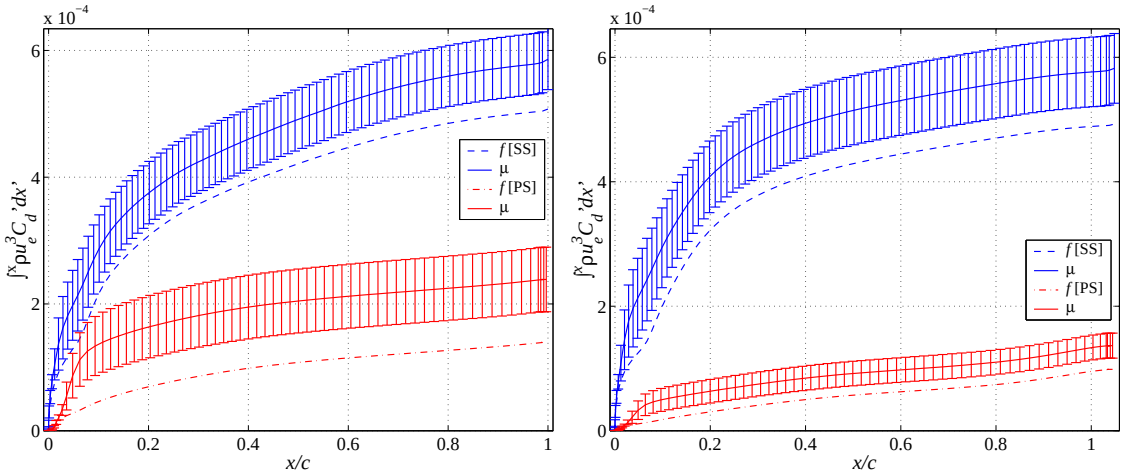

(a) Baseline

(b) DML

(c) MML

(d) MSL

Figure 4-9: IBR mid-span ($a = 5$): $\int_0^x \rho U_e^3 C_d' dx'$

the deterministic redesign.

Table 4.3: DFVLR: Redesigned airfoil statistics

Design	ϖ^0	μ_ϖ	$\sigma_\varpi \times 10^3$	$\%V_\varpi$	ϑ^0	μ_ϑ	σ_ϑ	$\%V_\vartheta$
Baseline	0.0297	0.0315	2.07	6.56	9.26	9.27	0.94	10.1
DML	0.0246	0.026	1.94	7.47	9.498	9.43	0.96	10.1
MML	0.0249	0.0259	1.47	5.68	9.546	9.48	0.94	9.9
MSL	0.0269	0.0272	0.84	3.07	9.546	9.47	0.91	9.7

As with the IBR blade, the airfoil redesigned probabilistically for reduced variability (MSL) shows larger nominal and mean loss coefficient than the minimum-loss redesigns (about 5% larger in both cases). The uncertainty in loss coefficient has been decreased by nearly 60% from the deterministic redesign and by 46% from the MML airfoil. Figure 4-10 shows histograms of the MC results. The 17% "mean shift" and the narrowing of the distribution are discernible, as are the higher nominal and mean loss coefficient values.

The Monte Carlo confirmation turning statistics summarized in Table 4.3 are similar for all the redesigned airfoils, with somewhat larger nominal and mean values than the baseline case. The mean turning constraints were satisfied by all the redesigned airfoils.

Figure 4-11 shows scatter plots of loss coefficient versus turning angle from Monte Carlo results. The location of mean loss and turning as well as the loss coefficient 6σ (six standard deviations) interval are also shown in the plots. The plots illustrate, in addition, the loss coefficient response to the twist mode since, in the interval considered, turning is linearly correlated with that mode. The rate of increase in loss away from the nominal operating condition is greater for the minimum loss redesigns, particularly for negative incidence (lower turning), resulting in an increased loss spread. The primary effect of the probabilistic MSL redesign is to reduce the sensitivity to incidence variability away from the nominal operating condition by re-centering the "loss bucket", therefore increasing the low-loss incidence range at the expense of mean performance.

Figure 4-12 compares baseline and redesigned nominal airfoil geometries. Figure 4-12(a) shows the effect of the stagger changes incurred by the redesigns: -1.1, -1.4 and -1.6 degrees for the DML, MML and MSL cases respectively. Figure 4-12(b), depicts airfoil sections at zero stagger angle with vertical axis scaled up by a factor of 10 to facilitate comparison. Figures 4-12(c) and (d) depict mean camber line slope and thickness respectively. As in the IBR case, the redesigned airfoils share in common ad change in maximum camber location, but unlike the IBR case, not all the the redesigned airfoils are thicker than the nominal section.

For all three redesigned sections, the maximum camber location moved forward by about 10% of the chord length and decreased by 10 to 15% in magnitude, with the higher value corresponding to the MSL airfoil—which also has correspondingly higher incidence. The minimum-loss redesigns have similar thickness and camber distributions, but the MML airfoil is about 5% thicker than the deterministically optimized airfoil.

As with the IBR case, the MSL DFVLR airfoil is thicker than the minimum-loss redesigns along the forward half of the chord; but the trend reverses somewhat for the rear 20% of the airfoil. Furthermore, the MSL airfoil is thicker than the baseline section for the first 80% of the airfoil. The MSL airfoil also has a less pronounced mean camber line slope

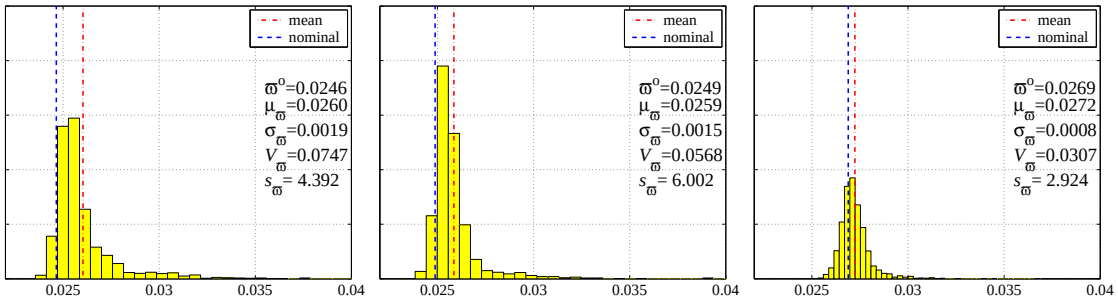

(a) DML redesign (b) MML redesign (c) MSL redesign

Figure 4-10: DFVLR loss coefficient for redesigned airfoils

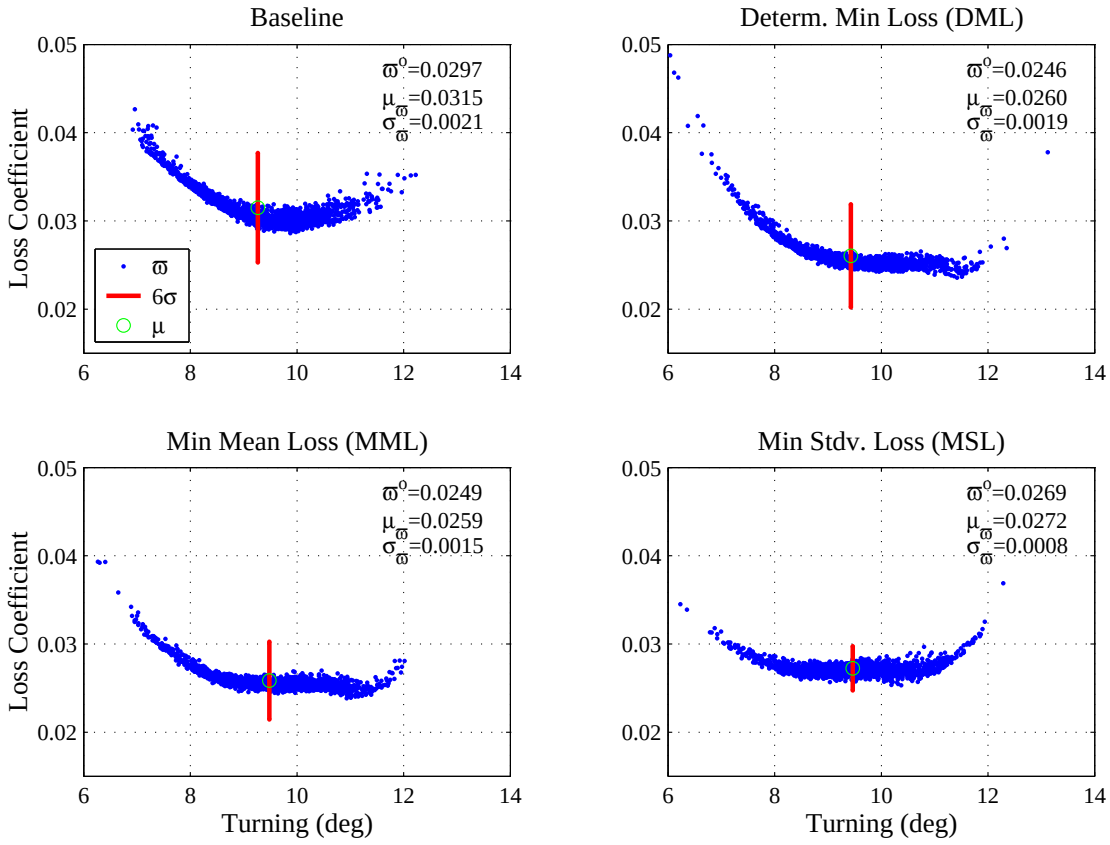

Figure 4-11: DFVLR: Scatter of Loss coefficient vs. turning angle

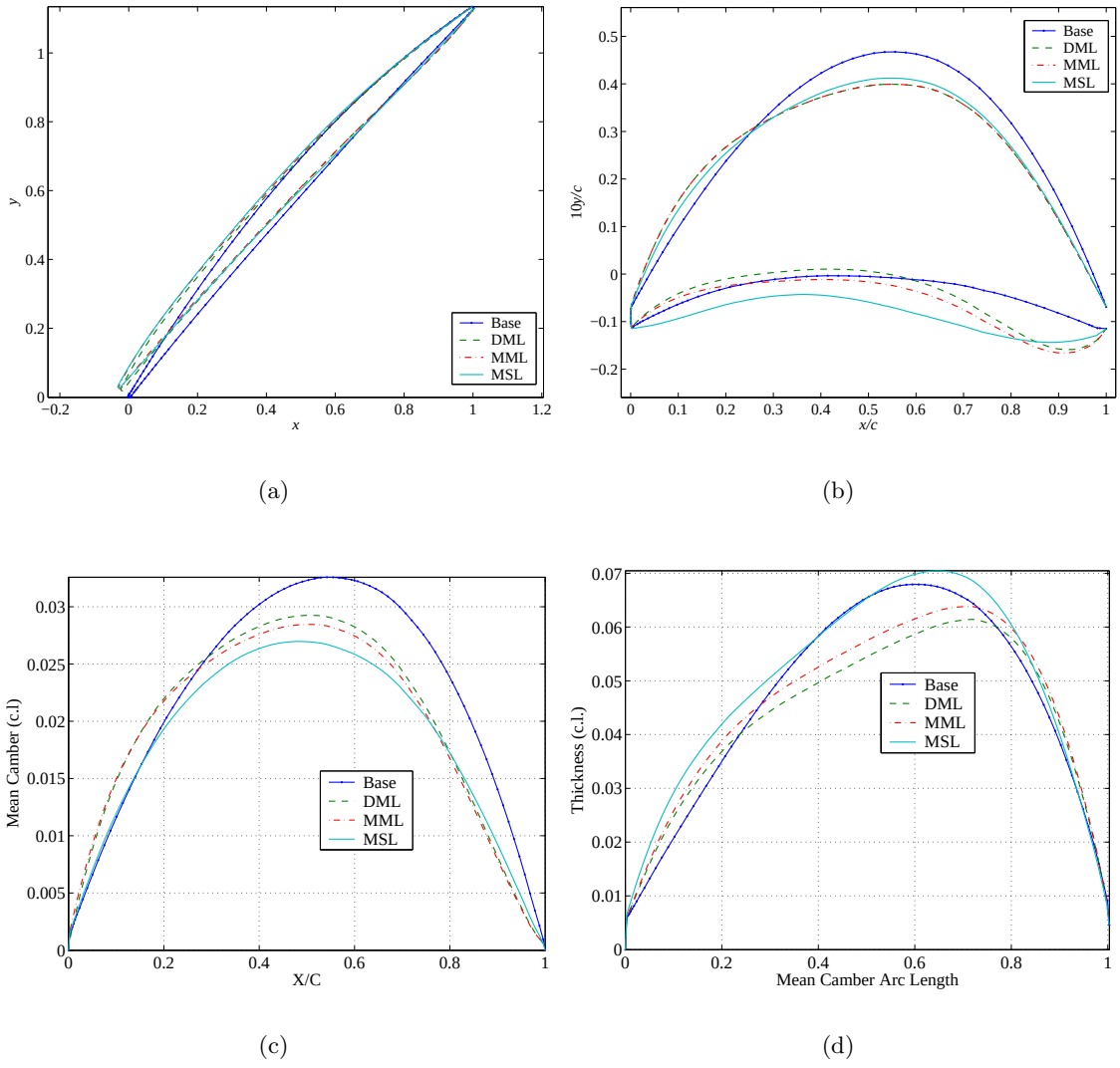

(a) (b)

(c) (d)

Figure 4-12: DFVLR cascade: Redesigned nominal airfoil shape

than the DML or MML airfoils on the front 15% of the airfoil, and less camber for the first 70%, indicating a shifting in loading similar to that shown in the IBR MSL redesign. Figure 4-12(b) shows that the camber and thickness distribution change in the forward part of the airfoil are more noticeable on the pressure side: as with the IBR case, the MSL redesign shows the thickening is more pronounced on the pressure side of the airfoil.

Figure 4-13 shows plots of nominal and mean pressure coefficient for the baseline and probabilistically redesigned MML and MSL airfoils.

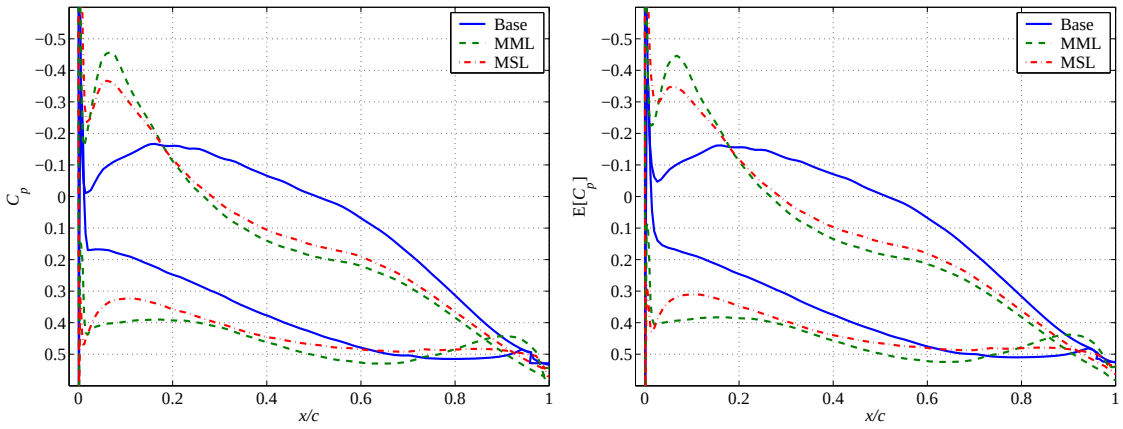

(a) C_p (b) $\mathbb{E}[Cp]$

Figure 4-13: Redesigned DFVLR airfoil: Pressure coefficient

The MML pressure distribution is similar to that of typical controlled diffusion blades: on the suction side the flow accelerates to the boundary layer transition point, the flow is then decelerated continuously to the trailing edge without a shock forming; on the concave side the pressure is kept nearly constant over most of the blade surface with exception of the rear 30% of the blade where the flow is first accelerated and then diffused near the trailing edge, again due to the modifications to the trailing edge imposed by the mean-turning constraint. The deterministically redesigned airfoil produced a pressure distribution nearly identical to that of the MML airfoil in agreement with their similar geometry and performance.

As with the IBR blade, the key difference between the MML and MSL pressure distributions is a qualitative change in the initial diffusion region on the pressure side. In fact, while the MML airfoil exhibits a nearly constant pressure coefficient for the first quarter chord, the flow on the MSL airfoil is accelerated for the first 10% chord and then expanded gradually till mid-chord. On the suction side of the DML and MSL pressure distributions are similar.

Figure 4-14 shows the impact of the minimum-variability redesign on suction-side momentum thickness statistics, as compared with those of the MML airfoil. Although the mean values of θ are similar, the variability about the mean and the nominal-to-mean discrepancy are noticeably smaller for the MSL redesign.

The effect of MSL redesign on performance variability is further illustrated in Figs. 4-15 and 4-16 showing plots of shape parameter H and entropy generation rate respectively. On the pressure side, the MML airfoil has considerably larger nominal and mean shape

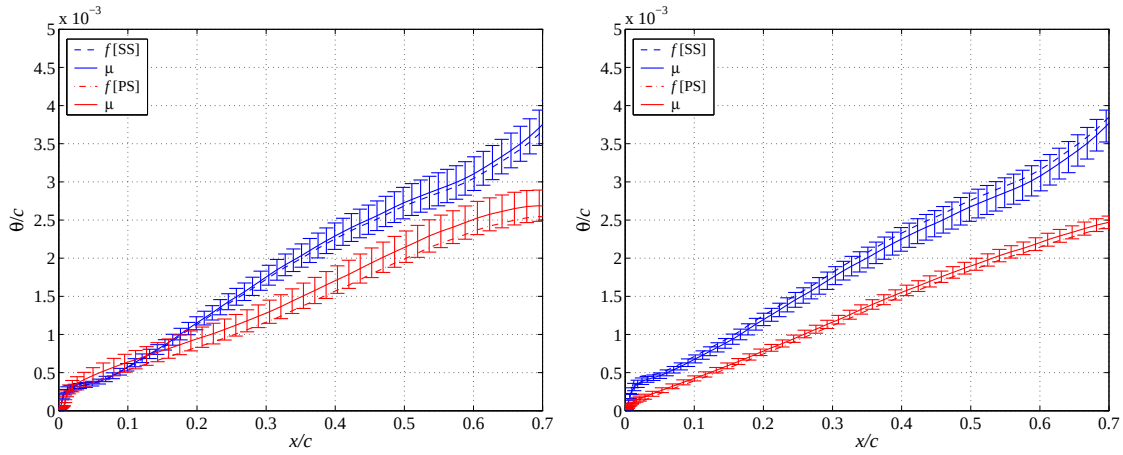

(a) MML: θ

(b) MSL: θ

Figure 4-14: redesigned DFVLR airfoil: Momentum thickness

parameter values with larger variability than the MSL airfoil. On the suction surface the mean H values are similar for both airfoils. The trends of entropy generation rate per unit span (as per Eq. (3.7)) shown in Fig. 4-16 are similar to those of the IBR airfoil: the minimum-loss airfoil has lower nominal and mean values on the suction surface (with a less abrupt initial rate of increase), but the pressure side exhibits both a slightly larger mean and substantially more variability at the trailing edge.

4.2.5 Rotor 37 Mid-Span

The nominal flow conditions and performance under geometric variability of the R37 airfoil were discussed in Sect. 3.3.3. The tradespace considered for redesigning the R37 airfoil was $\Omega = [-0.006, 0.006]^n$ with $n = 8$, i.e., no stagger angle changes were considered. The turning constraints were $14.5^\circ \leq \vartheta \leq 15^\circ$ in the deterministic case and $14.5^\circ \leq \mathbb{E}_\theta[\vartheta] \leq 15^\circ$ for the probabilistic programs. During the probabilistic optimization $N_{\text{opt}} = 100$ trials were used to approximate mean and standard deviation gradients for loss and turning with respect to the design vector $\mathbf{x}$.

As with the DFVLR cascade, twist, thickness, leading-edge bluntness and Mach number modes were used to simulate geometric and inlet flow condition variability. The input noise statistics are summarized in Table 3.3 on page 51.

The final loss and turning statistics for the redesigned airfoils were computed via Monte Carlo simulation with $N = 2000$ trials. Table 4.4 summarizes the MCS results. Both the deterministic and probabilistic redesigns that aimed at reducing loss coefficient exhibit similar nominal, mean and standard deviation values for loss and turning. When compared with the original design, the DML and MML redesigns show a reduction in nominal and mean loss coefficient of nearly 30%.

The MSL redesign resulted in a reduction of loss coefficient variability: compared with the deterministically redesigned airfoil, the MSL redesign has a nearly 20% smaller loss COV. Similarly, the reduction in loss coefficient COV is around 36% from the baseline

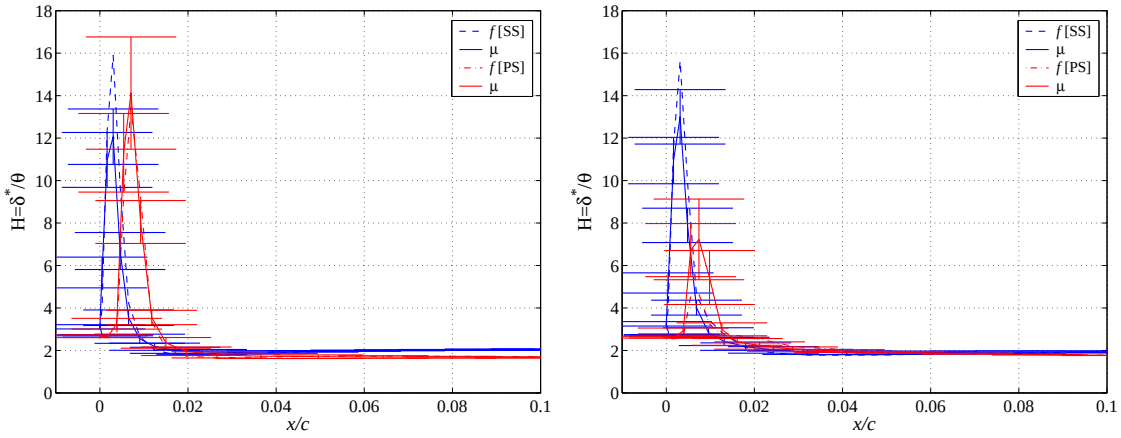

(a) MML: H (b) MSL: H

Figure 4-15: redesigned DFVLR airfoil: Shape parameter $H = \delta^*/\theta$

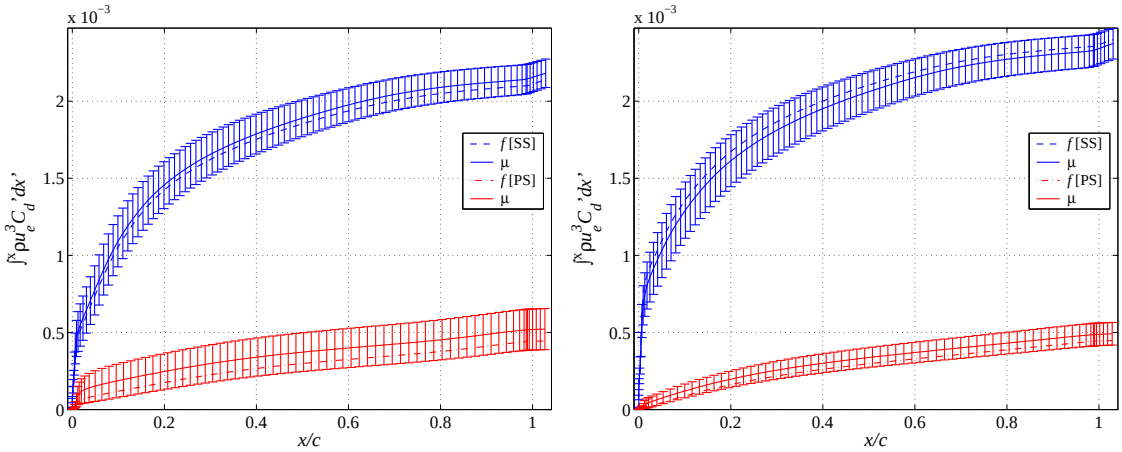

(a) MML (b) MSL

Figure 4-16: redesigned DFVLR airfoil: $\int_0^x \rho U_e^3 C d' dx'$

Table 4.4: Rotor 37 redesigned airfoil statistics (MCS $N = 2000$)

Design	ϖ^0	μ_ϖ	$\sigma_\varpi \times 10^3$	$\%V_\varpi$	ϑ^0	μ_ϑ	σ_ϑ	$\%V_\vartheta$
Baseline	0.0842	0.0857	9.64	11.2	14.68	14.74	0.481	3.26
DML	0.0593	0.0632	5.63	8.92	14.54	14.63	0.527	3.61
MML	0.0597	0.0631	5.64	8.94	14.52	14.60	0.510	3.49
MSL	0.0637	0.0667	4.78	7.17	14.56	14.61	0.562	3.84

design (or about 50% in standard deviation). The turning angle statistics are similar for the three redesigned airfoils, with nominal and mean values less than 0.2 degrees lower than baseline. All three redesigns satisfied the specified turning constraints. Figure 4-17 shows loss coefficient histograms of Monte Carlo results for the redesigned airfoils.

The effect of the nominal geometry redesign can also be seen in Fig. 4-18 which shows scatter plots of loss coefficient versus twist mode amplitude. Locations of mean loss coefficient and a 6σ interval about it are also shown. All three redesigns reduce the nominal value, mean and standard deviation of loss coefficient. The minimum-loss redesigns (DML, MML) have similar pressure distributions. The MSL airfoil produces a further reduction in loss coefficient scatter, in addition to reduced mean loss. The redesigned airfoils exhibit reductions in nominal and mean loss coefficient of 25 to 30% from the baseline design. For that reason further comparisons are made among the redesigned airfoils only.

Figure 4-19(a) shows the redesigned airfoil sections, with the vertical coordinate scaled up by a factor of ten. Figures 4-19(b) and (c) show plots of mean camber and thickness with respect to mean camber arc-length. Unlike the previous cases, the redesigned R37 airfoils have, in general, thinner cross sections than the baseline airfoil. Thinner leading-edges in the minimum-loss airfoils are to be expected as losses due to leading edge thickness t_{LE} have been shown to grow like $t_{\mathrm{LE}} M_1^2$, that is, with the square of the inlet Mach number [71]. The MML airfoil is somewhat thicker than the deterministic redesign, especially toward the rear of the blade. The MSL airfoil has more camber and a different thickness distribution than the other two redesigns.

In contrast to the subsonic-inlet cases discussed previously, for which viscous dissipation in the boundary layers and mixing of the wake were the main causes of loss, the dominant contribution to total pressure loss in the rotor 37 blade comes from entropy generation at the passage shock. Table 4.5 shows nominal and statistical values of viscous (subscript v) and wave (subscript w) contributions to the total loss coefficient. The nominal and mean values of the shock loss roughly twice as large as the viscous loss. The variability of the former, however, is roughly twice that of the latter. Although the relative reduction in variability (COV) is similar in both cases, the reduction in the shock loss variability dominates the reduction in overall loss uncertainty.

One mechanism that leads to reduced loss variability can be seen by considering the pressure distributions produced by the redesigned airfoils in Fig. 4-20. The DML and MML airfoils have relatively flat pressure distributions on the pressure side and constant expansion behind the passage shock, which impinges on the suction side at about mid-chord. The distinguishing characteristics of the MSL airfoil are a pressure plateau downstream of the shock on the suction side and the decompression at about 30% of the chord on the pressure side. The small pressure plateau behind the shock, caused by the local change in

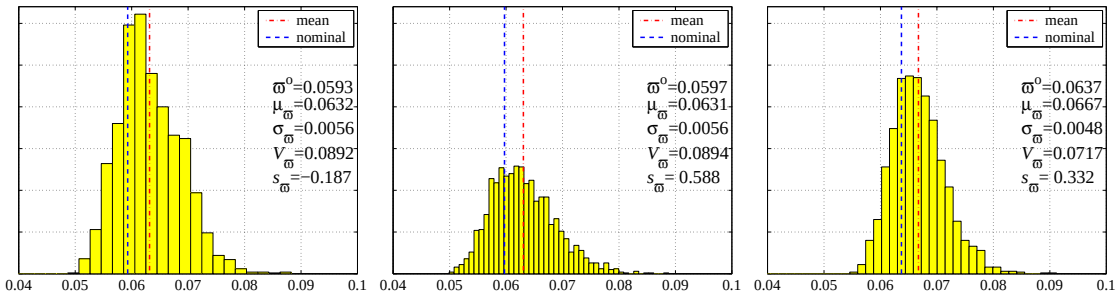

(a) DML (b) MML (c) MSL

Figure 4-17: Rotor 37 loss coefficient for redesigned airfoils

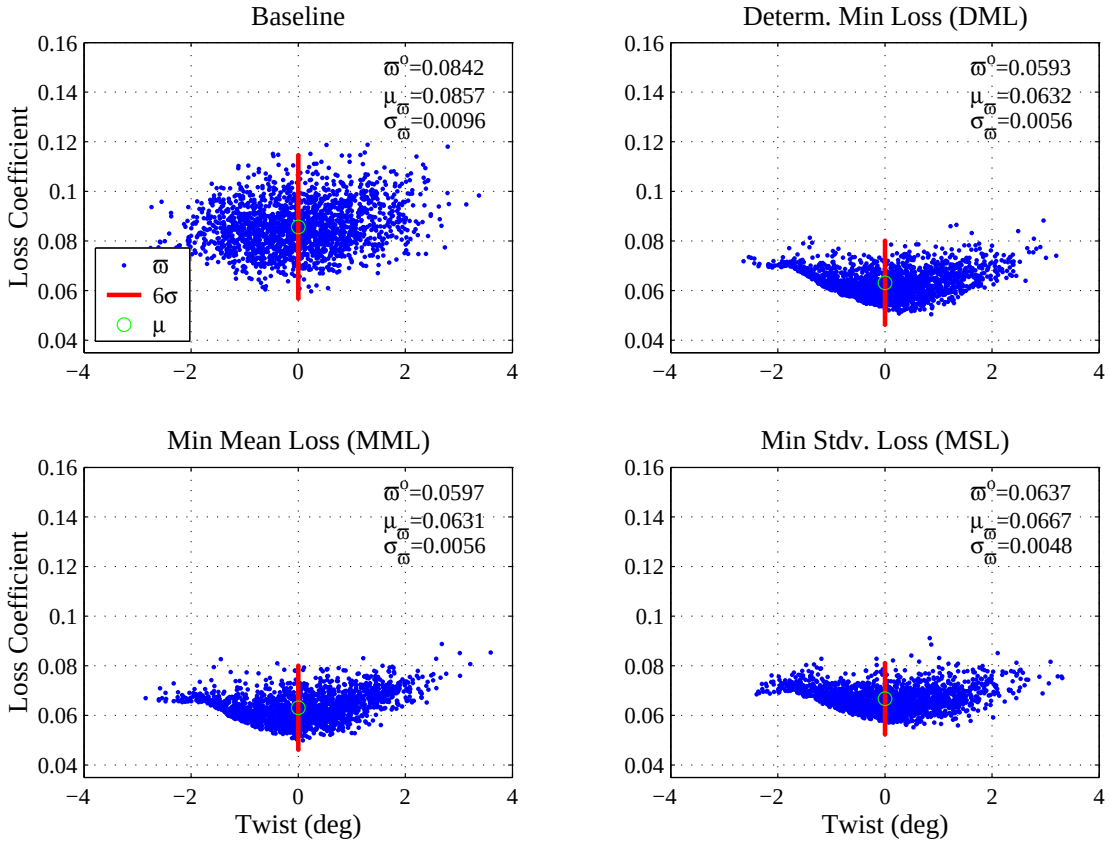

Figure 4-18: Rotor 37: Scatter of Loss coefficient vs. turning angle

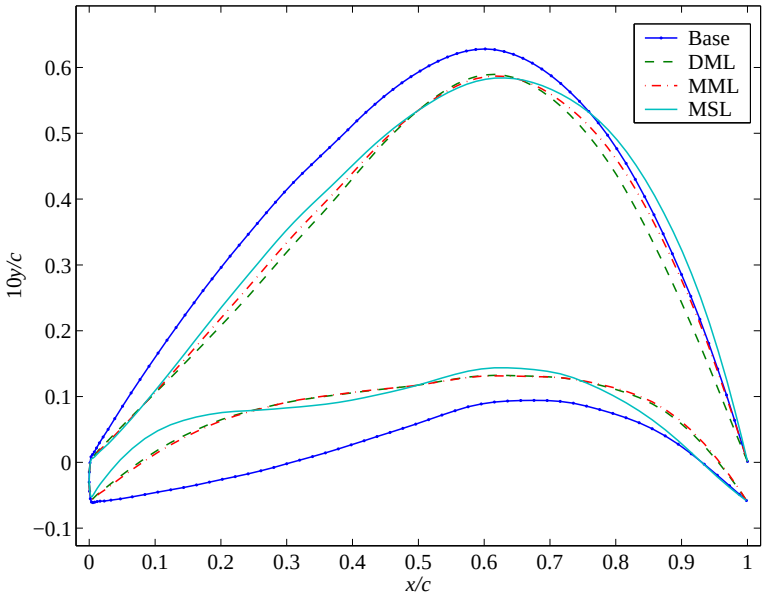

(a)

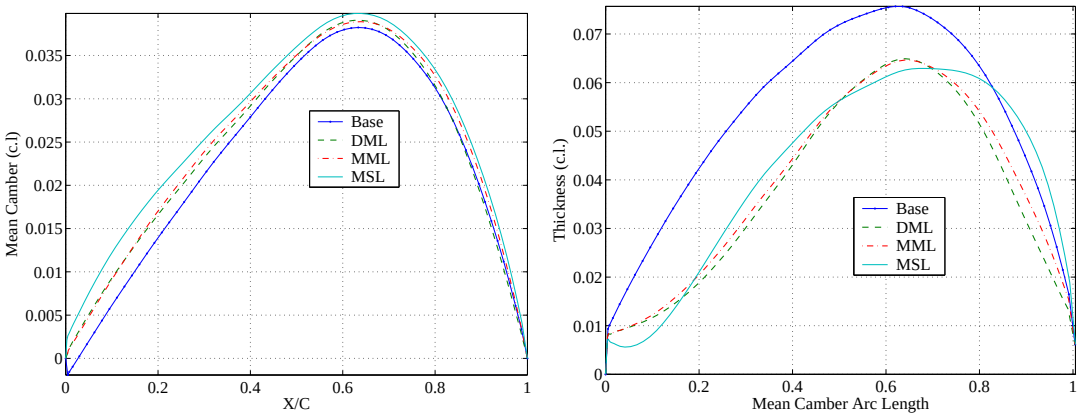

(b) (c)

Figure 4-19: Rotor 37: Redesigned nominal airfoil shape

Table 4.5: Viscous vs. shock loss for R37 redesigned blade

Design	ϖ_v^0	μ_{ϖ_v}	σ_{ϖ_v}	V_{ϖ_v}	ϖ_w^0	μ_{ϖ_w}	σ_{ϖ_w}	V_{ϖ_w}
Base	0.0195	0.0198	0.0025	12.6	0.0454	0.0465	0.0077	16.6
DML	0.0160	0.0164	0.0025	15.2	0.0271	0.0302	0.0058	19.2
MML	0.0167	0.0171	0.0026	15.2	0.0259	0.0287	0.0050	17.4
MSL	0.0162	0.0166	0.0018	10.8	0.0313	0.0337	0.0049	14.5

thickness distribution, lowers the sensitivity of the the shock impingement point to geometric variability, reducing in turn the likelihood of boundary layer separation.

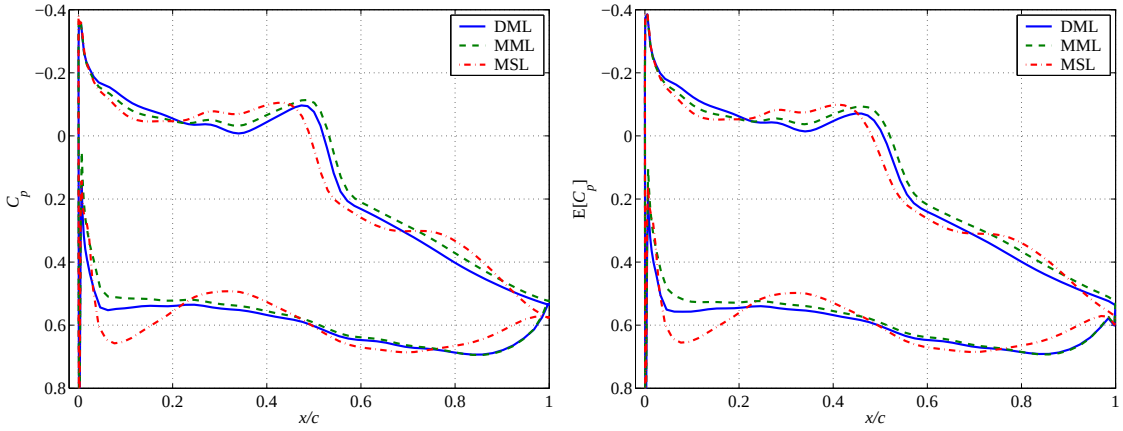

(a) C_p (b) $\mathbb{E}[Cp]$

Figure 4-20: Rotor 37: Pressure Coefficient

Figures 4-21(a) and (b) show mean and standard deviation values of the boundary layer shape parameter H on the suction side of the redesigned airfoils. The minimum-loss airfoils exhibit lower values of mean H until about 65% chord after which the trend reverses and the MSL airfoil shows as much as 30% lower mean H values. The variability of H, as illustrated in Fig. 4-21(b) by the standard deviation, is consistently lower for the MSL airfoil than for the DML and MML redesigns in the aft 40% of the suction side. At 80% chord the variability of H for the MSL airfoil is about 40% that of the DML or MML redesigns. Figure 4-21(c) shows plots of the standard deviation of $\rho u_e^3 C_d'$ on the suction side of the redesigned airfoils. The standard deviation of $\rho u_e^3 C_d'$ is consistently lower for the MSL airfoil (as much as 70%) on the aft 35% of the suction side. The accumulated effect of the reduced dissipation variability on the suction side of the MSL airfoil is illustrated in Fig.4-21(d) which shows standard deviation of the entropy generation rate. Initially (for $0 \leq x/c \leq 0.5$) the MML airfoil exhibits lower variability in the entropy generation rate, but in the aft 30% the DML and MML airfoils exhibit consistently higher variability than the MSL airfoil. At $x/c = 1$ the MSL redesign produces about 50% lower variability than the DML and MML airfoils.

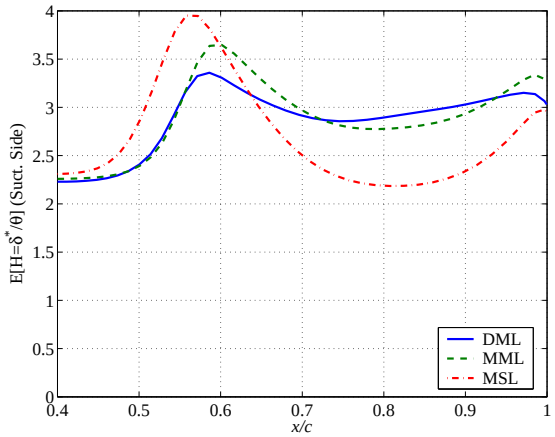

(a) Shape parameter

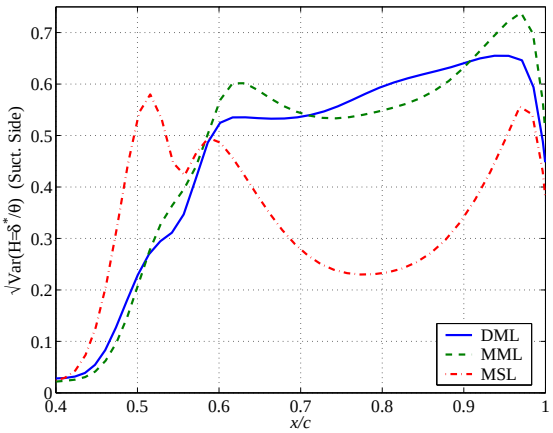

(b) Shape parameter std. dev.

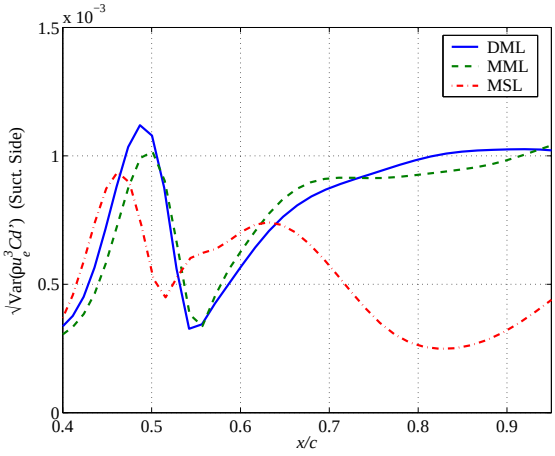

(c) Std. dev. of dissipation

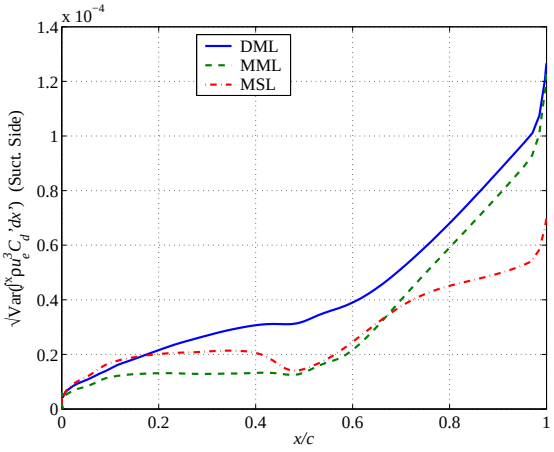

(d) Std. dev. of entropy gen. rate

Figure 4-21: Rotor 37: Suction side boundary layer

4.3 Summary

In this Chapter a probabilistic gradient-based approach to compressor blade optimization was presented. The probabilistic objectives, constraints and their corresponding gradients are approximated using low-fidelity Monte Carlo simulation. An external nonlinear optimization driver was used to drive the probabilistic simulations. Design modes included Chebyshev polynomials applied to the airfoil surface and solid-body rotation to optimize stagger angle.

Three test airfoils were optimized both deterministically and probabilistically and then subjected to simulated geometric variability to assess its impact on their performance. The deterministic redesign objective was to minimize loss coefficient subject to turning constraints. The probabilistic objectives were to minimize mean loss and loss variability respectively. In all probabilistically redesigned airfoils a mean turning constraint was satisfied.

The IBR airfoils was optimized at three geometric noise levels to explore possible redesign gains under different levels of uncertainty. At the baseline noise level the probabilistically redesigned airfoils exhibit lower loss coefficient variability than either baseline or deterministically redesigned airfoils. When optimizing for reduced variability the coefficient of variability of loss was reduced by 54% from the deterministic redesign and by 65% from the baseline airfoil; with 17% lower loss mean shift. In contrast, the minimum-variability redesign lead to 5% higher nominal and mean loss coefficient than the deterministic or probabilistic minimum-loss airfoils.

For $a = 2$ the minimum-variability redesign produced a 37% smaller loss coefficient of variability than the deterministic redesign. The reduction in variability from the deterministic minimum-loss to the minimum-variability redesigns was accompanied by an increase in mean loss coefficient of roughly 6%. At the more realistic $a = 5$ noise level the reduction in loss variability between the deterministic and minimum-variability redesigns was 30%, and the latter exhibits a 26% smaller loss mean shift.

In the DFVLR case, the deterministic redesign produced 17% lower nominal loss than the baseline airfoil, with a similar decrease in mean loss. However, the loss variability for the deterministically redesigned blade was 14% higher the baseline design. The loss coefficient variability of the probabilistic minimum-loss redesign was 32% lower than the deterministic redesign.

For the IBR and DFVLR airfoils with subsonic inlet relative Mach numbers, viscous dissipation dominated the generation of entropy. It was found that a decrease in the rate of diffusion on the entry region of the pressure side reduced the entropy generation variability by lowering the likelihood of separation in the presence of geometric variability. This mechanism was noticed at the three noise levels.

For the Rotor 37 mid-span section, the deterministic and probabilistic minimum-loss redesigns produced a reduction in nominal and mean loss coefficient of nearly 30% from the baseline airfoil. The minimum-variability redesign resulted in a sizable reduction of loss coefficient variability: 20% smaller coefficient of variability than the deterministically redesigned airfoil (36% from baseline). The statistics for turning performance are similar for the three redesigned airfoils, with nominal and mean values less than 0.2 degrees lower than baseline. The three redesigns satisfy-ed the specified turning constraints. For this case, shock losses were found to be considerably larger than viscous losses. A decrease in the rate of flow deceleration immediately downstream of the shock impingement point on

the suction side helped reduce the loss variability due to shock-boundary layer interactions exacerbated by geometric variability.

Chapter 5

Effect of Geometric Variability on Overall Compressor Performance

In this chapter, a mean-line multi-stage axial compressor model is used to estimate the impact of geometric variability on overall compressor performance. Probabilistic models of loss coefficient and turning angle are constructed from the aerodynamic performance of the IBR blade discussed in previous chapters. The loss and turning models were used in probabilistic mean-line calculations for various redesigned airfoils at three noise amplitude levels: original, double and five-fold, the latter representing more realistic geometric levels. At the baseline noise level the impact on compressor polytropic efficiency is small, causing a 0.2% mean-shift and 0.04% coefficient of variability. Loss models using probabilistically redesigned airfoils for minimum loss variability cause a decrease of 46% in standard deviation of polytropic efficiency compared to a compressor model using deterministically redesigned airfoils.

At a more realistic geometric noise level (five times the original), the drop from nominal to mean efficiency is more than one percentage point, with an increase in efficiency variability to 30%. In contrast, a compressor using minimum-variability loss blades exhibited a 42% reduction in the discrepancy between mean and nominal polytropic efficiency as well as 34% reduction in variability compared to the baseline airfoil. Compressors using minimum-variability airfoils exhibited reductions in mean-shift and variability of 30 and 26% respectively compared to compressors using deterministically optimized airfoils. In contrast to single blade results, polytropic efficiency and pressure ratio variability were found to be 30 and 70% lower, respectively, for multiple-blade compressor models.

Pressure ratio variability is found to increase linearly with the amount of geometric variability. Rotor and stator incidence variability is found to decrease with distance through the compressor. For the same canonical airfoil design, mean stage exit Mach number increases with noise amplitude as does its variability. As with incidence, the Mach number variability decreases with each successive stage.

5.1 Mean-Line Compressor Model

A simple compressor stage mean-line model, in which rotors and stators are described separately, was obtained as follows. Given rotor total pressure loss coefficient, ϕ_r, flow turning ϑ_r, outlet area and upstream total temperature, relative total pressure and Mach

number, and inlet flow angle, the rotor outlet state is described by the nonlinear system (see Appendix D for an explanation of the nomenclature)

$$F := \Delta T_T - \frac{\omega}{c_p}(r_2 V_2 \sin\alpha_2 - r_1 V_1 \sin\alpha_1) \qquad = 0 \tag{5.1}$$

$$G := \frac{\dot{m}\sqrt{T_{T_2}}}{P_{T_2} A_2 \cos\alpha_2} - \sqrt{\frac{\gamma}{R}} \frac{M_2}{\left(1 + \frac{\gamma-1}{2} M_2^2\right)^{\frac{\gamma+1}{2(\gamma-1)}}} = 0 \tag{5.2}$$

$$H := V_2 \left[\sin\alpha_2 + \cos\alpha_2 \tan(\beta_1 - \vartheta_r)\right] - \omega r_2 \quad = 0 \tag{5.3}$$

where

$$T_{T_2}(\Delta T_T) := T_{T_1} + \Delta T_T$$

$$V_2(\Delta T_T, M_2) := M_2 \left(\frac{\gamma R T_{T_2}}{1 + \frac{\gamma-1}{2} M_2^2}\right)^{\frac{1}{2}}$$

$$P_{T_2}(\Delta T_T) := P_{T_{1R}} \left[1 - \phi_r \frac{\frac{1}{2}\gamma M_{1R}^2}{(1 + \frac{\gamma-1}{2} M_{1R}^2)^{\frac{\gamma}{\gamma-1}}}\right] \left(\frac{T_{T_2}}{T_{T_{1R}}}\right)^{\frac{\gamma}{\gamma-1}}$$

Equations (5.1)–(5.3) form a nonlinear system in the variables ΔT_T, M_2 and α_2, which can be readily solved numerically using, for instance, a Newton-Raphson solver.

Equation (5.1) is a restatement of the Euler turbine equation for calorically perfect gases, namely

$$c_p(T_{T_2} - T_{T_1}) = \omega(r_2 v_2 - r_1 v_1),$$

which relates the change in total enthalpy to the change in angular momentum of a stream tube across a rotor. Using the definition of the total pressure loss coefficient [1],

$$\phi \equiv \frac{P_{T_1} - P_{T_2}}{\frac{1}{2}\rho_1 V_1^2} \ ,$$

the rotor relative total pressure ratio may be rewritten in terms of inlet relative Mach number and pressure coefficient in the form [81]

$$\frac{P_{T_{2R}}}{P_{T_{1R}}} = 1 - \phi_r \frac{\rho_1 V_{1R}^2}{2 P_{T_{1R}}} = 1 - \phi_r \frac{\gamma P_1 M_{1R}^2}{2 P_{T_{1R}}} = 1 - \phi_r \frac{\gamma M_{1R}^2}{(1 + \frac{\gamma-1}{2} M_{1R}^2)^{\gamma/(\gamma-1)}}.$$

Equation (5.2) follows from Fligner's formula (or *mass flow parameter* [81]) for quasi-one-dimensional flow of a calorically perfect gas,

$$\frac{\dot{m}\sqrt{T_T}}{A P_T} = \sqrt{\frac{\gamma}{R}} \frac{M}{\left(1 + \frac{\gamma-1}{2} M^2\right)^{\frac{\gamma+1}{2(\gamma-1)}}} \ .$$

Equation (5.3) states how the absolute and relative tangential velocities are related through the wheel speed (velocity triangles). Expressions for for the derivatives of F, G

[1] The loss coefficient definition used here, which differs from that of ϖ used in the previous chapters, is more meaningful in the present context.

and H with respect to ΔT_T, M_2 and α_2,—which are used in a gradient-based algorithm to solve the nonlinear system—are included in Appendix D.

After solving the rotor equations and using the rotor outlet state to initialize the stator inlet, the stator exit Mach number is found from Fligner's formula,

$$\frac{\dot{m}\sqrt{T_{T_3}}}{f(M_3)P_{T_3}\cos\alpha_3} - A_3 = 0, \tag{5.4}$$

where

$$f(M) = \sqrt{\frac{\gamma}{R}}\frac{M}{\left(1+\frac{\gamma-1}{2}M^2\right)^{\frac{\gamma+1}{2(\gamma-1)}}} .$$

As with the rotor, the stator total pressure ratio may be written in terms of loss coefficient and the upstream flow conditions,

$$\frac{P_{T_3}}{P_{T_2}} = 1 - \phi_s\frac{\gamma M_2^2/2}{(1+\frac{\gamma-1}{2}M_2^2)^{\gamma/(\gamma-1)}} .$$

The calculation is marched through the compressor using the previous stage's exit conditions to calculate the next inlet state for fixed flow annulus area, i.e., $T_{T_1}^{k+1} \leftarrow T_{T_3}^{k}$, $P_{T_1}^{k+1} \leftarrow P_{T_3}^{k}$, $M_1^{k+1} \leftarrow M_3^{k}$, where the superscript indicates stage number.

The deterministic mean-line model is used as part of a probabilistic simulation by prescribing models of loss coefficient and turning angle variability for each blade row. These loss and turning models are described in the next section.

The current method estimates only the impact of blade profile variability caused by geometric noise on compressor performance. Endwall effects and radial imbalances are not included. It follows that the results discussed below likely underestimate actual compressors performance variability in the presence of geometric uncertainty.

5.2 Loss Coefficient and Turning Angle Models

In a mean-line sense, the effect of geometric and operating condition variability occurring upstream of a given compressor stage translates to changes in axial Mach number, total pressure and total temperature at the rotor inlet. These augment the performance variability caused by geometric noise in the rotor blades. The statistical impact of geometric variability can therefore be modeled by considering changes in loss and turning statistics based on inlet flow conditions, i.e., inlet flow angle and axial Mach number.

Conceptually, the loss coefficient and turning obtained from quasi-2D blade passage analyses may be taken to be deterministic functions of various geometric and flow parameters such as inlet flow angle, inlet Mach number, etc. In particular, for fixed nominal geometry $\mathbf{x}^0$, let

$$\phi = \phi(\alpha, \mathbf{x}), \quad \text{and} \quad \vartheta = \vartheta(\alpha, \mathbf{x})$$

where α is inlet flow incidence, and $\mathbf{x}$ is a vector of parameters describing amplitudes of geometric noise modes such as those described in Chapter 2 (e.g., PCA modes, thickness, twist, leading-edge bluntness, etc). In the present application, "incidence" refers to the difference between nominal inlet flow angle (here the minimum-loss angle) and actual incoming flow

angle [2]. Other geometric and flow parameters are assumed to be fixed and their functional dependence not explicitly considered.

To proceed, it ϕ and ϑ are written in the form

$$\phi(\alpha, \mathbf{x}) = \phi_0(\alpha) + \Delta\phi(\alpha, \mathbf{x}), \tag{5.5}$$
$$\vartheta(\alpha, \mathbf{x}) = \vartheta_0(\alpha) + \Delta\vartheta(\alpha, \mathbf{x}), \tag{5.6}$$

where $\phi_0(\alpha)$ and $\vartheta_0(\alpha)$ are deterministic components of loss and turning depending on incidence alone.

Next, instead of a deterministic geometric argument, an independent random vector X is considered. For fixed α, $\Delta\phi(\alpha, X)$, let

$$\Delta\mu_\phi(\alpha) := \mathop{\mathbb{E}}_X[\Delta\phi(\alpha, X)], \qquad \sigma^2_\phi(\alpha) := \mathop{\mathrm{Var}}_X(\Delta\phi(\alpha, X)),$$
$$\Delta\mu_\vartheta(\alpha) := \mathop{\mathbb{E}}_X[\Delta\vartheta(\alpha, X)], \qquad \sigma^2_\vartheta(\alpha) := \mathop{\mathrm{Var}}_X(\Delta\vartheta(\alpha, X)).$$

In general $\Delta\mu_\phi(\alpha)$, $\sigma^2_\phi(\alpha)$, $\Delta\mu_X(\alpha)$, and $\sigma^2_X(\alpha)$ cannot be written in closed form. Instead, let $\Delta\hat{\mu}_\phi(\alpha)$, $\hat{\sigma}^2_\phi(\alpha)$, $\Delta\hat{\mu}_\vartheta(\alpha)$ and $\hat{\sigma}^2_\vartheta(\alpha)$ be models of loss "mean shift" (i.e., the difference between $\phi_0(\alpha)$ and $\mathbb{E}_X[\Delta\phi(\alpha, X)]$ for a given α) and variance, and turning mean shift and variance, respectively. Then

$$\mathop{\mathbb{E}}_X[\phi(\alpha, X)] = \mathop{\mathbb{E}}_X[\phi_0(\alpha) + \Delta\phi(\alpha, X)] \simeq \phi_0(\alpha) + \Delta\hat{\mu}(\alpha),$$
$$\mathop{\mathbb{E}}_X[\phi(\alpha, X)] = \mathop{\mathbb{E}}_X[\phi_0(\alpha) + \Delta\phi(\alpha, X)] \simeq \phi_0(\alpha) + \Delta\hat{\mu}(\alpha),$$

and

$$\mathop{\mathrm{Var}}_X(\phi(\alpha, X)) = \mathop{\mathbb{E}}_X[(\Delta\phi(\alpha, X) - \Delta\mu_\phi(\alpha, X))^2] \simeq \hat{\sigma}^2_\phi(\alpha),$$
$$\mathop{\mathrm{Var}}_X(\vartheta(\alpha, X)) = \mathop{\mathbb{E}}_X[(\Delta\vartheta(\alpha, X) - \Delta\mu_\vartheta(\alpha, X))^2] \simeq \hat{\sigma}^2_\vartheta(\alpha).$$

To proceed it is assumed that, for fixed incidence α, $\Delta\phi(\alpha, X)$ and $\Delta\vartheta(\alpha, X)$ are normally distributed, that is,

$$\Delta\phi(\alpha, X) \in \mathcal{N}(\Delta\hat{\mu}_\phi(\alpha), \hat{\sigma}^2_\phi(\alpha)), \quad \text{and} \quad \Delta\vartheta(\alpha, X) \in \mathcal{N}(\Delta\hat{\mu}_\vartheta(\alpha), \hat{\sigma}^2_\vartheta(\alpha)).$$

Although the Monte Carlo simulation results reported in Chapter 3 show loss distributions that are not always normal (indeed not always symmetric), the assumption of normality is made here for the sake of model simplicity and in lieu of a general description of loss and turning distribution. Models $\Delta\hat{\mu}_\phi(\alpha)$, $\hat{\sigma}^2_\phi(\alpha)$, $\Delta\hat{\mu}_\vartheta(\alpha)$, and $\hat{\sigma}^2_\vartheta(\alpha)$ are obtained from computed statistics of loss and turning at fixed values of incidence for single blade passages. The statistics are computed via Monte Carlo simulation, as described in Chapter 3, for discrete values of incidence in the range of adequate numerical convergence.

Figure 5-1 shows loss coefficient and turning angle results from MISES Monte Carlo simulations of the IBR blade. The geometric noise assumed in the simulations was the PCA-based model from Chapter 2, with noise amplitude $a = 2$. The output statistics

[2]The present definition of incidence, though more appropriate in the current context, is in contrast with the more common one involving the difference between inlet flow angle and airfoil inlet camber angle.

were computed for each fixed value of α via Monte Carlo simulation ($N = 2000$). Similar computations were also carried out for $a = 1$ and $a = 5$ noise levels. In Fig. 5-1 the solid line

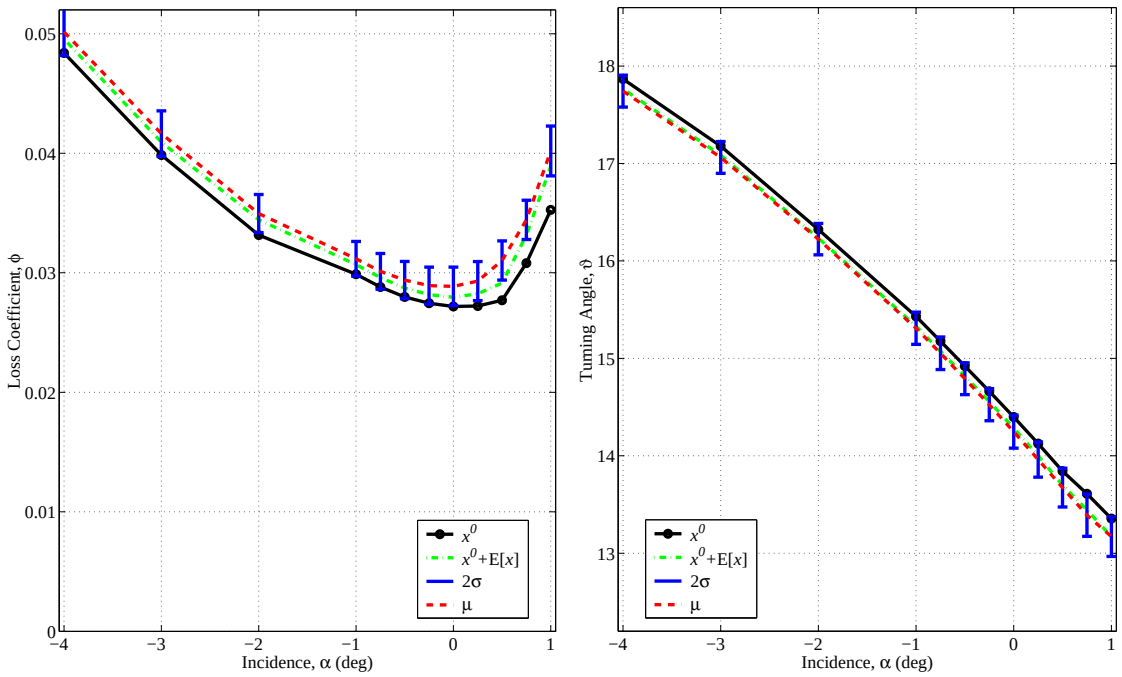

(a) Loss Coefficient

(b) Turning

Figure 5-1: IBR: Loss coefficient and turning angle vs. incidence, $a = 2$

connects the computed nominal (i.e., in the absence of geometric noise) loss coefficient and turning; the dash-dot line connects the values computed for the average-geometry airfoil; the dashed line indicates the mean values of the Monte Carlo trials and the error bars show their two-standard-deviation intervals centered at the mean.

The loss coefficient plot (Fig. 5-1(a)) shows a typical "loss bucket" shape with minimum nominal loss approximately located at zero incidence. The loss coefficient increases more steeply for positive values of incidence. No points are plotted for $\alpha > 1$ degree where numerical convergence of the Monte Carlo simulations was deficient (less than 80% convergence rate). As noted in Chapter 3, for the depicted $a = 2$ case the average geometry loss coefficient at zero-incidence lies approximately half-way between the nominal and mean values, indicating that half or more of the mean-shift is due to the geometric scatter. On the other hand, for $|\alpha| > 0.75$ the geometric variability contributes more to the mean-shift than does the average geometry. The mean-shift is largest for values of incidence above -0.5, with a maximum of 0.004 at $\alpha = 1$. The trend is similar for the turning mean-shift, with more negative mean-shift values corresponding to positive incidence.

The standard deviation of loss coefficient has a minimum of 0.6×10^{-3} at the zero-incidence condition. It increases from there for both positive and negative values of α; at $\alpha = -3$, $\sigma_{\varpi} \simeq 1.7 \times 10^{-3}$ while $\sigma_{\varpi} \simeq 1.5 \times 10^{-3}$ for $\alpha = 1$. Standard deviation of turning is roughly constant at 0.16° for non-positive values of incidence, increasing to 0.23° at $\alpha = 1$.

In addition to the baseline design, Figs. 5-2 and 5-3 show loss coefficient and turning

angle plots for the deterministic redesign (DML) and the two probabilistic redesigns (DML, MSL) introduced and discussed in the previous chapter; all for noise amplitude $a = 5$. As with the $a = 2$ case, the nominal loss coefficient for the baseline design is smallest near zero-incidence and increases more rapidly for positive incidence values. The characteristics of the redesigned airfoils at zero incidence, which were discussed in the previous chapter, are emphasized in Fig. 5-2: The DML redesign has the lowest nominal loss value, but the lowest mean loss corresponds to the probabilistic MSL redesign; the loss coefficient variability is lowest for the MSL design. In addition, Fig. 5-2 presents off-design aerodynamic performance information for the redesigned airfoils. The propensity of the deterministically redesigned airfoil to exhibit larger loss variability extends to values of incidence away from zero, and worsens for positive incidence. The MSL design shows a less pronounced rate of change away from $\alpha = 0$, i.e., a flatter loss trough. A comparison of Figs. 5-2(c) and (d) highlights the increased mean and nominal loss coefficient of the MSL redesign, as well as its reduced variability. The average geometry for the baseline design contributes comparatively little to the overall loss variability. However, at positive incidence the average geometry contributes nearly one-fourth of the DML airfoil mean-shift.

The computed output statistics for discrete values of α were used to construct the continuous loss and turning models which, in turn, were utilized in the probabilistic mean-line compressor simulations reported below. The computed data points were used to construct piecewise-cubic interpolating splines with zero-second-derivative end conditions [22]. To avoid difficulties with extrapolation outside the incidence range for which computed data points were available, additional points were added at higher positive incidence by linearly extrapolating the nominal loss and turning and replicating the mean-shift and variance values corresponding to the highest computed α (e.g., 1 or 1.5). [3] Separate models were constructed for each geometric noise amplitude considered, as well as for each redesigned nominal geometry.

5.3 Probabilistic Mean-Line Calculations

In this section, mean-line and probabilistic loss and turning models are used to estimate the impact of geometric variability on the overall performance of an axial compressor. A six-stage compressor with a base-line total pressure ratio of 11 is considered first. Next follows a comparison of compressors using deterministically and probabilistically optimized airfoils. Performance variability trends with geometric noise amplitude are discussed next. Lastly, the effect on performance statistics when considering multiple blades per row is discussed.

5.3.1 Six-stage compressor model: baseline airfoil

A baseline compressor model with nominal pressure ratio of 11 was constructed according to the procedure outlined in Appendix D. The nominal rotor and stator loss coefficients were $\phi_r = \phi_s = 0.03$ and the nominal rotor turning was $\vartheta_r = 14.4$ degrees. The resulting compressor total pressure ratio and polytropic efficiency were $\pi = 10.8$ and $e = 0.96$ respectively.

The probabilistic simulations involve solving nonlinear stage equations (5.1)–(5.3) and (5.4), for prescribed fixed flow annulus areas and mean-line radii. The compressor inlet

[3] This approach errs on the low side of loss and turning variability, which in turn may under-predict compressor performance effects.

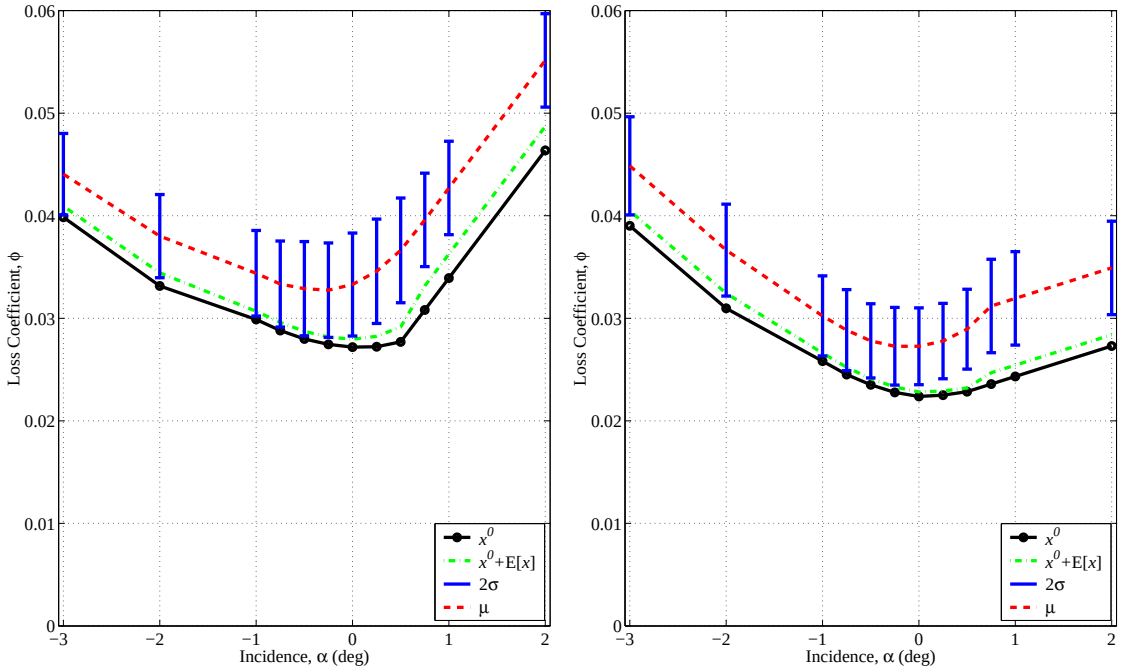

(a) Baseline

(b) DML

(c) MML

(d) MSL

Figure 5-2: IBR mid-span section: Loss coefficient vs. incidence, $a = 5$. (Linear extrapolation for $\alpha > 0.75$.)

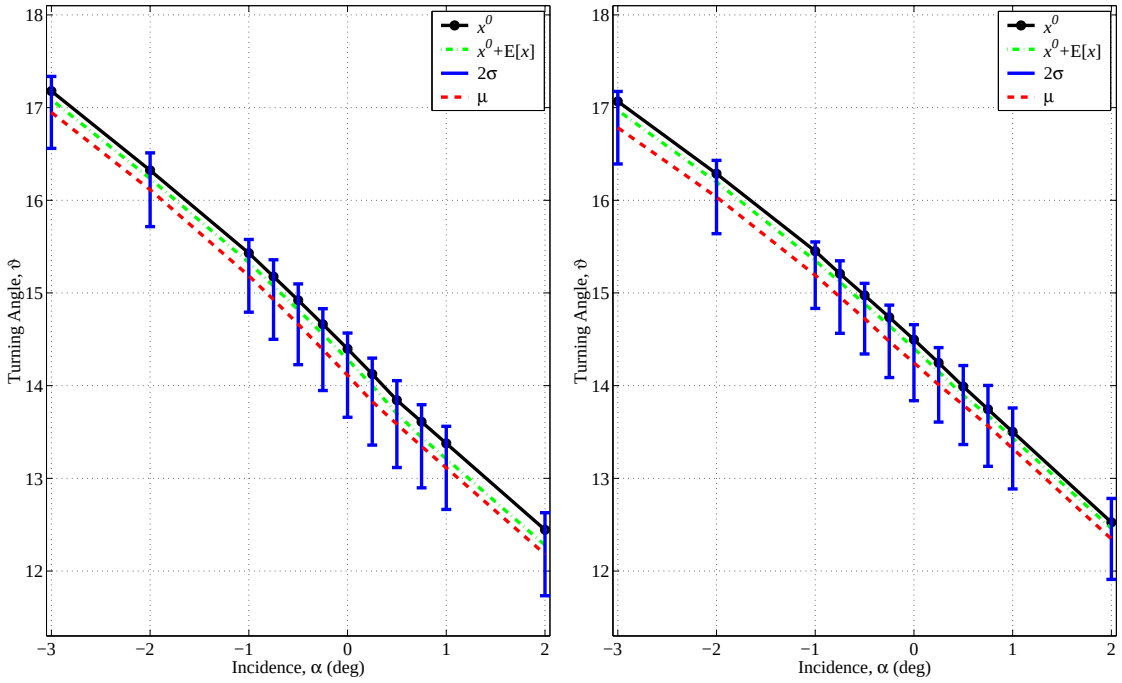

(a) Baseline

(b) DML

(c) MML

(d) MSL

Figure 5-3: IBR mid-span section: Turning angle vs. incidence, $a = 5$. (Linear extrapolation for $\alpha > 0.75$.)

conditions are assumed to be the same for each simulation (see Appendix D). The rotor and stator turning angle and loss coefficient values are obtained from the IBR blade models discussed in the previous section. The nonlinear equations for each stage are solved using the Newton-Raphson method implemented in MATLAB's Optimization Toolkit. [4] The procedure is repeated for each stage sequentially to march through the compressor.

Upstream operating condition variability leads to variations in rotor inlet flow angle (incidence) and axial Mach number, as well as in total temperature and pressure variability. The later variabilities follow directly from upstream loss coefficient and turning perturbations respectively. Since the annulus flow areas remain fixed, inlet total pressure and temperature fluctuations translate, for a given mass flow rate, into axial Mach number and incidence perturbations. Inlet flow condition variability is compounded by rotor and stator loss and turning noise to produce variability in the stage exit conditions, which in turn affect the following (downstream) stage.

The stator nominal loss and turning, as well as their mean shift and standard deviation were taken from the IBR incidence models discussed above. The impact of geometric variability on row performance can be expected to vary as nominal airfoil shapes change from stage to stage. In the current calculations the same loss and turning models were used for each blade row, as the intent is to illustrate the approach. In practical design situations, where blade shapes for each rotor and stator are available, loss and turning models could be readily generated for each separate blade row.

Commonly, stators are required to produce considerably higher flow turning than rotors, e.g., in the present six-stage model $\vartheta_s =\sim 35^\circ$, more than twice the rotor turning (see Table D.4 in Appendix D). Therefore it can be expected that the stator passages will exhibit higher exit flow variability (e.g., more flow deflection) than the rotor passages. As a conservative estimate the same loss coefficient nominal, mean-shift and variance models—as functions of incidence—were used for the stator as for the rotor. Similarly, the same mean-shift model for the rotor was used in the probabilistic stator calculation, but with the nominal turning being fixed (i.e., not varying with incidence). The stator turning variability model was obtained by scaling the rotor model to the stator nominal turning—effectively using the same COV-versus-incidence model as for the rotor.

Figure 5-4 shows polytropic efficiency and pressure ratio histograms of Monte Carlo simulation results ($N = 2000$ trials) for the baseline noise level. The histograms show a 0.2% drop from nominal polytropic efficiency to the expected value, and a 0.6% decrease in total pressure ratio. As discussed in Chapter 3, at this noise level the primary contribution to performance comes from the average geometry rather than from the geometric variability (cf. Figs. 3-5 and 3-6). The impact of increased noise level is reported in sub-section 5.4 below.

The geometric variability present in the IBR coordinate measurements is quite small (cf. Chapter 3), due to the highly controlled manufacturing processes employed (i.e., flank milling). The "small" geometric noise in the measurements translates into small loss and turning variability, which in turn results in small compressor performance uncertainty: the polytropic efficiency COV (ratio of standard deviation to mean) is only 0.04%, and the pressure ratio COV is 0.2%.

[4] The Mathworks, Inc., Natick, MA, `http://www.mathworks.com`

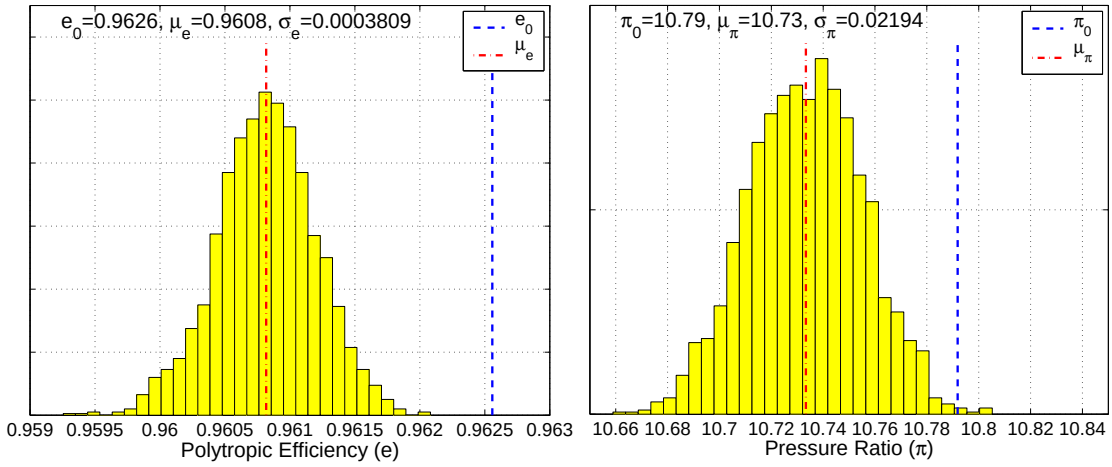

(a) Polytropic efficiency

(b) Pressure ratio

Figure 5-4: Monte Carlo results of Mean-line compressor model: IBR airfoils ($a = 1$)

5.3.2 Six-stage compressor model: redesigned airfoils

Figure 5-5 depicts the differences in compressor efficiency and pressure ratio statistics associated with the various redesigned airfoils reported in the previous chapter, for baseline geometric noise level. Despite the small compressor performance variability predicted by the mean-line analysis, the redesigned airfoils lead to differences in performance at the overall compressor level. The deterministic DML and probabilistic MML blade redesigns lead to similar mean efficiency and standard deviation: about 0.7% better nominal and mean efficiency, and 3% higher pressure ratio. In contrast, the probabilistic MSL redesign, with similar mean efficiency and pressure ratio as the minimum-loss redesigns, results in a decrease of 62% in standard deviation from the compressor model based on the baseline airfoil, and 46% when compared with the DML-based model. The enforcement of turning angle constraints at the airfoil level led to redesigned airfoils with similar mean and standard deviation values for pressure ratio.

5.4 Impact of Geometric Noise on Compressor Performance

Presumably, as blade geometric variability increases so does its impact on compressor performance. This section attempts to quantify that trend within the limitations of the current mean-line model. Table 5.1 summarizes the polytropic efficiency and overall pressure ratio statistics for the three noise variability levels: $a = 1$, 2 and 5. The loss and turning-versus-incidence models for the $a = 5$ noise level were discussed in Section 5.2. In addition to the baseline design, loss and turning models for the deterministically and probabilistically redesigned airfoils were considered.

For $a = 2$, the mean-shift in polytropic efficiency is about 0.4% for the baseline airfoil and no more than 0.2% for the compressor models based on the redesigned airfoils. Similarly, mean pressure ratio differs by no more than 0.7% from the nominal values. On the other hand, the standard deviation of polytropic efficiency for the baseline design increases by

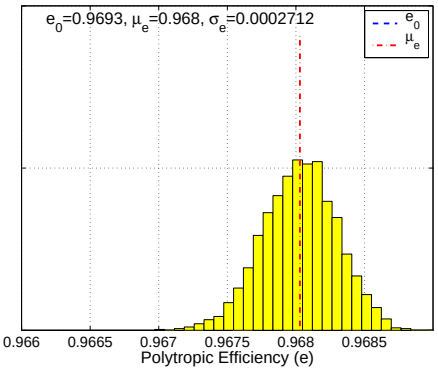

(a) DML: Polytropic efficiency

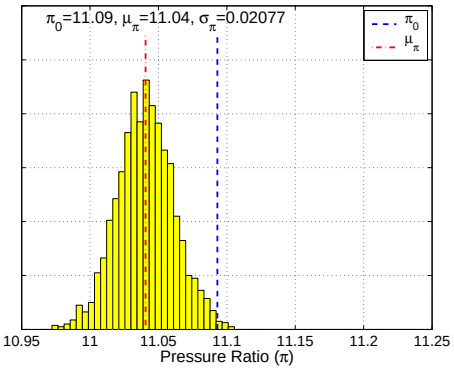

(b) DML: Pressure ratio

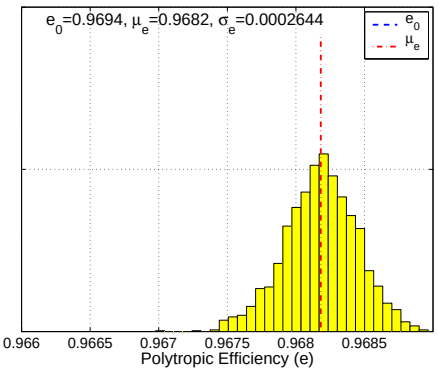

(c) MML: Polytropic efficiency

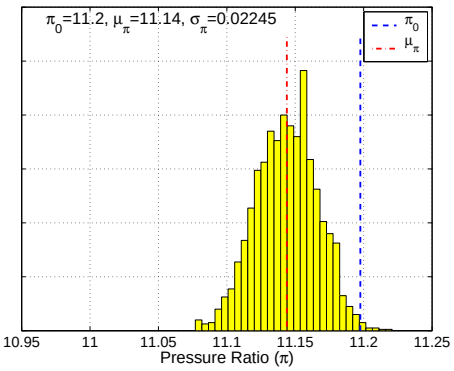

(d) MML: Pressure ratio

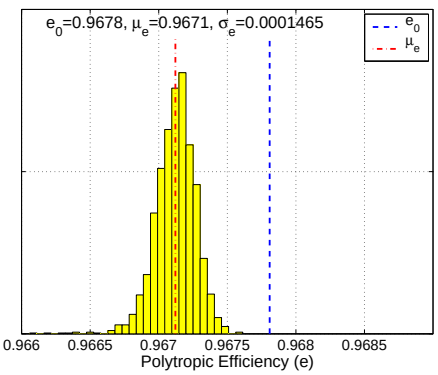

(e) MSL: Polytropic efficiency

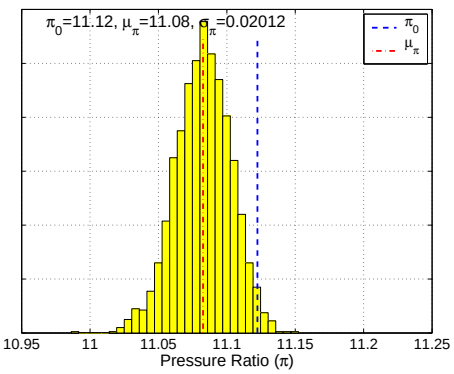

(f) MSL: Pressure ratio

Figure 5-5: Probabilistic mean-line results with redesigned airfoils ($a = 1$)

Table 5.1: Six-stage compressor, IBR airfoil-based loss and turning models

a	Design	e^0	μ_e	$\sigma_e \times 10^3$	π^0	μ_π	σ_π
1	Base	0.963	0.961	0.038	10.79	10.73	0.022
	DML	0.969	0.968	0.027	11.09	11.04	0.021
	MML	0.969	0.968	0.026	11.20	11.14	0.023
	MSL	0.968	0.967	0.015	11.12	11.08	0.020
2	Base	0.963	0.959	0.083	10.79	10.71	0.043
	DML	0.969	0.967	0.059	11.09	11.02	0.041
	MML	0.969	0.967	0.060	11.18	11.11	0.044
	MSL	0.967	0.966	0.047	11.13	11.08	0.041
5	Base	0.963	0.951	0.275	10.79	10.59	0.111
	DML	0.969	0.959	0.244	11.09	10.89	0.114
	MML	0.969	0.960	0.218	11.30	11.11	0.115
	MSL	0.967	0.960	0.181	11.20	11.05	0.107

more than a factor of two when compared with its $a = 1$ counterpart. A similar increase rate is seen in pressure ratio variability. When comparing efficiency for the DML and MSL redesigns, the latter shows a decrease of 21% in standard deviation from the former, in keeping with what was observed for $a = 1$. The pressure ratio COV decreases by about 8% when comparing the baseline design to the MSL redesign.

At the more realistic $a = 5$ noise level (see Appendix B), the efficiency COV for the baseline airfoil-based compressor model has risen to 30%, roughly a seven-fold increase from the $a = 1$ case. At this level of noise, the mean-shifts in polytropic efficiency also become noticeable: ∼1.2% drop for the baseline case, but only 0.7% for the MSL redesign (i.e., a 42% reduction in mean-shift from baseline and 30% from DML). At the higher noise level the decrease in efficiency uncertainty for the MSL-based compressor model is less drastic but still important: 34% from the baseline airfoil and 26% from the DML airfoil-based compressor. The pressure ratio variability does not change significantly among the redesigned airfoils, staying below 1%; the MSL pressure ratio COV is roughly 8% lower than the corresponding baseline and DML values. The impact of geometric noise amplitude on pressure ratio variability is nearly linear with noise level, i.e., the baseline pressure ratio COV for $a = 2$ is roughly twice as large as that of the $a = 1$ case, and similarly the COV for $a = 5$ is nearly five times higher. This agrees with the linear increase in turning variability with respect to noise amplitude observed in Chapter 3. Lastly, the MSL pressure ratio mean-shift is 25% lower than the corresponding baseline and DML values.

Figure 5-6 shows error-bar plots of rotor and stator inlet incidence variability at each stage of the compressor model. Plots for geometric noise levels $a = 1$ and 2 are shown. The symbols indicate the location of the average value while the error bars show a 6σ interval centered at the mean. In all cases mean incidence is negative, indicating that, in average, each stator and each rotor other than the first operate off-design. At the higher noise level the reduction of rotor incidence variability due to the probabilistic airfoil redesign becomes apparent, as is the less pronounced off-design average incidence. The second stage rotor and stator exhibit the highest level of variability compared to the other stages; in fact incidence variability decreases for each successive downstream stage.

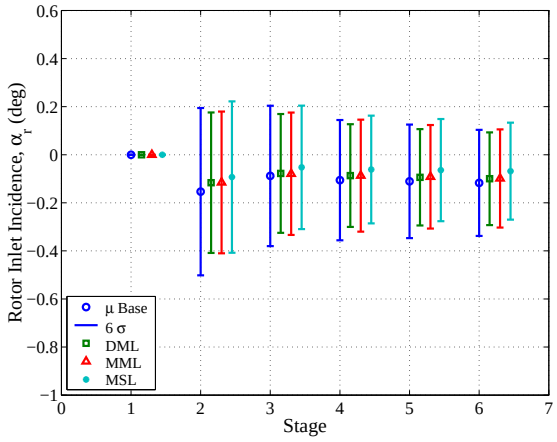

(a) $a = 1$: Rotor incidence

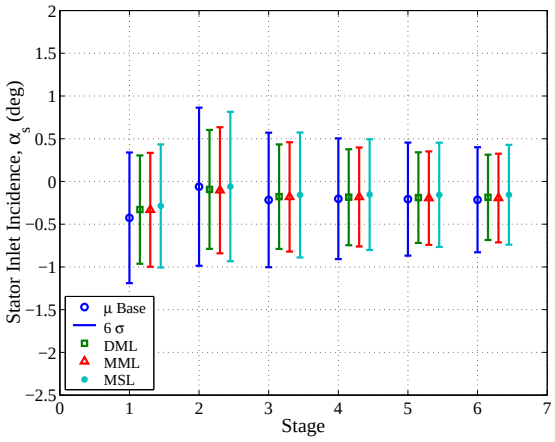

(b) $a = 1$: Stator incidence

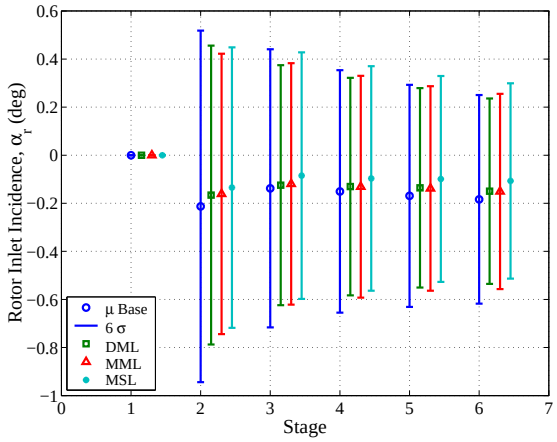

(c) $a = 2$: Rotor incidence

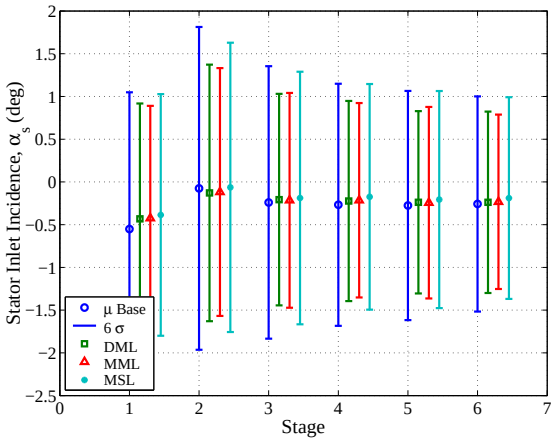

(d) $a = 2$: Stator incidence

Figure 5-6: Rotor and stator incidence variability

Figure 5-7 shows error-bar plots of stage exit Mach number (M_3) variability for each stage of the compressor model. Figures 5-7(a), (b) and (c) compare average and 6σ intervals for baseline and redesigned airfoil-based models at $a = 1$, 2 and 5 noise levels respectively. Figure 5-7(d) compares stage exit Mach number for the baseline airfoil-based model at the three noise levels. The mean stage exit Mach number decreases for each successive stage as the static temperature increases due to the work done by the rotor. At the higher noise amplitude values the effect of the probabilistic airfoil redesign becomes apparent: The average M_3 is lower for MML and MSL redesigns as is its corresponding variability. As with incidence, the Mach number variability decreases with each successive stage. As shown in Fig. 5-7(d), for a fixed canonical airfoil design (in this case the baseline airfoil), the average Mach number increases with noise amplitude as does its variability.

5.5 Multiple-Blade Rows

In the calculations reported above it was assumed that, for a given bladed row, all blade passages behaved identically, i.e., a single passage was considered for each bladed row. In this section, multiple passages per blade row are considered. For a given blade row, loss and turning values for each passage are sampled from the normal distribution according to inlet incidence. Thus in each passage loss and turning values are different, but with statistics prescribed by the loss and turning models for the specified incidence. The corresponding system of stage equations (Eqs. (5.1)–(5.3) or (5.4)) is solved for each passage. The outlet conditions are area-averaged to initialize the inlet conditions of the next rotor or stator and the calculation is marched through the compressor.

Table 5.2 shows polytropic efficiency and pressure ratio statistics for the six-stage compressor model reported above but with 80 blades per row (rotor or stator). Statistics for three levels of geometric variability and each redesigned canonical blade shape are reported. In comparing Table 5.2 to 5.1 it is seen that at the $a = 1$ noise level the mean shifts for the

Table 5.2: Six-stage compressor, IBR airfoil-based loss and turning models, 80 blade passages per row

a	Design	e^0	μ_e	$\sigma_e \times 10^3$	π^0	μ_π	σ_π
1	Base	0.963	0.961	0.033	10.79	10.73	0.005
	DML	0.969	0.968	0.022	11.09	11.04	0.006
	MML	0.969	0.968	0.021	11.20	11.14	0.006
	MSL	0.968	0.967	0.010	11.12	11.08	0.004
2	Base	0.963	0.960	0.065	10.79	10.72	0.010
	DML	0.969	0.967	0.045	11.09	11.02	0.011
	MML	0.969	0.967	0.044	11.18	11.11	0.011
	MSL	0.967	0.966	0.028	11.13	11.08	0.008
5	Base	0.963	0.953	0.197	10.79	10.61	0.029
	DML	0.969	0.961	0.163	11.09	10.90	0.033
	MML	0.969	0.961	0.145	11.30	11.13	0.033
	MSL	0.967	0.962	0.116	11.20	11.07	0.026

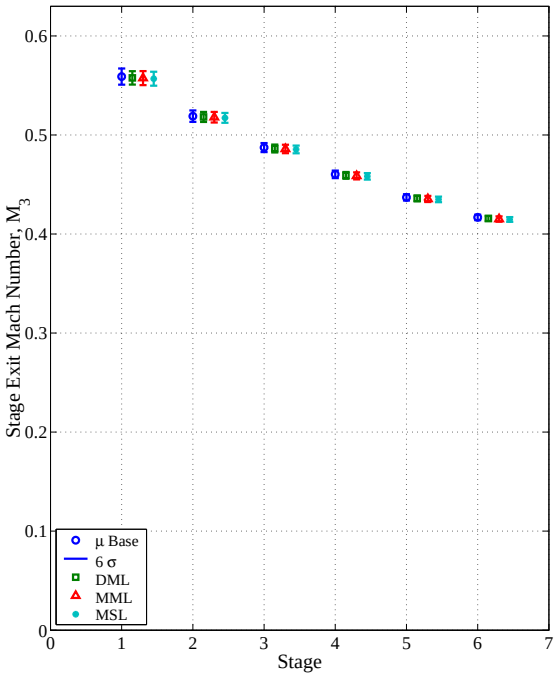

(a) $a = 1$: M_3 variability

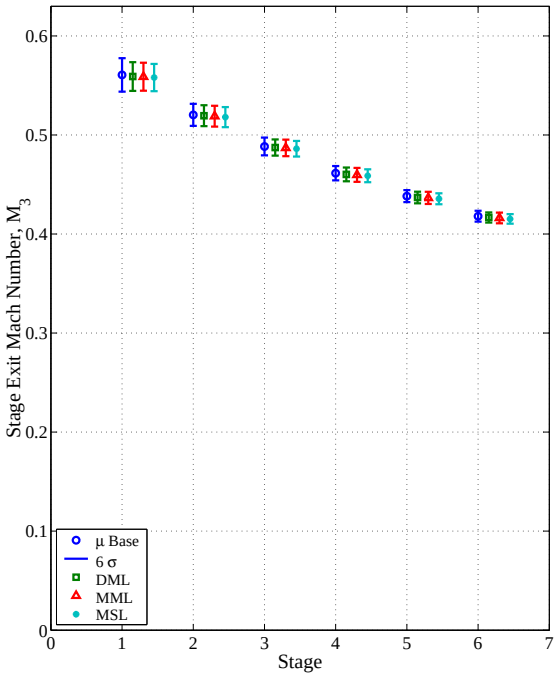

(b) $a = 2$: M_3 variability

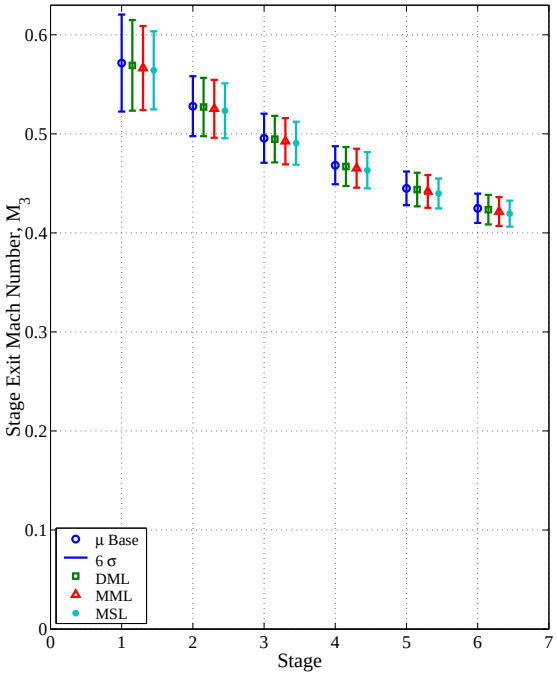

(c) $a = 5$: M_3 variability

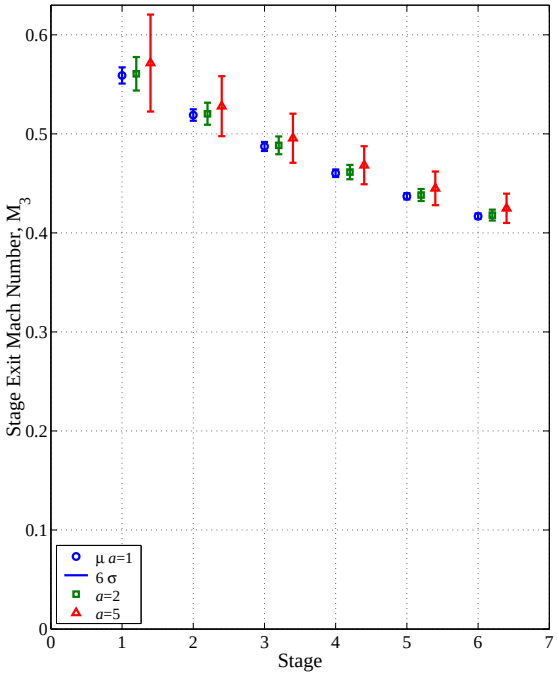

(d) Baseline airfoil: M_3 variability, $a = 1, 2, 5$

Figure 5-7: Stage exit Mach number variability

baseline multiple-blade calculation is the same as for the single-blade case. The efficiency and pressure ratio standard deviations in the multiple-blade case are 13 and 77% lower than in the single-blade case, respectively. At the $a = 5$ noise level the efficiency mean shift is now one percentage point, in contrast with the 1.2% drop seen with the single-blade calculation. The standard deviations of efficiency and pressure ratio have decreased by 30 and 75% from the single-blade calculations, respectively.

The reduction in efficiency and pressure ratio mean-shift can be explained in part by considering a deterministic compressor with loss and turning given by the mean values obtained from Monte Carlo simulation. As the number of blade passages is increased, the mean values of efficiency and pressure ratio converges to those obtained with the mean loss and turning models. Table 5.3 shows the resulting polytropic efficiency and pressure ratio values for the three noise levels considered. Comparing the values in Table 5.3 to those of

Table 5.3: Six-stage compressor, mean loss and mean turning (no variability)

	$a = 1$		$a = 2$		$a = 5$	
Design	e	π	e	π	e	π
Base	0.961	10.73	0.960	10.71	0.954	10.62
DML	0.968	11.04	0.968	11.02	0.961	10.91
MML	0.968	11.15	0.968	11.11	0.962	11.13
MSL	0.967	11.08	0.966	11.08	0.962	11.08

mean polytropic efficiency and pressure ratio in Table 5.2, and taking into account their reduced variability, it can be concluded that the contribution of the mean values of loss and turning (for given incidence) dominates the mean shifts of polytropic efficiency and pressure ratio.

5.6 Summary

In this chapter, a mean-line multi-stage axial compressor model was used to estimate the impact of geometric variability on overall compressor performance. Canonical probabilistic models of loss coefficient and turning angle versus incidence were constructed for an existing compressor rotor blade using Monte Carlo simulation. In the mean-line compressor model, upstream operating condition variability leads to variations in rotor inlet flow angle, axial Mach number, and total temperature and pressure. The later variabilities follow directly from upstream loss coefficient and turning perturbations. Since the annulus flow areas remain fixed, inlet total pressure and temperature fluctuations translate to axial Mach number and incidence perturbations. Inlet flow condition variability is compounded by rotor and stator loss and turning noise to produce variability in the stage exit conditions, which in turn affect the next stage.

The loss and turning models were used in probabilistic mean-line calculations for various redesigned airfoils at three noise amplitude levels. At the original noise level the impact on overall compressor polytropic efficiency is small (about 0.2% mean shift and 0.04% increase in coefficient of variability). Despite the small compressor performance variability predicted by the mean-line analysis, the effect of the redesigned airfoils can be detected at

the compressor level. The probabilistic MSL redesign, with very similar mean efficiency and pressure ratio as the minimum-loss redesigns, results in a decrease of 62% in standard devation of polytropic efficiency from the baseline airfoil model, and 46% when compared with the DML-based model.

At twice the original geometric noise level, the standard deviation of polytropic efficiency for the baseline design increased by more than a factor of two from the original noise level. A similar increase rate is seen in pressure ratio variability. The compressor model based on MSL-redesigned airfoils shows a decrease of 21% in standard deviation when compared with a model based on deterministic minimum loss. The pressure ratio COV decreases by about 8% when comparing the baseline to the MSL redesign-based models.

At the more realistic $a = 5$ noise level, the efficiency COV for the baseline model went up to 30%, a seven-fold increase from the $a = 1$ case. At this level of noise, the mean-shifts in polytropic efficiency is $\sim$1.2% for the baseline case but only 0.7% for the MSL-based model (i.e., a 42% reduction in mean-shift from baseline and 30% from DML). The decrease in efficiency uncertainty for the MSL-based model is 34% from the baseline airfoil and 26% from the DML airfoil-based model. The increase in pressure ratio COV is nearly linear with noise level, in agreement with the linear increase in turning variability with observed previously. Lastly, the MSL pressure ratio mean-shift is 25% lower than the corresponding baseline and DML values. The enforcement of turning angle constraints at the airfoil level led to redesigned airfoils with similar pressure ratio mean and standard deviation, with advantageous implications for stall margin.

When considering multiple blade passages (80 blades in the present case), the impact of the scatter about the mean loss and turning angle values was seen to decrease, leaving the mean values as the dominant contributors to mean shift in polytropic efficiency and pressure ratio. For a realistic $a = 5$ noise level the polytropic efficiency mean-shift was found to be 1%.

Rotor and stator incidence variability was found to decrease for each successive downstream stage. For the same canonical airfoil design the average Mach number increases with noise amplitude as does its variability. As with incidence, the Mach number variability decreases with each successive stage.

Chapter 6

Summary and Recommendations

In this thesis, statistical and probabilistic techniques are used to assess the impact of geometric variability on axial compressor performance. The following is a recapitulation of the thesis.

- A statistical analysis of high-resolution compressor blade surface measurements was performed using principal component analysis (PCA). The analysis resulted in high-fidelity models of geometric variability suitable for use in probabilistic simulation and optimization. The geometric noise modes were found in general not to correspond directly to geometric parameters of known aerodynamic importance.

- The impact of manufacturing variability on blade row aerodynamic performance was assessed using Monte Carlo simulation and a quasi-two-dimensional cascade analysis code. Geometric variability was introduces via the aforementioned PCA-based model derived from existing hardware measurements. Loss and turning variability were found to grow linearly with geometric noise amplitude. Discrepancies between nominal and mean loss coefficient of 23% were observed at five-times the baseline noise level. Supersonic-inlet test cases exhibited higher loss variability than subsonic ones for the same type and level of geometric variability.

- A mean-line multi-stage axial compressor model was used to estimate the impact of geometric variability on overall compressor performance. Canonical probabilistic models of loss coefficient and turning versus incidence were constructed for an existing compressor rotor blade. In the mean-line compressor model inlet flow condition variability is compounded by rotor and stator loss and turning noise to produce variability in the stage exit conditions, which in turn affect the subsequent stages. Probabilistic loss and turning models were used in mean-line simulations of a six-stage compressor with nominal pressure ratio of 11. At realistic levels of geometric variability the discrepancy between nominal and mean polytropic efficiency was found to be around one percentage point. Pressure ratio variability was found to vary linearly with geometric variability amplitude. Rotor and stator incidence variability was found to decrease with distance through the compressor. For the same canonical airfoil design the mean exit Mach number increased with noise amplitude as did its variability. Mach number variability was also found to decrease with distance through the compressor. When considering multiple-blade rows it was found that the mean shifts in loss coefficient and turning angle dominate the mean shifts in polytropic efficiency and pressure ratio.

- A probabilistic gradient-based approach to compressor blade optimization was developed. The probabilistic objectives, constraints and their corresponding gradients are approximated using low-fidelity Monte Carlo simulation. An external nonlinear optimization driver was used to drive the probabilistic simulations. Design modes included Chebyshev polynomials acting on the airfoil surface and solid-body rotation to optimize stagger angle. The airfoils were optimized both deterministically for minimum loss, and probabilistically for minimum mean loss and minimum loss variability The airfoils were then subjected to simulated geometric variability to assess its impact on their performance. Reductions in mean loss coefficient of up to 25% and in loss variability of up to 65% relative to deterministically redesigned airfoils were observed. At the compressor level, simulations using airfoils optimized probabilistically for minimum loss variability exhibited reductions of 30 to 40% in polytropic efficiency variability and mean-shift compared simulations using deterministically-redesigned airfoils.

- For subsonic airfoils viscous dissipation was found to dominate the rate of entropy generation. A decrease in the rate of flow deceleration on the entry region of the pressure side reduced the entropy generation variability for subsonic inlet airfoils. In supersonic inlet airfoils, a decrease in the rate of flow deceleration immediately downstream of the shock impingement location on the suction side reduced the loss variability caused by shock-boundary layer interaction.

Recommendations For Future Work

Probabilistic turbomachinery analysis and design is a relatively new area of research. The following is a categorized list of suggestions for further work on some of the areas touched in this thesis.

Applications

- The techniques outlined in Chapters 2 and 3—or variants thereof—could be used to assess the validity or relevance of current industrial manufacturing tolerancing practices.

- It would also be of interest to build a "catalog" of common geometric modes encountered in specific manufacturing processes. Such catalog could be employed, for instance, in proposing new manufacturing tolerancing schemes backed by aerodynamic (functional) information in addition to the traditional heuristics and past experience of current use.

- The main premise of Chapter 2—to obtain high-definition measurements of actual production hardware and analyze the data statistically—could as well be applied to characterizing geometric variability incurred during engine operation. Clearly, the main obstacles to such a study are the need for large numbers of samples and the costs involved in measuring them.

- As illustrated in Chapter 4, nominal airfoil shape modifications can contribute to the reduction of performance variability. Further redesign features should be explored over a wide range of airfoil types and geometric variability characteristics.

Extensions

- As briefly discussed in Appendix A, PCA may be used to characterize and construct *three-dimensional* of compressor blade variability.

- A natural extension of the investigations reported in Chapters 2 and 3 would be to perform a "quasi-3D" probabilistic analysis of an entire blade. Such study would involve obtaining geometric variability models and performing probabilistic analysis of multiple blade sections along the blade span. A simple feedback loop can then be established with the throughflow analysis code to take into account changes in streamtube radial paths and thickness.

- The mean-line model reported in Chapter Five can be greatly improved by considering multiple-stage quasi-2D models (i.e., with different nominal blades and probabilistic loss and turning models per stage) augmented by end-wall correlations to account for casing boundary layer blockage effects.

- The extended compressor model may be used in parametric studies of high-pressure compressors in more general design spaces, e.g., to study the changes in compressor performance variability for fixed target pressure ratio and variable number of stages, etc.

Methodology

- The nonlinear constrained optimization algorithm used in Chapter 4 (SQP), assumes that the program being solved is convex, i.e., minimization of a convex function over a convex region. Although convexity can be expected to hold in a small region around the origin (baseline design), the use of global optimization techniques (see for instance Ref. 18) may allow for more effective tradespace explorations.

- In Chapter 4, low-resolution Monte Carlo simulations were used as a surrogate of high-fidelity ones, the idea being that approximate probabilistic gradient information is sufficient to drive the probabilistic airfoil optimization. Other forms of surrogate models are also possible, e.g., polynomial fits, neural nets, etc. A way to infuse more fidelity during probabilistic optimization may be to use combinations of surrogate and high-fidelity evaluations. The optimal "schedules" for alternating low and high-resolution function evaluations should be investigated.

- Additional research on the importance of deterministic sensitivity-derivative accuracy to the effectiveness of gradient-based probabilistic optimization needs to be carried out. In particular, trade-offs among ease of implementation (and retro-fitting), fidelity and computational expense of various methods (e.g., finite-difference approximations, solving sensitivity equations or implementing adjoint-based solvers) should be addressed in the context of gradient-based probabilistic optimization of turbomachinery components.

- Throughout the thesis, simple Monte Carlo sampling was used to estimate the statistics of functions of random variables. As a first step to improve computational efficiency, the use of variance reduction techniques (e.g., stratified sampling) should be evaluated.

- The calculations reported in this thesis took advantage of the easily parallelizable nature of Monte Carlo simulation. On the other hand, less expensive probabilistic analysis methods may be not only desirable alternatives to Monte Carlo but perhaps even the only feasible means to assess the impact of geometric variability on compressor airfoil performance as higher fidelity results are sought.

Appendix A

Principal Component Analysis

A.1 Background

The primary underlying idea in principal component analysis is the modal decomposition of data sets (from experiments, numerical simulations, field observations, etc.) into bases which are *optimal* in a statistical sense. This idea is known to various disciplines under different names: Proper orthogonal decomposition (POD), Karhunen-Loève expansion, singular system analysis, singular value decomposition (SVD), etc. [60].

In fluid mechanics POD has been widely used in the analysis of experimental and simulation data [117], particularly in turbulence [15,42,77]. PCA has found applications in random variables [75,95], image processing [49,93,107] and other computer science applications [5,6], and meteorology [76,100]. Computer packages implementing the Karhunen-Loève decomposition to study the spatiotemporal behavior of dynamical systems have been reported [8,57]. More recently POD has been used in constructing reduced-order aerodynamic models for applications in turbomachinery control [54, 106, 136, 137]. Häcker [52] used principal components analysis and other statistical techniques to map simulated compressor blade shape variability to aerodynamic performance.

According to Preisendorder [100] the origins of PCA can be traced back to the 1870s and the work of Beltrami, Jordan and Wierstrass who laid down the foundations for what is now known as the Singular Value Decomposition. Lumley [77] reports that in the 1940s and 50s research in this area was independently carried out by various researchers including Kosambi [74], Loève [75], Karhunen, Pougachev [99] and Obukhov [92]. E. N. Lorenz suggested the technique in the context of weather prediction [76].

A.2 Basic Theory

The presentation of PCA that follows has been adapted from Refs. 100 and 67 to the characterization of geometric variability in turbomachinery airfoils.

The nominal airfoil geometry is defined by p coordinate points $\mathbf{w}^0(x) \in \mathbb{R}^m$, $x = 1, \ldots, p$ where m is typically 2 or 3. We consider a set of n coordinate measurements $\{\hat{\mathbf{w}}(t, x) \in \mathbb{R}^m \mid t = 1, \ldots, n;\ x = 1, \ldots, p\}$ taken, for instance, with a coordinate-measuring machine. The integral values of x uniquely identify a specific nominal point and its measured counterparts. Similarly t identifies a particular set of measured points. The discrepancies in the

coordinate measurements can be expressed as

$$\mathbf{w}'(t,x) = \hat{\mathbf{w}}(t,x) - \mathbf{w}^0(x), \quad t = 1,\ldots,n;\ x = 1,\ldots,p\ .$$

Subtracting from these error vectors their ensemble average given by

$$\bar{\mathbf{w}}(x) = \frac{1}{n}\sum_{t=1}^{n} \mathbf{w}'(t,x), \quad x = 1,\ldots,p\ ,$$

gives a t-centered set of m-dimensional vectors, $\mathcal{W} = \{\mathbf{w}(t,x) = \hat{\mathbf{w}}(t,x) - \bar{\mathbf{w}}(x) \mid t = 1,\ldots,n;\ x = 1,\ldots,p\}$.

Let $\mathbf{w}(t) = [\mathbf{w}^T(t,1),\ldots,\mathbf{w}^T(t,p)]^T$ and consider a unit vector $\mathbf{e} \in \mathbb{R}^{mp}$ with sub vectors $\mathbf{e}(x) \in \mathbb{R}^m$, so that $\mathbf{e} = [\mathbf{e}(1)^T,\ldots,\mathbf{e}^T(p)]^T$. The *scatter* of $\mathcal{W}$ along $\mathbf{e}$ is defined to be

$$\begin{aligned}\psi(\mathbf{e}) &\equiv \sum_{t=1}^{n} [\mathbf{w}^T(t)\mathbf{e}]^2 \\ &= \mathbf{e}^T \left(\sum_{t=1}^{n} \mathbf{w}(t)\mathbf{w}^T(t)\right)\mathbf{e} \\ &= \mathbf{e}^T\mathbf{S}\mathbf{e} \geq 0\end{aligned}$$

where the *scatter matrix* $\mathbf{S}$ is composed of the $m \times m$ sub matrices

$$\mathbf{S}(x,y) = \sum_{t=1}^{n} \mathbf{w}(t,x)\mathbf{w}(t,y)$$

The set $\mathcal{W}$ of t-centered error vectors can be written in matrix form as

$$\mathbf{X} \equiv [\mathbf{X}(1),\ldots,\mathbf{X}(p)]$$

where $\mathbf{X}(x) \equiv [\mathbf{w}^T(1,x),\ldots,\mathbf{w}^T(n,x)]^T$. Then the scatter matrix can be more succinctly written as

$$\mathbf{S} = \mathbf{X}^T\mathbf{X}.$$

The scatter matrix is related to the covariance matrix $\mathbf{C}$ simply by $\mathbf{C} = (n-1)^{-1}\mathbf{S}$.

We are interested in finding directions which minimize (or maximize) the scatter ψ. Assume that $\mathbf{v} \in \mathbb{R}^{mp}$ is one such direction. Then for a small perturbation $\delta\mathbf{v}$

$$\psi(\mathbf{v} + \delta\mathbf{v}) = \psi(\mathbf{v}) + \mathcal{O}(|\delta\mathbf{v}|^2)$$

so that, to first order $\psi(\mathbf{v} + \delta\mathbf{v}) \approx \psi(\mathbf{v})$. On the other hand, from the definition of ψ we have

$$\begin{aligned}\psi(\mathbf{v} + \delta\mathbf{v}) &= (\mathbf{v} + \delta\mathbf{v})^T\mathbf{S}(\mathbf{v} + \delta\mathbf{v}) \\ &= \mathbf{v}^T\mathbf{S}\mathbf{v} + \mathbf{v}^T\mathbf{S}\delta\mathbf{v} + \delta\mathbf{v}^T\mathbf{S}\mathbf{v} + \delta\mathbf{v}^T\mathbf{S}\delta\mathbf{v},\end{aligned}$$

since $\mathbf{S} = \mathbf{S}^T$, $\mathbf{v}^T\mathbf{S}\delta\mathbf{v} = \delta\mathbf{v}^T\mathbf{S}\mathbf{v}$, to first order, $\psi(\mathbf{v} + \delta\mathbf{v}) \approx \mathbf{v}^T\mathbf{S}\mathbf{v} + 2\delta\mathbf{v}^T\mathbf{S}\mathbf{v}$, which implies

$$\delta\mathbf{v}^T\mathbf{S}\mathbf{v} = 0. \tag{A.1}$$

From the requirement that $\|\mathbf{v} + \delta\mathbf{v}\|_2 = 1$, we get

$$\mathbf{v}^T\mathbf{v} + \mathbf{v}\delta\mathbf{v} + \delta\mathbf{v}\mathbf{v} + \delta\mathbf{v}^T\delta\mathbf{v} = 1$$

which to first order is equivalent to

$$\delta\mathbf{v}^T\mathbf{v} = 0, \tag{A.2}$$

i.e., to first order the perturbations only alter the direction of $\mathbf{v}$.

To combine Eqs. (A.1) and (A.2) we multiply the latter by $\lambda \in \mathbb{R}$ having the same units as the entries of $\mathbf{S}$, yielding

$$\delta\mathbf{v}^T(\mathbf{S}\mathbf{v} - \lambda\mathbf{v}) = 0. \tag{A.3}$$

Since Eq. (A.3) must hold for arbitrary perturbations satisfying Eq. (A.2), it follows that the extrema of the scatter probe occur along directions which are nontrivial solutions of the eigenvalue problem

$$\mathbf{S}\mathbf{v} = \lambda\mathbf{v}. \tag{A.4}$$

Since $\mathbf{S}$ is symmetric positive definite [1], it has in general mp orthonormal eigenvectors $\mathbf{v}_i \in \mathbb{R}^{mp}, i = 1, \ldots, mp$ with corresponding real, non-negative eigenvalues [130], i.e., if $\mathbf{V} = [\mathbf{v}_1, \ldots, \mathbf{v}_{mp}]$, then $\mathbf{V}^T\mathbf{V} = \mathbf{V}\mathbf{V}^T = \mathbf{I}$ and

$$\mathbf{V}\mathbf{S} = \mathbf{V}\mathbf{\Lambda} \tag{A.5}$$

where $\mathbf{\Lambda} = \mathrm{diag}(\lambda_i, \ldots, \lambda_{mp})$, $\lambda_1 \geq \ldots \geq \lambda_{mp} \geq 0$. Equation (A.5) is a statement of the *eigenvector property* of $\mathbf{S}$ [100].

The orthonormal columns of $\mathbf{V}$ span $\mathbb{R}^r$ where $r \leq mp$ is the rank of $\mathbf{S}$. Therefore the original data vectors can be represented as linear combinations of the eigenvectors of $\mathbf{S}$. From the orthogonality of $\mathbf{V}$ we can write the identity

$$\mathbf{X} = \mathbf{X}\mathbf{V}\mathbf{V}^T.$$

Introducing the $n \times mp$ matrix of amplitudes $\mathbf{A} \equiv \mathbf{X}\mathbf{V}$ we can rewrite the above as

$$\mathbf{X} = \mathbf{A}\mathbf{V}^T \ . \tag{A.6}$$

Equation (A.6) is called the PCA *synthesis* formula [100]. The entries of $\mathbf{A}$ have the same dimensions as the entries of $\mathbf{X}$, i.e., as the data vectors. The columns of $\mathbf{A}$ are the *principal component* or amplitude vectors in $\mathbb{R}^n$ and can be thought of as the amplitudes modulating a set of modes given by the eigenvectors of $\mathbf{S}$.

From the eigenvector property of $\mathbf{S}$ it follows that

$$\mathbf{A}^T\mathbf{A} = (\mathbf{X}\mathbf{V})^T(\mathbf{X}\mathbf{V}) = \mathbf{V}^T(\mathbf{X}^T\mathbf{X})\mathbf{V} = \mathbf{V}^T\mathbf{S}\mathbf{V} = \mathbf{V}^T\mathbf{V}\mathbf{\Lambda},$$

that is

$$\mathbf{A}^T\mathbf{A} = \mathbf{\Lambda} \ . \tag{A.7}$$

This last expression is called the *PCA property* of the data set $\mathbf{X}$.

The total scatter (or *energy* [8]) E of the data set $\mathcal{W}$ is given by

$$\mathsf{E} = \mathrm{tr}(\mathbf{S}) = \mathrm{tr}(\mathbf{X}^T\mathbf{X}) = \|\mathbf{X}\|_F^2$$

[1] For any nonzero vector $\mathbf{v}$, $\mathbf{v}^T\mathbf{S}\mathbf{v} = \mathbf{v}^T\mathbf{X}^T\mathbf{X}\mathbf{v} = (\mathbf{X}\mathbf{v})^T(\mathbf{X}\mathbf{v}) = \|\mathbf{X}\mathbf{v}\|_2^2 > 0$

where $\|\cdot\|_F^2$ stands for the Frobenius norm. Using the fact that the Frobenius norm is invariant under unitary multiplication [130] we can write

$$\mathsf{E} = \|\mathbf{A}\mathbf{V}^T\|_F^2 = \|\mathbf{A}\|_F^2 = \mathrm{tr}(\mathbf{A}^T\mathbf{A}) = \mathrm{tr}(\mathbf{\Lambda}) = \sum_{j=1}^{mp} \lambda_j \ .$$

Therefore the total scatter of the data set is given by the sum of squares of the entries of the principal component vectors or, equivalently, by the sum of the eigenvalues of the scatter matrix $\mathbf{S}$. The latter can also be seen by applying the scatter probe to each eigenvector $\mathbf{v_j}, j = 1, \ldots, mp$ of $\mathbf{S}$,

$$\psi(\mathbf{v}_j) = \mathbf{v}_j^T\mathbf{S}\mathbf{v}_j = \mathbf{v}_j^T\lambda_j\mathbf{v}_j = \lambda_j \ ,$$

by the orthogonality of $\mathbf{V}$. Therefore, the scatter of the data set along a particular eigenvector is given by its corresponding eigenvalue.

Directly computing the eigenvalue decomposition of $\mathbf{S}$ (Eq. (A.5)) can become computationally expensive for large n, m, p. An alternate, less expensive computation is motivated as follows. Define the normalized amplitude matrix $\mathbf{U}$ to have columns $\mathbf{u}_j(t) = \mathbf{a}_j(t)/\sqrt{\lambda_j}, j = 1, \ldots mp$, where $\mathbf{a}_j(t) \in \mathbb{R}^n$ are the principal components of the data set. Then

$$\mathbf{A} = \mathbf{U}\mathbf{\Sigma}$$

where $\mathbf{\Sigma} = \mathrm{diag}(\sigma_1, \ldots, \sigma_{mp})$, $\sigma_j = \sqrt{\lambda_j}$, $j = 1, \ldots, mp$. The PCA property can be rewritten as

$$\mathbf{U}^T\mathbf{U} = \mathbf{I}$$

and the synthesis formula becomes

$$\mathbf{X} = \mathbf{U}\mathbf{\Sigma}\mathbf{V}^T \ . \tag{A.8}$$

The above expression is a statement of the *Singular Value Decomposition* (SVD) of $\mathbf{X}$ in reduced form [130], which is made unique by requiring that $\{\sigma_j\}_{j=1}^{mp}$ be a non-increasing sequence. Computing the SVD of $\mathbf{X}$ is less expensive and more numerically stable than finding the full eigenvalue decomposition of $\mathbf{S}$. Furthermore, the form of Eq. (A.8) can be readily cast to include cases for which $\mathrm{rank}(\mathbf{S}) \leq n < mp$.

A.3 Three-Dimensional Analysis of IBR Blade Measurements

An alternative application of PCA to the IBR measurements discussed in Chapter 2 is to consider all 13 sections at once in a three-dimensional analysis. The 3-D analysis allows for the possibility of section-to-section effects that were precluded by the two-dimensional assumption made priorly.

Using the notation introduced above, the t-centered measurements are collected into $n \times mp$ matrix $\mathbf{X}$, where now $n = 52$, $m = 3$ and $p = 112$. As before, the eigenmodes and eigenmodes of the scatter matrix $\mathbf{S}$ are obtained from the singular value decomposition of $\mathbf{X}$.

Figures A-2 and A-3 show the effect of the mean airfoil perturbation and the first five modes. The scalar quantity plotted is the displacement in the direction normal to the baseline blade surface (outward positive). For ease of visualization, the surface of the airfoil

has been "unwrapped": the suction surface of the blade corresponds to the horizontal interval $-1 \leq x \leq 0$, while the pressure side is corresponds to $0 < x \leq 1$, with the leading edge is located at 0. The portion of the measured span has been normalized. To facilitate comparison of leading- and trailing-edge effects, a transformation defined by

$$T : x \mapsto \begin{cases} \frac{1}{2}\left[1 - \cos \pi(x-1)\right] - 1 & -1 \leq x < 0 \\ \frac{1}{2}\left(1 - \cos \pi x\right) & 0 \leq x \leq 1 \end{cases}$$

has been used on to the chord-wise component. In the plots, the bottom horizontal axis corresponds to the transformed abscissa coordinate, $T^{-1}(x)$, while the top auxiliary horizontal axis indicates the original x coordinate value. Figure A-1 shows the effect of T^{-1} on a uniform grid.

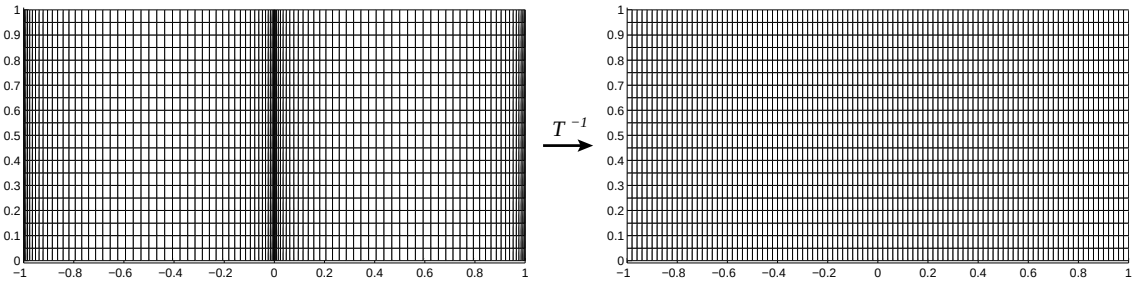

Figure A-1: Transformation T

Figures A-2 and A-3 suggest the existence of three-dimensional components of geometric variability modes acting along the blade span and not only along its axial and tangential directions.

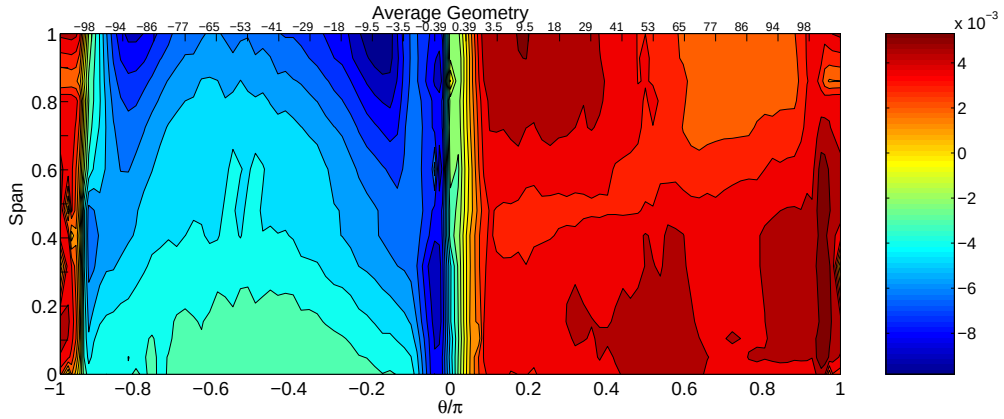

(a) Average Geometry

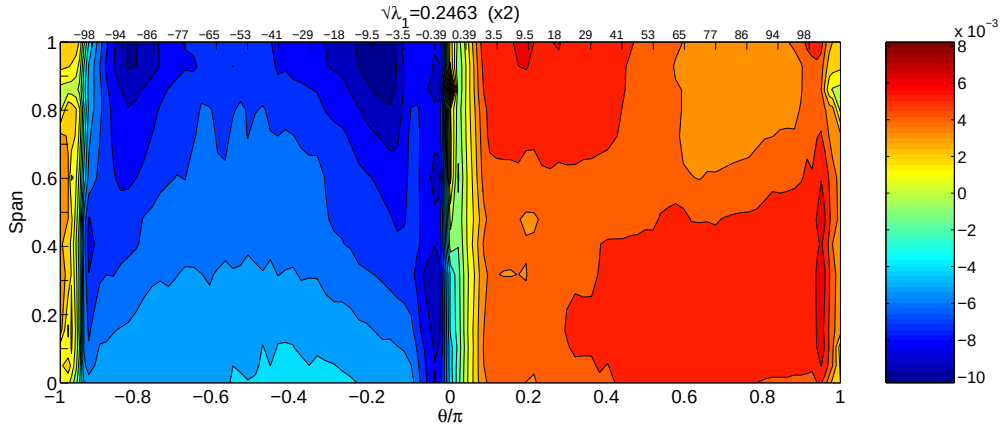

(b) Mode 1

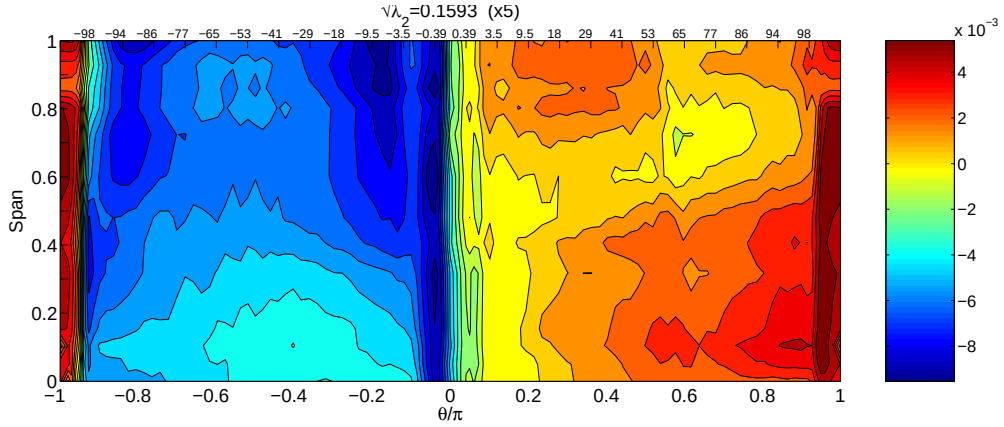

(c) Mode 2

Figure A-2: Three-dimensional geometric modes

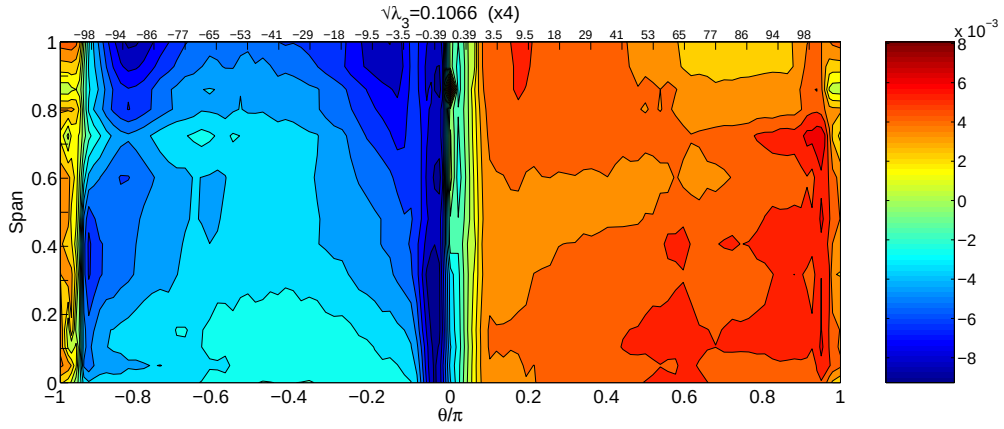

(a) Mode 3

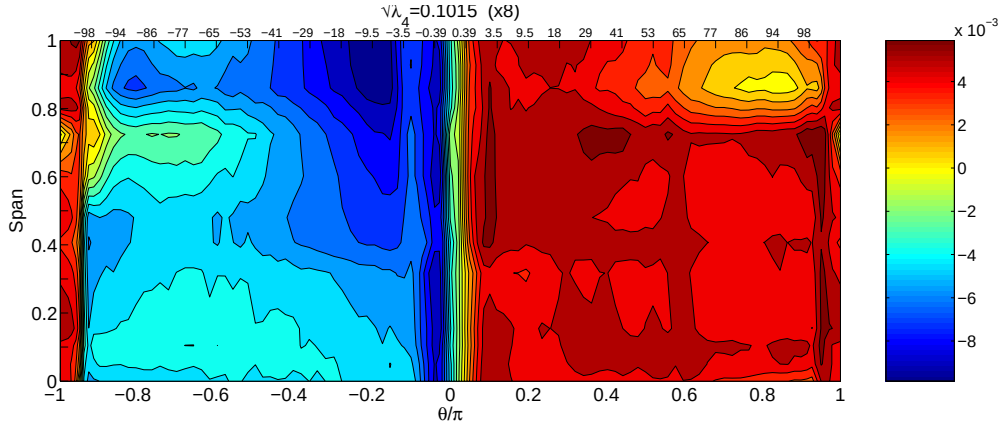

(b) Mode 4

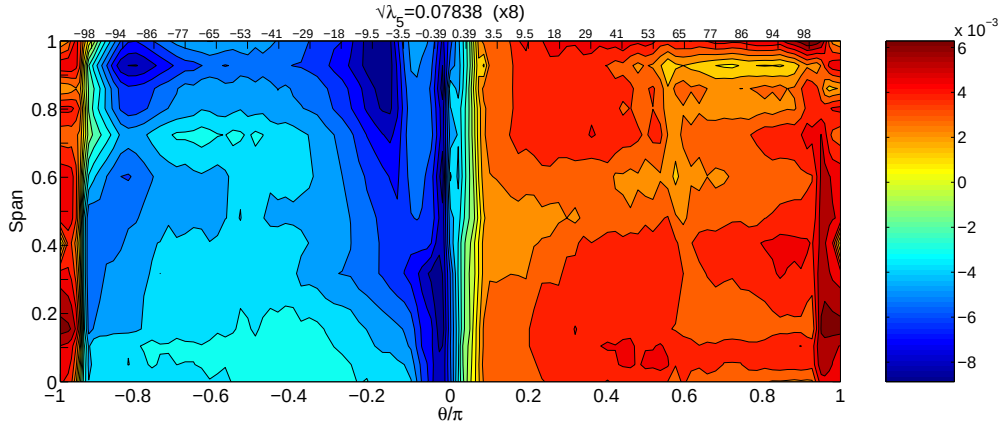

(c) Mode 5

Figure A-3: Three-dimensional geometric modes (Cont'd)

Appendix B

Point- Vs. Flank-Milled Compressor Blade Rows

Point milling is a well understood and widely used method for manufacturing compressor blades. In this technique, a ball cutter removes material from a block of metal following computer-controlled paths. The main disadvantages of point milling are the time required to cut an entire blade surface in several passes and the resulting scalloped surface finish [138]. An alternative to point milling that is starting to become practical is flank milling, whereby a conical tool is used to cut the entire surface of a blade from the blank material in a single pass [138]. Flank milling poses a more challenging tool control problem than point milling, but can potentially be more time and cost effective. Another advantage of flank milling is that it produces a better surface finish than point milling, requiring less time for surface polishing.

The integrally bladed rotor (IBR) discussed throughout this thesis was manufactured via flank milling. Production hardware is likely to be manufactured using other more common techniques like point milling. Figure B-1 shows plots of measured deviations of two production compressor rotor blades, one manufactured with point milling and the other with flank milling. Deviations in chord length, leading-edge thickness and trailing-edge thickness at various spanwise locations are shown. The deviations have been scaled with respect to the nominal spanwise average chord. Largest positive and negative deviations at each spanwise station are indicated by dashed lines, which in turn provides a rough measure of variability in each measured dimension. Table B.1 shows maximum deviations (per unit chord) intervals in chord, leading and trailing-edge thickness for the measurements shown in Fig. B-1. The point-milled IBR exhibits roughly 18 times more variability in chord

Table B.1: Spanwise maximum deviation intervals (per unit chord) for point- and flank-milled IBR measurements.

Dimension	Point ($\times 10^3$)	Flank ($\times 10^3$)	Ratio
Chord length	8.6	0.49	18
LE thickness	2.7	0.49	6.7
TE thickness	3.8	0.57	5.6

length than the flank-milled IBR. The variability in LE and TE thickness measurements for

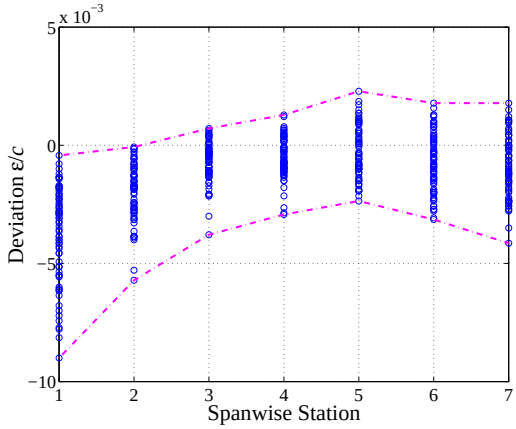

(a) Point-milled IBR: Chord length

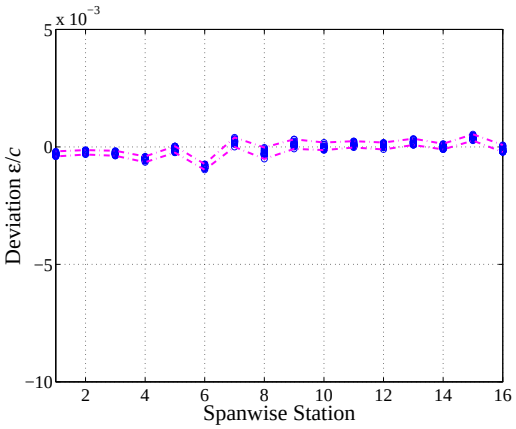

(b) Flank-milled IBR: Chord length

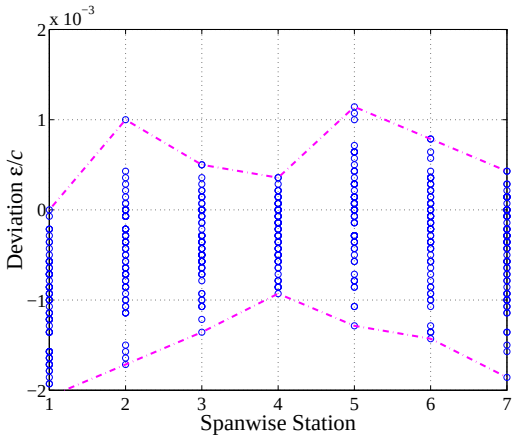

(c) Point-milled IBR: LE thickness

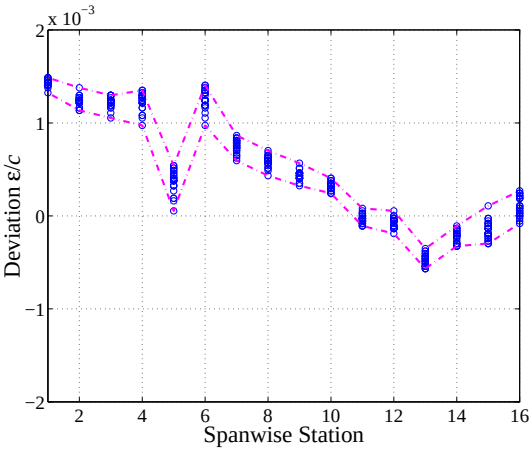

(d) Flank-milled IBR: LE thickness

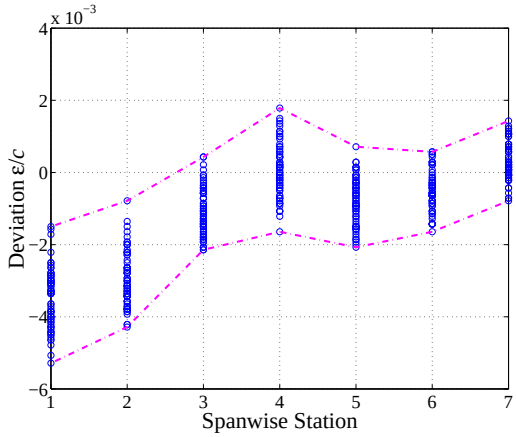

(e) Point-milled IB9: TE thickness

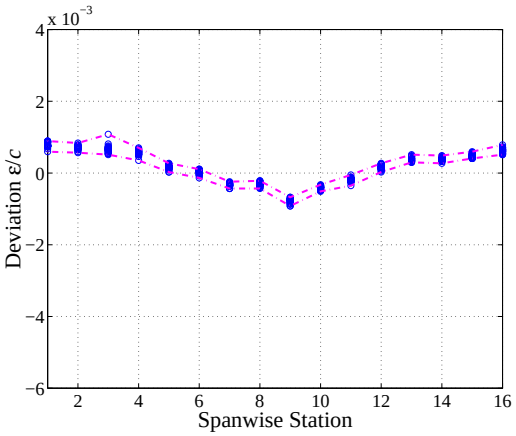

(f) Flank-milled IBR: TE thickness

Figure B-1: Measured deviations for sample point and flank-milled IBR

the point-milled IBR is roughly six times that of the flank-milled rotor. This comparison provides a justification for the higher geometric variability levels considered in Chapters 3–6.

Appendix C

Robustness Via Constrained Probabilistic Optimization

Various definitions of *robustness* have been introduced in the context of design under uncertain conditions [98, 124]. In the present context a *robust* blade passage design is one that exhibits improved mean performance and reduced sensitivity to geometric and flow parameter variability when compared to a baseline design.

A comparison of problems (4.1) and (4.2) suggests a probabilistic nonlinear program of the form

$$\begin{aligned} \sigma^*_{\varpi} = \min_{\mathbf{x}\in\Omega'} & \left\{ \operatorname*{Var}_{\theta}(\varpi(\mathbf{x},\theta)) \right\}^{\frac{1}{2}} \\ \text{s.t.} \quad & \vartheta_l \leq \operatorname*{\mathbb{E}}_{\theta}[\vartheta(\mathbf{x},\theta)] \leq \vartheta_u, \\ & \operatorname*{\mathbb{E}}_{\theta}[\varpi(\mathbf{x},\theta)] = \varpi^* \ . \end{aligned} \tag{C.1}$$

Assuming that, in some subset Ω' of the design space Ω, σ^*_{ϖ} varies continuously with ϖ^* and is furthermore monotonically decreasing in ϖ^*, then an acceptable level of mean performance degradation may be traded by a profitable reduction in output variability.

To illustrate a mean performance vs. variability study, the IBR airfoil introduced in Chapters 2–5 was redesigned to meet the mean loss equality constraints summarized in Table C.1. A geometric noise level $a = 5$ was assumed. The design variables and tradespace were similar to those used in Sect. 4.2.3 with the exception that no stagger angle changes were allowed. The turning constraint was relaxed to $14.4 \leq \mu_\vartheta \leq 15.4$. To ensure sufficient resolution of the equality constraints $N_{\text{opt}} = 200$ trials were used. All optimization runs were started from the baseline geometry.

The mean loss constraint values in Table C.1 were selected to subdivide the mean loss interval between the values computed for the MML and MSL redesigns (see Table 4.2) into five segments (roughly) uniformly-spaced. The problem names given in the table identify the resulting redesigned airfoils and their performance statistics in Figs. C-1 and C-2. Figure C-1 gives final standard deviation versus mean mean loss coefficient (computed via MCS, $N = 2000$) for the four trade-off airfoils, as well as those of the MML and MSL airfoils discussed earlier. The highest variability corresponds to the MML redesign, as does the smallest mean loss. The largest mean loss value corresponds to the minimum standard deviation airfoil (MSL). The four trade-off redesigns lie between the MSL and MML cases.

Table C.1: IBR $a = 5$: Mean vs. variability trade-off problem constraints

Problem	$\mathbb{E}_\theta[\varpi(\mathbf{x})]$
TO1	2.78
TO2	2.83
TO3	2.91
TO4	2.98

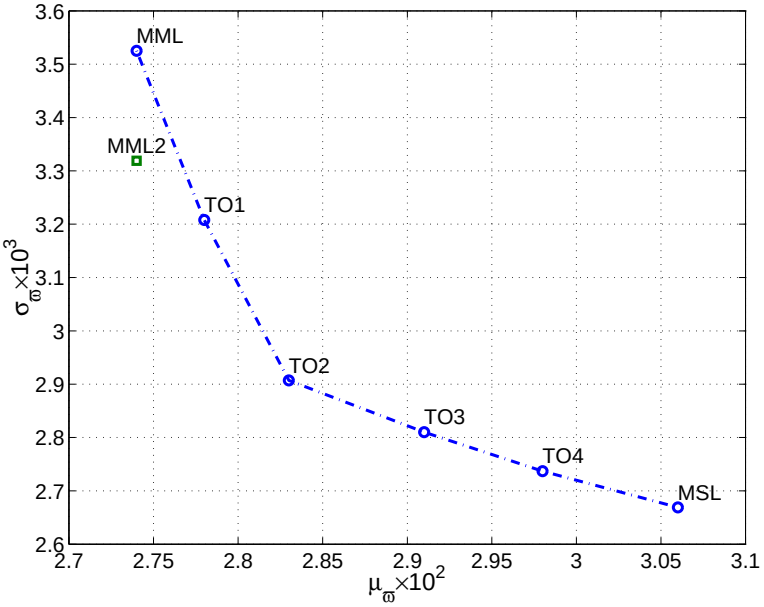

Figure C-1: IBR: Mean loss coefficient vs. standard deviation ($a = 5$)

The graph can be interpreted in two ways. As the loss coefficient constraint is eased (i.e., larger values are considered), the possibility to reduce loss variability increases. Conversely, as the requirement for reduced uncertainty is reduced, minimum mean loss that can be reduced.

Point labeled MML2 in Fig. C-1 corresponds to the mean loss and standard deviation obtained by minimizing the mean loss starting with the TO2 trade-off design. The design space explored was the same as in the previous programs. The fact that a design was obtained resulting in roughly the same minimum mean loss, but with reduced uncertainty, suggests that a useful strategy for minimizing mean loss while reducing variability is to first minimize variability and then improving mean performance.

Figures C-2 show geometric features of the redesigned airfoils TO1 through TO4 compared to the MML and MSL airfoils. The geometric trends that led to designs with reduced variability are seen also in the TO3 and TO4 airfoils, namely a somewhat thicker leading edge (from building up the pressure side) and a shifting of the maximum camber location aft. However, the thickness and camber transformations among the three sections are not linear scalings of those in the MSL airfoil. Similarly, thinner sections in the forward portion of the airfoil and a shifting of the maximum thickness toward the rear of the airfoil are

characteristic to the low-loss/high-variability designs (MML, TO1, TO2).

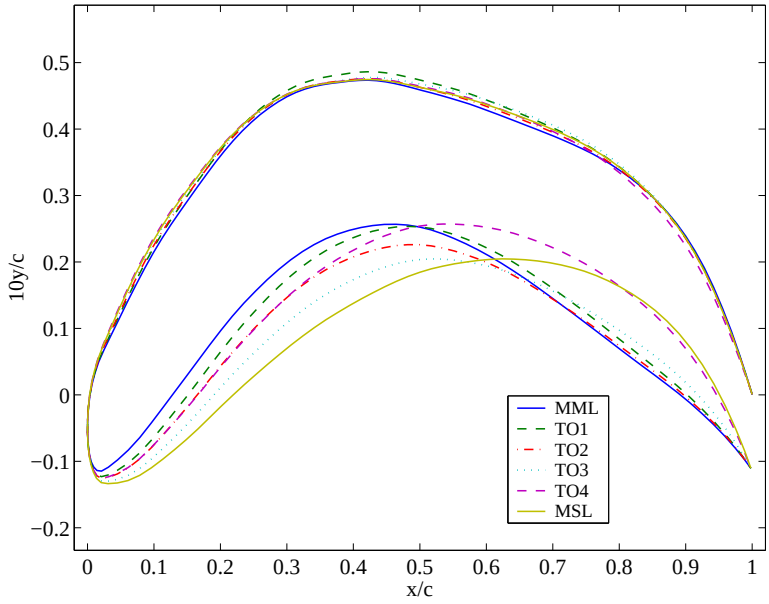

(a)

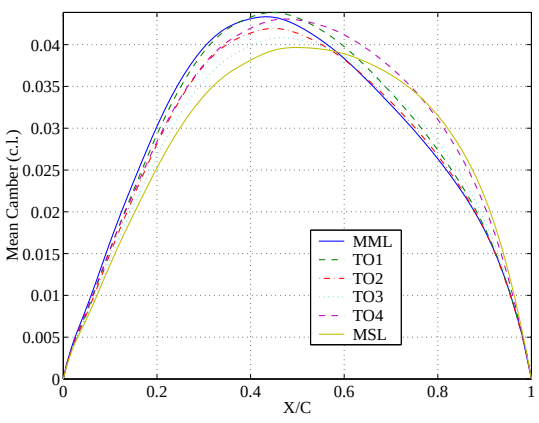

(b)

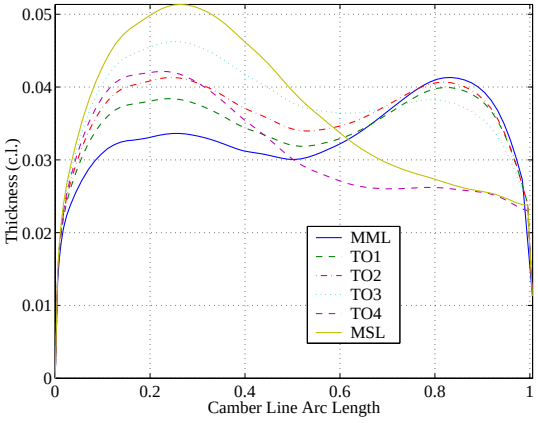

(c)

Figure C-2: IBR ($a = 5$): Geometric features of "trade-off" redesigns

Appendix D

Mean-Line Compressor Model

D.1 Nomenclature

Variables

T	Temperature	P	Pressure
M	Mach number	a	Speed of sound
V	Velocity	u	Axial velocity
v	Tangential velocity	r	Radius
ρ	Density	h	Enthalpy
α	Absolute flow angle	β	Relative flow angle
ω	Wheel speed	ϕ	Total pressure loss coeff.
ϑ	Flow turning	R	Gas constant
γ	Ratio of specific heats	c_p	Specific heat at const. P
$\dot{m}$	Mass flow rate	pi	Pressure ratio
η	Adiabatic efficiency	e	Polytropic efficiency
D	Diffusion factor	σ	Solidity
A	Area		

Subscripts

T	"Total"	R	"Relative"
r	"Rotor"	s	"Stator"
1	Rotor inlet	2	Stator inlet
3	Stator exit		

D.2 Baseline Model

For a given choice of the design parameters outlined below, a mean-line compressor design is obtained as follows: For some initial choice of tip-to-hub ratio, the stage inlet flow annulus area is calculated according to the formulae summarized in Sect. D.3. A new tip-to-hub ratio is calculated from the computed area and the iteration is continued to convergence. The procedure is repeated for the next stage, $k+1$, using the previous stage's exit conditions, i.e., $T_{T_1}^{k+1} \leftarrow T_{T_3}^{k}$, $P_{T_1}^{k+1} \leftarrow P_{T_3}^{k}$, $M_1^{k+1} \leftarrow M_3^{k}$, where the superscript indicates stage number. The design parameters are then varied as required to comply with the suggested design guidelines

and the stage iterations repeated. The design parameters, guidelines and outputs are as follows.

- **Design parameters**
  - Number of stages, N
  - Compressor inlet properties: $T^1_{T_1}$, $P^1_{T_1}$, M^1_1, and α^1_1, for $k = 1, \ldots, N$
  - Mass flow rate and wheel speed
  - Compressor inlet tip radius and casing (tip) contraction angle θ_{casing}
  - Rotor and stator total pressure loss coefficients, ϕ^k_r, ϕ^k_s
  - Nominal rotor turning angle ϑ^k_r
  - Rotor and stators axial velocity ratios AVR_r, AVR_s
  - Stage solidity, σ^k
- **Design guidelines** (as suggested in Ref. 81)
  - Stage loading coefficient $\psi = \Delta h_T/(\omega r)^2 \sim 0.3$
  - Flow coefficient $\Phi = u_1/(\omega r) \sim 0.5$
  - Diffusion factors D_r, $D_s < 0.6$
  - Degree of reaction ${}^oR = \Delta h_{\mathrm{rotor}}/\Delta h_{\mathrm{stage}} \sim 0.5$.
  - Axial stage exit flow (no residual swirl)
- **Design outputs**
  - Flow annulus areas: A^k_1, A^k_2, A^k_3, $k = 1, \ldots, N$
  - Stator turning: ϑ^k_s, $k = 1, \ldots, N$
  - Baseline compressor pressure ratio π
  - Adiabatic and polytropic efficiencies, η, e

The six-stage compressor model parameters and stage settings for the baseline design used in Chapter 5 are summarized in Tables D.1 and D.2. In addition, the nominal rotor

Table D.1: Baseline compressor model parameters

$T^1_{T_1}$ (K)	$P^1_{T_1}$ (kpa)	M^1_1	$\dot{m}$ (kg/s)	ω (rad/s)	α^1_1 (deg)	r^1_{tip} (m)	θ_{casing} (deg)
380	300	0.6	70	1400	0	0.30	1.3

and stator loss coefficients taken from the IBR airfoil calculations summarized in Chapter 3 were $\phi_r = \phi_s = 0.03$. The nominal rotor turning, also corresponding to the nominal IBR airfoil was $\vartheta_r = 14.4$ deg. The resulting nominal compressor total pressure ratio, total temperature ratio, and adiabatic and polytropic efficiencies were $\pi = 10.8$, $\tau = 2.03$, $\eta = 0.95$ and $e = 0.96$ respectively. Figure D-1 shows the a schematic representation of the compressor stages and the mean-line path. Table D.3 shows the pressure and temperature ratios, diffusion factors, stage loading, flow coefficient, and degree of reaction for each stage of the nominal mean-line model. Similarly D.4 shows exit total temperatures, pressures and Mach number, as well as stator inlet area, stator inlet absolute flow angle and nominal stator turning.

Table D.2: Baseline compressor model stage settings

Stage	1	2	3	4	5	6
α_3	0	0	0	0	0	0
AVR_r	1	1	1	1	1	1
AVR_s	1	1	1	1	1	1
σ	1	1	1.2	1.4	1.6	1.7
AR	1.6	1.6	1.6	1.7	1.8	1.8
θ_{stagger}	30	30	35	35	40	45

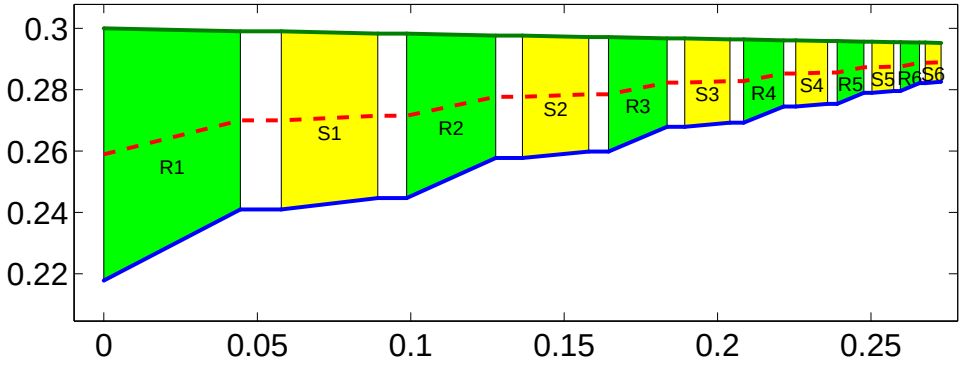

Figure D-1: Compressor model stages

D.3 Stage formulae

$$M_1 = f^{-1}\left(\frac{\dot{m}\sqrt{T_{T_1}}}{P_{T_1}A_1\cos\alpha_1}, \gamma, R\right), \quad f(M) = \sqrt{\frac{\gamma}{R}}\frac{M}{\left(1+\frac{\gamma-1}{2}M^2\right)^{\frac{\gamma+1}{2(\gamma-1)}}}.$$

$$T_1 = \frac{T_{T_1}}{1+\frac{\gamma-1}{2}M_1^2}, \quad P_1 = \frac{P_{T_1}}{(1+\frac{\gamma-1}{2}M_1^2)^{\gamma/(\gamma-1)}}$$
$$a_1 = \sqrt{\gamma R T_1}, \quad V_1 = M_1 a_1, \quad u_1 = V_1\cos\alpha_1, \quad v_1 = V_1\sin\alpha_1$$
$$v_{1R} = \omega r - v_1, \quad \beta_1 = \arctan(v_{1R}/u_1),$$
$$V_{1R} = \sqrt{u_1^2 + v_{1R}^2}, \quad M_{1R} = V_{1R}/a_1$$

$$T_{T_{1R}} = T_1\left(1+\frac{\gamma-1}{2}M_{1R}^2\right), \quad P_{T_{1R}} = P_1\left(\frac{T_{T_{1R}}}{T_1}\right)^{\gamma/(\gamma-1)}$$
$$P_{T_{2R}} = P_{T_{1R}}\left[1-\phi_r\frac{\gamma M_{1R}^2}{(1+\frac{\gamma-1}{2}M_{1R}^2)^{\gamma/(\gamma-1)}}\right]$$

Table D.3: Baseline six-stage compressor model (1)

Stage	η	π	D_r	D_s	ψ	Φ	$^\circ R$
1	0.964	1.655	0.440	0.478	0.429	0.599	0.785
2	0.962	1.573	0.454	0.483	0.421	0.582	0.789
3	0.960	1.504	0.432	0.438	0.418	0.573	0.791
4	0.959	1.447	0.415	0.405	0.416	0.567	0.792
5	0.958	1.400	0.402	0.381	0.415	0.563	0.792
6	0.957	1.360	0.397	0.372	0.415	0.560	0.793

Table D.4: Baseline six-stage compressor model (2)

Stage	T_{T_3} (K)	P_{T_3} (kpa)	M_3	A_2 (m^2)	α_2 (deg)	ϑ_s (deg)
1	441.0	496.5	0.554	0.12112	35.6	-35.6
2	504.4	781.1	0.516	0.08588	35.8	-35.8
3	569.4	1175.0	0.484	0.06322	36.1	-36.1
4	635.5	1700.2	0.457	0.04801	36.2	-36.2
5	702.4	2379.8	0.434	0.03743	36.4	-36.4
6	769.9	3237.7	0.414	0.02982	36.5	-36.5

$$u_2 = \mathrm{AVR}_r u_1, \quad T_{T_{2R}} = T_{T_{1R}}, \quad \beta_2 = \beta_1 - \vartheta_r$$
$$\Delta T_T = \frac{\omega}{c_p}(r_1 u_1 \tan\beta_1 - r_2 u_2 \tan\beta_2), \quad T_{T_2} = T_{T_1} + \Delta T_T$$

$$v_{2R} = u_2 \tan\beta_2, \quad V_{2R} = \sqrt{u_2^2 + v_{2R}^2},$$
$$v_2 = \omega r_2 - v_{2R}, \quad \alpha_2 = \arctan(v_2/u_2), \quad V_2 = \sqrt{u_2^2 + v_2^2}$$

$$T_2 = T_{T_2} - \frac{V_2^2}{2c_p}, \quad P_2 = P_{T_{2R}} \left(\frac{T_2}{T_{T_{2R}}}\right)^{\gamma/(\gamma-1)}$$
$$a_2 = \sqrt{\gamma R T_2}, \quad M_2 = V_2/a_2, \quad M_{2R} = V_{2R}/a_2$$

$$A_2 = \frac{\dot{m}}{P_{T_2}\cos\alpha_2 M_2}\sqrt{\frac{T_{T_2}R}{\gamma}}\left(1 + \frac{\gamma-1}{2}M_2^2\right)^{\frac{\gamma+1}{2(\gamma-1)}}$$

$$P_{T_2} = P_2\left(\frac{T_{T_2}}{T_2}\right)^{\gamma/(\gamma-1)}, \quad T_{T_3} = T_{T_2}, \quad T_3 = \frac{T_{T_3}}{1 + \frac{\gamma-1}{2}M_3^2}$$
$$\left(\frac{P_{T_3}}{P_{T_2}}\right)_{\phi_s} = 1 - \phi_s \frac{\gamma M_2^2/2}{(1 + \frac{\gamma-1}{2}M_2^2)^{\gamma/(\gamma-1)}}$$

$$u_3 = \mathrm{AVR}_s u_1$$

$$P_{T_3} = P_{T_2}\left(\frac{P_{T_3}}{P_{T_2}}\right)_{\phi_s}, \quad P_3 = P_{T_3}\left(\frac{T_3}{T_{T_3}}\right)^{\gamma/(\gamma-1)}$$

$$a_3 = \sqrt{\gamma R T_3}, \quad V_3 = M_3 a_3,$$

$$u_3 = V_3\cos\alpha_3, \quad v_3 = V_3\sin\alpha_3$$

$$A_3 = \frac{\dot{m}}{P_{T_3}\cos\alpha_3 M_3}\sqrt{\frac{T_{T_3}R}{\gamma}}\left(1+\frac{\gamma-1}{2}M_3^2\right)^{\frac{\gamma+1}{2(\gamma-1)}}$$

$$\pi_c = \frac{P_{T_3}}{P_{T_1}}, \quad \eta_{\text{stage}} = \frac{(P_{T_3}/P_{T_1})^{(\gamma-1)/\gamma}-1}{T_{T_3}/T_{T_1}-1}, \quad \eta_{\text{poly}} = \frac{(\gamma-1)}{\gamma}\frac{\log(P_{T_3}/P_{T_1})}{\log(T_{T_3}/T_{T_1})}$$

D.4 Rotor System Jacobian

The following are the entries of the Jacobian corresponding to the nonlinear system 5.1–5.3.

$$\frac{\partial F}{\partial \Delta T_T} = 1 - \sin\alpha_2\frac{\omega r_2}{c_p}\frac{\partial V_2}{\partial \Delta T_T}, \qquad \frac{\partial G}{\partial \Delta T_T} = \frac{\dot{m}\sqrt{T_{T_2}}}{A_2 P_{T_2}\cos\alpha_2}\left(\frac{1}{2T_{T_2}} - \frac{1}{P_{T_2}}\frac{\partial P_{T_2}}{\partial \Delta T_T}\right),$$

$$\frac{\partial F}{\partial M_2} = -\sin\alpha_2\frac{\omega r_2}{c_p}\frac{\partial V_2}{\partial \Delta M_2}, \qquad \frac{\partial G}{\partial M_2} = (M_2^2-1)\sqrt{\frac{\gamma}{R}}\left(1+\frac{\gamma-1}{2}M_2^2\right)^{\frac{1-3\gamma}{2(\gamma-1)}}$$

$$\frac{\partial F}{\partial \alpha_2} = -\cos\alpha_2\frac{\omega r_2}{c_p}V_2, \qquad \frac{\partial G}{\partial \alpha_2} = \frac{\dot{m}\sqrt{T_{T_2}}}{P_{T_2}A_2\cos\alpha_2}\tan\alpha_2$$

$$\frac{\partial H}{\partial \Delta T_T} = (\sin\alpha_2 + \cos\alpha_2\tan\beta_2)\frac{\partial V_2}{\partial \Delta T_T}$$

$$\frac{\partial H}{\partial M_2} = (\sin\alpha_2 + \cos\alpha_2\tan\beta_2)\frac{\partial V_2}{\partial M_2}$$

$$\frac{\partial H}{\partial \alpha_2} = (\cos\alpha_2 - \sin\alpha_2\tan\beta_2)V_2$$

where

$$\frac{\partial V_2}{\partial \Delta T_T} = \frac{1}{2}\frac{V_2}{T_{T_2}},$$

$$\frac{\partial V_2}{\partial \Delta_{M_2}} = \frac{V_2}{M_2}\left[1 - \frac{(\gamma-1)M_2^2}{2+(\gamma-1)M_2^2}\right],$$

$$\frac{\partial P_{T_2}}{\partial \Delta T_T} = \left(\frac{P_{T_2}R}{T_{T_{1R}}^{\gamma}}\right)\left(\frac{T_{T_2}}{T_{T_{1R}}}\right)^{\frac{1}{\gamma-1}}$$

Bibliography

[1] J. D. Adamson. The probabilistic design system development experience. AIAA-94-1444-CP, AIAA, 1994.

[2] Advisory Group for Aerospace Research and Development. *Erosion, Corrosion and Foreign Object Damage Effects in Gas Turbines*, 7 Rue Ancelle, 92200 Neuilly-Sur-Seine, France, April 1994. AGARD-CP-558.

[3] N. M. Alexandrov, R. M. Lewis, C. R. Gumbert, L. L. Green, and P. A. Newman. Optimization with variable-fidelity models applied to wing design. AIAA-2000-0841, AIAA, 2000.

[4] N. M. Alexandrov, E. J. Nielsen, R. M. Lewis, and W. K. Anderson. First-order model management with variable-fidelity physics applied to multi-element airfoil optimization. AIAA-2000-4886, AIAA, 2000.

[5] V. R. Algazi and D. J. Sakrison. On the optimality of the Karhunen-Loéve expansion. *IEEE Trans. Inform. Theory*, 15:319–21, 1969.

[6] C. A. Andrews, J. M. Davies, and G. R. Schwartz. Adaptive data compression. *Proc. IEEE*, 55:267–77, 1967.

[7] A. H-S. Ang and W. H. Tang. *Probability Concepts in Engineering Planning and Design*, volume I–Basic Principles. John Wiley & Sons, Inc., New York, NY, 1975.

[8] D. Armbruster, R. Heiland, and E. J. Kostelich. KLTOOL: A tool to analyze spatiotemporal complexity. *Chaos*, 4(2):421–424, 1994.

[9] M. W. Bailey. First order manufacturing constraints and requirements. In *Integrated Multidisciplinary Design of High Performance Multistage Compressor Systems*, pages 3.1–3.27, 1998. AGARD RTO Lecture Series No. 211.

[10] V. S. Beknev, I. N. Egorov, and V. S. Talyzina. Multicriterion design optimization of the multistage axial flow compressor. In *1991 ASME Cogen-Turbo*, pages 453–460. ASME IGTI, 1991.

[11] D. P. Bertsekas. *Nonlinear Programming*. Athena Scientific, Belmont, MA, second edition, 1999.

[12] H. P. Breuer and F. Petruccione. A stochastic approach to computational fluid dynamics. *Continuum Mechanics and Thermodynamics*, 4:247–67, 1997.

[13] J. Burkardt and M. Gunzburger. Sensitivity discrepancy for geometric parameters. In O. Baysal, editor, *CFD For Design and Optimization*, pages 9–15. ASME, 1995.

[14] B. Busnello. A probabilistic approach to the two-dimensional Navier-Stokes equations. *The Annals of Probability*, 27(4):1750–80, 1999.

[15] D. H. Chambers, R. J. Adrian, P. Moin, D. S. Stewart, and H. J. Sung. Karhunen-Loéve expansion of burger's model of turbulence. *Phys. Fluids*, 31(9):2573–2582, September 1988.

[16] C. C. Chamis. Probabilistic structural analysis methods for space propulsion system components. *Probabilistic Engineering Mechanics*, 2(2):100–10, 1987.

[17] R. V. Chima. Calculation of tip clearance effects in a transonic compressor rotor. *ASME Journal of Turbomachinery*, 120:131–140, January 1998.

[18] A. R. Conn, N. I. M. Gould, and P. L. Toint. *Trust-Region Methods*. MPS-SIAM series on optimization. Society for Indistrial and Applied Mathematics, Philadelphia, PA, 2000.

[19] N. A. Cumpsty. *Compressor Aerodynamics*. Longman, London, 1989.

[20] A. Dadone, M. Valorani, and B. Grossman. Smoothed sensitivity equation method for fluid dynamic design problems. *AIAA Journal*, 38(3):418–426, March 2000.

[21] C. de Boor. *A Practical Guide To Splines*, volume v. 27 of *Applied Mathematical Series*. Springer Verlag, New York, 1978.

[22] C. de Boor. *Matlab Spline Toolbox User's Guide Version 3*. The MathWorks, Inc., 3 Apple Hill Drive, Natick, MA, 2002.

[23] J. D. Denton. The 1993 IGTI scholar lecture: Loss Mechanisms in Turbomachines. *ASME J. of Turbomachinery*, 115(4):621–656, October 1993.

[24] M. Drela. *Two-Dimensional Transonic Aerodynamic Design and Analysis Using the Euler Equations*. Ph.D. thesis, Massachusetts Institute of Technology, 1985.

[25] M. Drela. A users's guide to MTFLOW 1.2. MIT Fluid Dynamics Research Laboratory, November 1997.

[26] M. Drela. Pros and cons of airfoil optimization. In D. A. Caughey and M. M. Hafez, editors, *Frontiers of Computational Fluid Dynamics 1998*, chapter 19, pages 363–380. World Scientific Publishing, 1999.

[27] M. Drela and H. Youngren. *A User's Guide to MISES 2.53*. MIT Fluid Dynamics Research Laboratory, 70 Vassar ST, Cambridge MA 02139, December 1998.

[28] M. Drela and H. Youngren. *XFOIL 6.9 User Guide*. Dept. of Aeronautics and Astronautics, MIT, 77 Massachusetts Ave, Cambridge MA 02139, Jan 2001.

[29] X. Du and W. Chen. Methodology for managing the effect of uncertainty in simulation-based design. *AIAA Journal*, 38(8):1471–8, August 2000.

[30] J. Dunham, editor. CFD validation for propulsion system components. AGARD Advisory Report, 1997.

[31] I. N. Egorov. Optimization of a multistage axial compressor stochastic approach. ASME paper 92-GT-163, ASME, 1992.

[32] I. N. Egorov and G. V. Kretinin. Multicriterion stochastic optimization of axial compressor. In *1992 ASME Cogen-Turbo, IGTI-Vol.7*, pages 563–570. ASME IGTI, 1992.

[33] I. N. Egorov and G. V. Kretinin. Optimization of gas turbine engine elements by probability criteria. ASME paper 93-GT-191, ASME, 1993.

[34] J. Elliott and J. Peraire. Constrained, multipoint shape optimisation for complex 3D configurations. *The Aeronautical Journal*, 102:365–76, 1998.

[35] Engine Yearbook 1996–1997. A new lease of life for gas turbine compressor airfoils. Aircraft Technology Engineering & Maintenance, Aviation Industry Press., 1997.

[36] S. Eyi and K. D. Lee. Effects of sensitivity analysis on aerodynamic design optimization. In O. Baysal, editor, *CFD For Design and Optimization*, pages 1–8. ASME, 1995.

[37] George S. Fishman. *Monte Carlo: Concepts, Algorithms and Applications*. Springer Verlag, New York, 1996.

[38] R. Fletcher. *Practical Methods of Optimization*. John Wiley and Sons, Ltd., New York, 1987.

[39] E. P. Fox. Methods of integrating probabilistic design within an organization's design system using Box-Behnken matrices. AIAA-93-1380-CP, AIAA, 1993.

[40] E. P. Fox. The Pratt & Whitney probabilistic design system. AIAA-94-1442-CP, AIAA, 1994.

[41] U. Frisch. *Turbulence: The Legacy of A. N. Kolmogorov*. Cambridge University Press, 1995.

[42] J. L. Lumley G. Berkooz, P. Holmes. The proper orthogonal decomposition in the analysis of turbulent flows. *Annu. Rev. Fluid Mech.*, 25:539–75, 1993.

[43] P. Garbaczewski, G. Kondrat, and R. Olkiewicz. Burgers' flows as Markovian diffusion processes. *Physical Review E*, 55(2):1401–12, February 1997.

[44] V. E. Garzon and D. L. Darmofal. Using computational fluid dynamics in probabilistic engineering design. 2001-2526, AIAA, 2001.

[45] K. H. Gau. Improve designs using probabilistic sensitivity information. 1999 Quality and Productivity Research Conference, May 1999.

[46] M. B. Giles and N. A. Pierce. An introduction to the adjoint approach to design. Report 00/04, Oxford University Computing Laboratory, Numerical Analysis Group, Wolfson Bldg., Pars Rd., Oxford, England, OX 1 3QD, March 2000.

[47] M. B. Giles and N. A. Pierce. Analytic adjoint solutions for the quasi-one-dimensional Euler equations. *J. Fluid Mech.*, 426:327–345, 2001.

[48] A. A. Giunta. Use of data sampling, surrogate models, and numerical optimization in engineering design. AIAA-2002-0538, AIAA, 2002.

[49] R. C. Gonzalez. *Digital Image Processing*. Addison Wesley, 1992.

[50] M. Grigoriu. A monte carlo solution of transport equations. *Probabilistic Engineering Mechanics*, 13(3):169–174, 1998.

[51] C. R. Gumbert, P. A. Newman, and G. J.-W. Hou. Effect of random geometric uncertainty on the computational design of a 3-D flexible wing. AIAA 2002-2806, 2002.

[52] J. Hačker. *Statistical Analysis of Manufacturing Deviations and Classification Methods for Probabilistic Aerothermal Design of Turbine Blades*. Diplomarbeit, Department of Aeronautics and Astronautics, University of Stuttgart, Stuttgart, Germany, August 2000.

[53] A. Haji-Sheikh and E. M. Sparrow. The floating random walk and its applications to monte carlo solutions of heat equations. *J. SIAM Appl. Math.*, 14(2):370–389, March 1966.

[54] K. C. Hall, J. P. Thomas, and E. H. Dowell. Proper orthogonal decomposition technique for transonic unsteady aerodynamic flows. *AIAA Journal*, 38(10):1853–62, October 2000.

[55] A. Hamed and W. Tabakoff. Experimental and numerical simulations of the effects of ingested particles in gas turbine engines. In *Erosion, Corrosion and Foreign Object Damage Effecs in Gas Turbines*. Advisory Group for Aerospace Research and Development, 1994. AGARD-CP-558.

[56] J. M. Hammersley and D. C. Handscomb. *Monte Carlo Methods*. Methuen & Co., London, England, 1965.

[57] R. W. Heiland. KLTOOL: A mathematical tool for analyzing spatiotemporal data. Master's thesis, Dept. of Mathematics, Arizona State University, December 1992.

[58] D. E. Hobbs and H. D. Weingold. Development of controlled diffusion airfoils for multistage compressor application. *ASME Journal of Engineering for Gas Turbines and Power*, 106:271–8, April 1984.

[59] H. Holden and Y. Hu. Finite difference approximation of the pressure equation for fluid flows in a stochastic medium—a probabilistic approach. *Communications in Partial Differential Equations*, 21(9 & 10):1367–88, 1996.

[60] P. Holmes, J. L. Lumley, and G. Berkooz. *Turbulence, Coherent Structures, Dynamical Systems and Symmetry*. Cambridge University Press, England, 1996.

[61] L. Huyse. Aerodynamic shape optimization of two-dimensional airfoils under uncertain conditions. Technical Report NASA/CR-2001-210648, Langley Research Center, Hampton, VA, January 2001.

[62] L. Huyse. Free-form airfoil shape optimization under uncertainty using maximum expected value and second-order second-moment strategies. Report 2001-18, ICASE, 2001.

[63] L. Huyse. Solving problems of optimization under uncertainty as statistical decision problems. AIAA 2001-1519, 2001.

[64] L. Huyse and R. W. Walters. Random field solutions including boundary condition uncertainty for the steady-state generalized Burgers equation. Report 2001-35, ICASE, 2001.

[65] R. L. Iman. Uncertainty and sensitivity analysis for computer modeling applications. *Reliability Technology*, 28:153–168, 1992.

[66] A. Jameson. Computational fluid dynamics for aerodynamic design: Its current and future impact. Paper AIAA-2001-0538, AIAA, 2001.

[67] I. T. Jolliffe. *Principal Component Analysis*. Springer Verlag, New York, 1986.

[68] R. Jugulum and A. Dichter. Taguchi methods in american universities and corporations. *Quality Engineering*, 13(4):607–621, 2001.

[69] G. E. Karniadakis. Quantifying uncertainty in CFD. *Journal of Fluids Engineering*, 124:2–3, March 2002.

[70] J. Kirchner. Aerodynamic design of an aspirated counter-rotating compressor. Master's thesis, Massachusetts Institute of Technology, Cambridge, MA, June 2002.

[71] C. C. Koch and J. H. Smith, Jr. Loss sources and magnitudes in axial-flow compressors. *ASME Journal of Engineering and Power*, pages 411–424, July 1976.

[72] P. N. Koch. Probabilistic design: Optimizing for six sigma quality. AIAA 2002-1471.

[73] P. N. Koch, B. Wujek, and O. Golovidov. A multi-stage, parallel implementation of probabilistic design optimization in an MDO framework. AIAA 2000-4805, 2000.

[74] D. D. Kosambi. Statistics in function space. *J. Indian Math. Soc.*, 7:76–88, 1943.

[75] M. Loève. *Probability Theory*. Springer Verlag, New York, 1977.

[76] E. N. Lorenz. Empirical orthogonal functions and statistical weather prediction. Sci. report 1, MIT Dept. of Meteorology, Cambridge, MA, 1956.

[77] J. L. Lumley. *Stochastic Tools In Turbulence*. Academic Press, New York, 1970.

[78] C. Lykins, D. Thomson, and C. Pomfret. The Air Force's application of probabilistics to gas turbine engines. AIAA-94-1440-CP, AIAA, 1994.

[79] J. I. Madsen, W. Shyy, and R. T. Haftka. Response surface techniques for diffuser shape optimization. *AIAA Journal*, 38(9):1512–8, September 2000.

[80] B. Mantel, J. Periaux, M. Sefrioui, and B. Stoufflet. Evolutionary computational methods for complex design in aerodynamics. AIAA-98-0222, AIAA, 1998.

[81] Jack D. Mattingly. *Elements of Gas Turbine Propulsion*. McGraw Hill, New York, NY, 1996.

[82] D. N. Mavris and O. Bandte. A probabilistic approach to multivariate constrained robust design simulation. Paper SAE-975508, Society of Automotive Engineers, 1997.

[83] D. N. Mavris, N. I. Macsotai, and B. Roth. A probabilistic design methodology for commercial aircraft engine cycle selection. Paper SAE-985510, Society of Automotive Engineers, 1998.

[84] M. D. McKay, W. J. Conover, and R. J. Beckman. A comparison of three methods for selecting values of input variables in the analysis of output from a computer code. *Technometrics*, 21(2):239–245, 1979.

[85] A. Merchant. *Design and Analysis of Axial Aspirated Compressor Stages*. Ph.D. thesis, Massachusetts Institute of Technology, 1999.

[86] M. Metwally, W. Tabakoff, and A. Hamed. Blade erosion in automotive gas turbine engines. *ASME J. of Engineering for Gas Turbines and Power*, 117:213–219, January 1995.

[87] H. R. Millwater and Y.-T. Wu. Global/local methods for probabilistic structural analysis. Technical Report AIAA-93-1378-CP, AIAA, 1993.

[88] C. Z. Mooney. *Monte Carlo Simulation*. Sage Publications Inc, Thousand Oaks, CA, 1997.

[89] V. N. Nair. Taguchi's parameter design: A panel discussion. *Technometrics*, 34(2):127–161, May 1992.

[90] E. J. Nielsen and W. K. Anderson. Recent improvements in aerodynamic design optimization on unstructured meshes. Paper AIAA-2001-0596, AIAA, 2001.

[91] S. Obayashi and T. Tsukahara. Comparison of optimization algorithms for aerodynamic shape design. *AIAA Journal*, 35(8):1413–5, August 1997.

[92] A. M. Obukhov. The statistical description of continuous fields. *Trans. Geophys. Inst. Acad. Sci. USSR*, 24:3–42, 1954.

[93] E. Oja. Neural networks, principal components and subspaces. *Int. J. Neural Systems*, 1(1):61–68, 1989.

[94] J. Otto, M. Paraschivoiu, S. Yesilyurt, and A. T. Patera. Bayesian-validated computer-simulation surrogates for optimization and design: Error estimates and applications. *Mathematics and Computers in Simulation*, 44:347–67, 1997.

[95] A. Papoulis. *Probability, Random Variables, And Stochastic Processes*. McGraw Hill, Inc., third edition, 1991.

[96] J. M. Parks. On stochastic optimization: Taguchi methods demystified; its limitations and fallacy clarified. *Probabilistic Engineering Mechanics*, 16:87–101, 2001.

[97] J. Periaux, G. Degrez, and H. Deconick, editors. *Genetic Algorithms in Aeronautics and Turbomachinery*, Belgium, 2000. Von Karman Institue for Fluid Dynamics.

[98] M. S. Phadke. *Quality Engineering Using Robust Design*. Prentice-Hall, Englewood Cliffs, NJ, 1989.

[99] V. S. Pougachev. General theory of correlations of random functions. *Izv. Akad. Nauk. SSSR*, 17:401–2, 1953.

[100] R. W. Preisendorfer. *Principal Component Analysis in Meteorology and Oceanography*. Elsevier, Amsterdam, 1988.

[101] M. M. Putko, P. A. Newman, A. C. Taylor III, and L. L. Green. Approach for uncertainty propagation and robust design in CFD using sensitivity derivatives. AIAA 2001-2528, 2001.

[102] L. Reid and D. C. Urasek. Experimental evaluation of the effects of a blunt leading edge on the performance of a transonic rotor. *ASME J. of Engineering and Power*, pages 199–204, July 1973.

[103] W. B. Roberts. Advanced turbofan blade refurbishment technique. *ASME Journal of Turbomachinery*, 117:666–7, October 1995.

[104] W. B. Roberts, A. Armin, G. Kassaseya, K. L. Suder, S. A. Thorp, and A. J. Strazisar. The effect of variable chord length on transonic axial rotor performance. ASME paper 2001-GT-0498, 2001.

[105] William B. Roberts. Axial compressor performance restoration by blade profile control. AIAA-84-GT-232, ASME, 1984.

[106] M.C. Romanowski. Reduced order unsteady aerodynamic and aeroelastic models using Karhunen-Loéve eigenmodes. AIAA Paper 96-194, 1996.

[107] A. Rosenfeld and A. C. Kak. *Digital Picture Processing*. Academic Press, New York, 1982.

[108] S. Ross. *A First Course in Probability*. Prentice Hall, Upper Saddle River, NJ, fifth edition, 1997.

[109] R. S. Ryan and J. S. Townsend. Application of probabilistic analysis/design methods in space programs: The approaches, the status, and the needs. AIAA-93-1381, AIAA, 1993.

[110] M. N. O. Sadiku. Monte carlo solution of axisymmetric potential problems. *IEEE Transactions of Industry Applications*, 29(6):1042–6, 1993.

[111] F. M. Safie. Use of probabilistic design methods for NASA applications. *Reliability Technology*, 28:17–24, 1992.

[112] K. Y. Sanliturk, M. Imregun, and D. J. Ewins. A probabilistic analysis of single-degree-of-freedom blade vibration. Paper 93-GT-264, ASME, 1993.

[113] M. S. Sasena, P. Y. Papalambros, and P. Goovaerts. Metamodeling sampling criteria in a global optimization framework. AIAA-2000-4921, AIAA, 2000.

[114] B. J. Schuler, J. L. Kerrebrock, A. A. Merchant, and M. Drela. Design, analysis, fabrication and test of an aspirated fan stage. Paper 2000-GT618, ASME, 2000.

[115] J. N. Siddall. *Probabilistic Engineering Design: Principles And Applications*, volume 23 of *Mechanical Engineering*. M. Dekker, Inc., New York, NY, 1983.

[116] T. W. Simpson and F. Mistree. Kriging models for global approximation in simulation-based multidisciplinary design optimization. *AIAA Journal*, 39(12):2233–41, December 2001.

[117] L. Sirovich. Turbulence and the dynamics of coherent structures, parts I–III. *Quart. J. Appl. Math.*, 45(3):561–90, 1987.

[118] L. Socha. A survey of quantitative and qualitative methods of sensitivity analysis for stochastic dynamic systems. *Probabilistic Engineering Mechanics*, 6(3–4):148–163, 1991.

[119] H. Starken and H. A. Schreiber. Test case E/CA-4: Low supersonic compressor cascade MCA. In L. Fottner, editor, *Test Cases for Computation of Internal Flows in Aero Engine Components*, pages 81–94. Advisory Group for Aerospace Research and Development, NATO, 1990.

[120] A. Strazisar. Aerodynamic performance data for NASA Rotor 37 test case. Personal communication, Nov 2001.

[121] K. L. Suder. Experimental and computational investigation of the tip clearance flow in a transonic axial compressor rotor. *ASME Journal of Turbomachinery*, 118:218–229, April 1996.

[122] K. L. Suder. Blockage development in a transonic, axial compressor rotor. *ASME Journal of Turbomachinery*, 120:465–476, July 1998.

[123] K. L. Suder, R. V. Chima, A. J. Strazisar, and W. B. Roberts. The effect of adding roughness and thickness to a transonic axial compressor rotor. *ASME J. of Turbomachinery*, 117:491–505, October 1995.

[124] N. P. Suh. *The Principles of Design*. Oxford University Press, New York, NY, 1990.

[125] W. Tabakoff and A. Hamed. Blade deterioration in a gas turbine engine. *Int. J. of Rotating Machinery*, 4:233–241, November 1998.

[126] A. C. Taylor III, L. L. Green, P. A. Newman, and M. M. Putko. Some advanced concepts in discrete aerodynamic sensitivity analysis. AIAA 2001-2529, 2001.

[127] The MathWorks, Inc., Natick, MA. *Optimization Toolbox User's Guide, V2.0*, 2002.

[128] James R. Thompson. *Simulation: A Modeler's Approach*. John Wiley & Sons, Inc., New York NY, 2000.

[129] D. E. Thomson and T. G. Fecke. Air force perspective on probabilistic design. *Reliability Technology*, 28:25–32, 1994.

[130] L. N. Trefethen and D. Bau. *Numerical Linear Algebra*. Society for Industrial and Applied Mathematics, Philadelphia, PA, 1997.

[131] E. Turgeon, D. Pelletier, and S. Etienne. Sensitivity and uncertainty analysis for turbulent flows. Technical Report AIAA 2002-0985, AIAA, 2002.

[132] R. W. Walters and L. Huyse. Uncertainty analysis for fluid mechanics with applications. Report 2002-1, ICASE, 2002.

[133] L. Wang. Fast probability integration (FPI) and its applications to dfss. 1999 Quality And Productivity Research Conference, May 1999.

[134] X. Wang and M. Damodaran. Aerodynamic shape optimization using computational fluid dynamics and parallel simulated annealing algorithms. *AIAA Journal*, 39(8):1500–8, August 2001.

[135] X. Wang and M. Damodaran. Design optimization of 3D nozzle shapes using CFD and parallel simulated annealing. AIAA-2001-0264, AIAA, 2001.

[136] K. Willcox, J. Peraire, and J. White. An Arnoldi approach for generation of reduced-order models for turbomachinery. *Computers and Fluids*, 31(3):369–389, March 2002.

[137] K. E. Willcox. *Reduced-Order Aerodynamic Models for Aeroelastic Control of Turbomachines*. PhD thesis, Dept. of Aeronautics and Astronautics, MIT, Cambridge, MA, February 2000.

[138] C. Y. Wu. Arbitrary surface flank milling of fan, compressor and impeller blades. *ASME Journal of Engineering for Gas Turbines and Power*, 117:534–539, July 1995.

[139] J. N. Yang, S. D. Manning, J. L. Rudd, and M. E. Artley. Probabilistic durability analysis methods for metallic airframes. *Probabilistic Engineering Mechanics*, 2(1):9–15, 1987.

[140] S. Yesilyurt and A. Patera. Surrogates for numerical simulations: Optimization of eddy-promoter heat exchangers. *Computer Methods in Applied Mechanics and Engineering*, 121:231–57, 1995.

[141] H. Youngren. Analysis and design of transonic cascades with splitter vanes. Masters thesis, Massachusetts Institute of Technology, March 1991.